

# MICROWAVE EXPERIMENTS ON GRAPHS SIMULATING SPIN-1/2 SYSTEM

**Dissertation**

zur

Erlangung des Doktorgrades

der Naturwissenschaften

(Dr. rer. nat.)

dem

Fachbereich Physik

der Philipps-Universität Marburg

vorgelegt von

**Aimaiti Rehemanjiang**

aus

Kashgar, Volksrepublik China

August 24, 2018

Vom Fachbereich Physik der Philipps-Universität Marburg als Dissertation  
angenommen am 06.08.2018

Erstgutachter: Prof. Dr. Ulrich Kuhl  
Zweitgutachter: Prof. Dr. Bruno Eckhardt  
Tag der mündlichen Prüfung : 20.08.2018

*Ich widme diese Arbeit meiner Frau Gulistan und meinem Sohn Zulkar.  
Bu emgikimni ayalim Gulistan'gha we oghlum Zulkar'ge béghishlaymen.*





# Abstract

In this work I study the statistical properties of the Gaussian symplectic ensemble (GSE) by means of microwave experiments on quantum graphs mimicking spin-1/2 systems. Additionally, the transport property of three terminal microwave graphs with orthogonal, unitary and symplectic symmetry is investigated.

In the first part of this thesis, following the spirit of the idea proposed by Joyner *et al.* we construct microwave quantum graphs to realize a antiunitary symmetry  $\mathcal{T}$  that squares to minus one,  $\mathcal{T}^2 = -1$ . This symmetry induces degenerate eigenvalues, which are called Kramers doublets. If the classical dynamics of the system is chaotic, statistical features of the spectrum can be well described by the corresponding statistics of random matrix Gaussian symplectic ensemble. Indeed, Kramers doublets are observed in reflection spectrum as expected from the scattering properties of a symplectic graph. The level spacing distribution of these doublets is compared with the corresponding random matrix predictions. Since the level spacing distribution accounts for the short range eigenvalue correlation, to study the spectral long range correlation the spectral two point correlation function and its Fourier transform, the spectral form factor are analyzed. In order to further examine the fluctuation of the eigenvalues smoothed quantities such as number variance and spectral rigidity are discussed. The graphs used in the experiment consist of two subgraphs coupled via one pair of connecting bonds. Theoretical study shows that the level spacing distribution for graphs with one pair of connecting bonds deviates by few percents from the random matrix prediction. This difference is too small to be resolved in the experiment. The one pair of bonds approximation is introduced to better understand the symplectic graph we used in the experiment. This model is extended to address more general cases of the symplectic graph. Finally, the parameter dependent dynamical transition of the statistical features of the spectrum from GSE via Gaussian unitary ensemble (GUE) to Gaussian orthogonal ensemble (GOE) is studied.

In the second part of this thesis, the collaborative work with Dr. A. M. Martínez-Argüello from Mexico is briefly presented. A three terminal setup is proposed to study the universal transport properties of systems with orthogonal, unitary and symplectic symmetry. The probability distribution for a transport related quantity is predicted analytically and microwave graphs are constructed to test this prediction. The absorption within the system is modeled by effective Hamiltonian approach. The parameters of the absorption and coupling are extracted from the experimental autocorrelation function. This allowed a comparison between experiment and theory without any free parameters. Finally, a quantitative good agreement between experiment and theory was found for all three symmetry classes.



# Zusammenfassung

In dieser Arbeit untersuche ich das Gaußsche symplektische Ensemble (GSE) in einem Mikrowellen-Netzwerk, im folgenden Graph genannt, mit einer Symmetrie, die einen Spin-1/2 simuliert. Im weiteren werden die Transporteigenschaften von Mikrowellengraphen mit drei offenen Enden für orthogonale, unitäre und symplektische Symmetrie untersucht.

Im ersten Teil der Arbeit konstruieren wir, einer Idee von Joyner et al. folgend, Mikrowellengraphen mit einer antinuitären Symmetrie  $\mathcal{T}$ , also mit der Eigenschaft  $\mathcal{T}^2 = -1$ . In einem System mit einer solchen Symmetrie erwartet man ein Eigenwertspektrum bestehend aus Kramersdupletts. Wenn die klassische Dynamik des Systems chaotisch ist, sollten die statistischen Eigenschaften des Spektrums durch die des Gaußschen symplektischen Zufallsmatrix-Ensembles beschrieben werden. In der Tat wurden Kramers-Dupletts im Reflexionsspektrum gefunden, wie man sie von den Streueigenschaften eines symplektischen Graphen erwartet. Die Abstandsverteilung der Dupletts wird mit der entsprechenden Zufallsmatrix-Vorhersage verglichen. Da die Abstandsverteilungen durch die kurz-reichweitigen Eigenwert-Korrelationen bestimmt werden, wurde für die langreichweitigen Korrelationen auch die spektrale Zweipunktkorrelation und ihre Fouriertransformation, der spektrale Formfaktor analysiert. Weiter wurden auch geglättete Größen wie die Varianz der Eigenwerte in einem vorgegebenen Intervall, Varianz der Level-Anzahl (number variance) und die spektrale Rigidität (spectral rigidity) untersucht. Die in den Experimenten verwendeten Graphen bestehen aus zwei Untergraphen, die durch zwei Verbindungen miteinander gekoppelt sind. Theoretische Untersuchungen zeigten, dass die Abstandsverteilungen bei Kopplung mit nur zwei Bindungen um einige Prozent von der erwarteten Zufallsmatrixverteilung abweichen, zu klein, um sie im Experiment aufzulösen. Weiter wurde ein parameterabhängiger Übergang von GSE über das Gaußsche unitäre Ensemble (GUE) zum Gaußsche orthogonalen Ensemble (GOE) untersucht.

Im zweiten Teil der Arbeit wurden in Zusammenarbeit mit Dr. A. M. Martínez-Argüello aus Mexiko, Mikrowellengraphen mit drei offenen Enden mit wahlweise orthogonaler, unitäre und symplektischer Symmetrie untersucht. Eine transportabhängige Verteilungsfunktion wurde analytisch berechnet und in Mikrowellengraphen getestet. Benötigte Absorptions- und Kopplungsparameter wurden experimentell aus der spektralen Autokorrelationsfunktion bestimmt. Das ermöglichte einen Vergleich zwischen Experiment und Theorie ohne freie Parameter. Es wurde eine quantitative Übereinstimmung zwischen Experiment und Theorie für alle drei Ensembles gefunden.



# Contents

<b>Abstract</b>	<b>v</b>
<b>Zusammenfassung</b>	<b>vii</b>
<b>1 Introduction</b>	<b>1</b>
<b>2 Review of basic theory</b>	<b>3</b>
2.1 Time reversal invariance . . . . .	3
2.1.1 Without spin . . . . .	3
2.1.2 Time reversal symmetry with spin-1/2 interaction . . . . .	5
2.1.3 Kramers degeneracy . . . . .	7
2.1.4 Structure of $H$ matrix for $T^2 = -1$ system . . . . .	7
2.1.5 System without time reversal invariant . . . . .	9
2.2 Gaussian ensembles . . . . .	9
2.3 An idea to realize Gaussian symplectic ensemble . . . . .	12
2.3.1 Universality in subspectra . . . . .	12
2.3.2 Quantum graph with GSE statistics . . . . .	13
<b>3 Microwave realization of Gaussian symplectic ensemble</b>	<b>19</b>
3.1 Motivation . . . . .	19
3.2 Brief theoretical overview . . . . .	21
3.2.1 Quantum graph . . . . .	21
3.2.2 Symplectic quantum graph . . . . .	23
3.2.3 Scattering properties of GSE graphs . . . . .	26
3.2.4 Single pair of bonds approximation . . . . .	28
3.3 Experimental setup . . . . .	31
3.4 Measurement results . . . . .	34
3.4.1 Transmission spectra . . . . .	34
3.4.2 Reflection spectra and resonance extraction . . . . .	36
3.5 Spectral fluctuations . . . . .	43
3.6 Level spacing distribution . . . . .	45
3.7 Spectral correlations . . . . .	49
3.7.1 Spectral two-point correlation function $R_2(L)$ . . . . .	49
3.7.2 Spectral form factor $K(\tau)$ . . . . .	50
3.7.3 Number variance $\Sigma^2(L)$ and spectral rigidity $\Delta_3(L)$ . . . . .	51
3.8 Dynamical transition from GSE via GUE to GOE . . . . .	54
<b>4 Scattering experiments on graphs with orthogonal, unitary and symplectic symmetry</b>	<b>59</b>
4.1 Motivation . . . . .	59
4.2 Theory . . . . .	60

4.3	Experimental setup . . . . .	63
4.4	Results . . . . .	65
<b>5</b>	<b>Summary</b>	<b>69</b>
<b>A</b>	<b>Appendix A</b>	<b>71</b>
<b>B</b>	<b>Acknowledgments</b>	<b>79</b>
<b>C</b>	<b>Wissenschaftlicher Werdegang</b>	<b>81</b>

# Introduction

The statistical study of spectra of quantum systems is almost as old as quantum mechanics (since 1900) itself [1]. Random matrix theory (RMT) has proven to be an extremely powerful tool to describe fluctuation properties spectra of chaotic systems [1–4]. Random matrix was initiated by Wigner [5], developed by Dyson and Mehta in the 1950s and 60s to describe the statistical properties of the spectra of complex nuclei [6], and later extended by several others [7]. For systems with time reversal symmetry (TRS) and no half-integer spin in particular there is an abundant number of studies, theoretical, numerical and experimental, showing that the universal spectral properties are perfectly well reproduced by the corresponding properties of the Gaussian orthogonal random matrix ensemble (GOE) (see Ref. [8] for a review). This is the essence of the famous Bohigas-Giannoni-Schmit (BGS) conjecture [1] which has been proved to be true by many theoretical, numerical and experimental studies. For systems with TRS and half-integer spin the Gaussian symplectic ensemble (GSE) holds instead, and for system without TRS the Gaussian unitary ensemble (GUE). There are few number of experimental studies of the spectra of systems absence of TRS showing GUE statistics [9–12] including our work [13] presented in this thesis. For the GSE, to our knowledge, there are very few studies reported GSE statistics. Alt *et al.* [14] were able to determine the spectral form factor for the GSE case by taking only every second eigenvalue of a GOE spectrum of the microwave hyperbola billiard. The RMT theoretical basis of this method was discussed in Chapter 10.6 and Chapter 10.7 of Mehta’s monograph [2]. Recently Kuemmeth *et al.* reported that the integrated level spacing distribution of the spectra of Au nanoparticles followed Wigner GSE statistics [11]. Regarding many respects of the GSE the experimental situation is still statistically insufficient.

When it comes to study the level fluctuation of a GSE system, it has been taken as essential that one has to deal with a system of a real spin-1/2 particle (system of odd number of particles with half-integer spin). In fact, the GUE statistics is observed in systems without breaking TRS [15, 16] including experimental studies [17–19]. Moreover, in Ref. [20] the possibility to realize the GOE statistics in billiards with a magnetic field, which breaks the TRS, if there an additional reflection symmetry exists. This may invoke one to think the essence of the problem. Following Dyson’s threefold way [21], to observe GSE statistics one needs only an antiunitary symmetry  $\mathcal{T}$  that squares to minus one,  $\mathcal{T}^2 = -1$ . This is sufficient to guarantee GSE statistics if the system is chaotic [22]. In addition, it leads to Kramers degeneracy in the spectrum. To realize such a symmetry without considering spin one needs special nonconventional symmetry as mentioned above to realize GUE and GOE statistics. Recently, a system with such a symmetry is proposed by Joyner *et al.* [23] in the form of a quantum Graph. Quantum graphs were introduced by Kottos and Smilansky [24] to study various aspects of quantum chaos. Throughout this thesis

we will discuss our experimental results obtained from microwave quantum graphs and compare with RMT predictions.

In chapter 3 we start to explain the theoretical bases to the experiment and then present our experimental results. Here we have analyzed the level spacing distribution of our microwave symplectic quantum graph which was constructed based on the main idea suggested by Ref. [23]. Then to examine the long range correlation of experimental eigenvalues we present results for quantities like spectral two point correlation function, spectral form factor, number variance and spectral rigidity. At the end, we will shortly present our observation of the dynamic transition of the spectral fluctuation from Gaussian symplectic ensemble (GSE) via Gaussian unitary ensemble (GUE) to Gaussian orthogonal ensemble (GOE).

In chapter 4 we briefly discuss our collaborative work with Dr. A. M. Martínez-Argüello from Mexico. At the beginning of this part we will propose a three terminal scattering device and make analytical prediction for a transport related quantity. Then we will talk about the experimental test of this prediction by means of microwave graphs with orthogonal, unitary and symplectic symmetry. At the end we will compare briefly the experimental results with corresponding theoretical predictions and discuss about the treatment of absorption and imperfect coupling.



# Review of basic theory

## 2.1 Time reversal invariance

Since this Chapter is mainly a review based on previous works [4, 8, 23], we will keep some notations to give respect for the original works.

In order to study the invariance properties of a physical system we will look at the Hamiltonian of that system. One may write the Schrödinger equation for the system of interest as

$$i\hbar\dot{\psi}(\mathbf{x}, t) = H\psi(\mathbf{x}, t) \quad (2.1)$$

A system is called invariant under time reversal operation if two given solutions of the Schrödinger Eq. (2.1)  $\psi(\mathbf{x}, t)$  and  $\psi'(\mathbf{x}, t')$  with  $t' = -t$  are uniquely related to each other [4]. The general form of the Hamiltonian of a time reversal invariant system strongly depends on whether the system is involved in spin-1/2 interaction.

### 2.1.1 Without spin

In the case of a system of a spinless particle with time reversal invariance, the Hamiltonian can be written in the following form

$$H(\mathbf{x}, \mathbf{p}) = \frac{\mathbf{p}^2}{2m} + V(\mathbf{x}), \quad (2.2)$$

where the  $V(\mathbf{x})$  is a real potential, i.e.,  $V(\mathbf{x}) = V^*(\mathbf{x})$ . The first term is proportional to the square of the momentum operator  $\mathbf{p}$ , therefore the Hamiltonian is real. In the position representation the conventional reversal is

$$t \rightarrow -t, \quad \mathbf{x} \rightarrow \mathbf{x}, \quad \mathbf{p} \rightarrow -\mathbf{p}, \quad (2.3)$$

$$\psi(\mathbf{x}) \rightarrow \psi^*(\mathbf{x}) = K\psi(\mathbf{x}). \quad (2.4)$$

where  $K$  is the complex conjugate operator, it means taking complex conjugate for all quantities following after it. If we just apply  $t \rightarrow -t$  to Eq. (2.1), we will have

$$-i\hbar\dot{\psi}(\mathbf{x}, -t) = H\psi(\mathbf{x}, -t) \quad (2.5)$$

If we simply apply  $K$  on both sides of above equation

$$K(-i\hbar\dot{\psi}(\mathbf{x}, -t)) = K(H\psi(\mathbf{x}, -t)) \quad (2.6)$$

$$i\hbar K\dot{\psi}(\mathbf{x}, -t) = HK\psi(\mathbf{x}, -t) \quad (2.7)$$

$$i\hbar\dot{\psi}'(\mathbf{x}, t) = H\psi'(\mathbf{x}, t) \quad (2.8)$$

where we employed  $KH = H$  for the real Hamiltonian. Therefore, if  $\psi(\mathbf{x}, t)$  is one solution for the Schrödinger Eq. (2.1), then  $\psi'(\mathbf{x}, t) = K\psi(\mathbf{x}, -t)$  is also a solution.

In position representation, the  $K$  operator leaves the position intact, i.e.,  $K|x\rangle = |x\rangle$  and any given eigenstate  $\psi$  of the system can be written as

$$|\psi\rangle = \sum_x \psi_x |x\rangle, \quad (2.9)$$

and when  $K$  acts on  $|\psi\rangle$

$$K|\psi\rangle = \sum_x \psi_x^* |x\rangle \quad (2.10)$$

Of course, to be general, we can define the complex conjugate operator  $K'$  with respect to any arbitrary representation  $|n\rangle$

$$K'|\psi\rangle = K' \sum_n \psi_n |n\rangle = \sum_n \psi_n^* |n\rangle \quad (2.11)$$

$K$  can always be understood in terms of  $K'$  with

$$K = UK' \quad (2.12)$$

where  $U$  is a unitary matrix and responsible for the transformation from one basis to the other.

Conventionally, the time reversal operator is denoted with  $T$ , and for a system of spinless particles we take

$$T = K \quad (2.13)$$

This operator  $T$  is defined by Eqs. (2.3), (2.4) to change the sign of the momenta (and the spin, if there is any) of all particles but to leave the positions unchanged. Since the time reversal operator  $T$  is an antiunitary operator, it might be appropriate to briefly review its properties. Firstly, it preserves the norm

$$|\langle T\psi|T\phi\rangle|^2 = |\langle\psi|\phi\rangle|^2; \quad (2.14)$$

Secondly, from its definition, it is a anti-linear operator

$$T(a\psi + b\phi) = a^*T\psi + b^*T\phi. \quad (2.15)$$

These two important properties of  $T$ , makes it antiunitary as

$$\langle T\psi|T\phi\rangle = \langle\psi|\phi\rangle^* = \langle\phi|\psi\rangle. \quad (2.16)$$

which means that the transformation by time reversal operator  $T$  on the whole system transforms the overlap of two wave functions of the system into its complex conjugate.

For a system without half-integer spin,  $T$  square is unity

$$T^2 = 1 \quad (2.17)$$

which means that  $T = T^{-1}$ . Invariant property of the system under time reversal  $T$  implies that  $T$  commutes with the Hamiltonian  $H$

$$[H, T] = 0 \quad (2.18)$$

The Hamiltonian of a system that has an operator with the above two properties given by Eq. (2.17) and Eq. (2.18) can always be real and this can be achieved without diagonalization [4]. If we just take some T invariant basis to construct the H matrix

$$H_{\mu\nu} = \langle \psi_\mu | H \psi_\nu \rangle \quad (2.19)$$

$$= \langle T\psi_\mu | TH\psi_\nu \rangle^* \quad (2.20)$$

$$= \langle \psi_\mu | THT^2\psi_\nu \rangle^* \quad (2.21)$$

$$= \langle \psi_\mu | THT\psi_\nu \rangle^* \quad (2.22)$$

$$= H_{\mu\nu}^*. \quad (2.23)$$

As a matter of fact, the Hamiltonian of a time reversal invariant system without spin-1/2 interactions can always be described by a real symmetric matrix. An orthogonal transformation transforms this real H matrix to another real  $H'$  matrix without changing its eigenvalues and Hermitian property

$$H' = OHOT^T \quad (2.24)$$

where  $O$  is an orthogonal matrix,  $OO^T = 1$ .

### 2.1.2 Time reversal symmetry with spin-1/2 interaction

In a previous section, we have seen that the time reversal operator  $T$  for a system of a spinless particle is simply the complex conjugate operator  $K$ , because the corresponding system Hamiltonian given by Eq. (2.2) is real.

Since now we are going to study the  $T$  operator for a system of spin-1/2 particle, we shall start with the typical spin Hamiltonian

$$H = H_0 + a\vec{L}\vec{S} \quad (2.25)$$

where  $\vec{L} = \vec{r} \times \frac{1}{i}\vec{\nabla}$  is the orbital angular momentum operator and  $\vec{S} = \frac{\hbar}{2}\vec{\sigma}$  is the spin angular momentum operator with Pauli spin matrices  $\vec{\sigma} = (\sigma_x, \sigma_y, \sigma_z)$ , and

$$\sigma_x = \begin{pmatrix} 0 & 1 \\ 1 & 0 \end{pmatrix}, \quad \sigma_y = \begin{pmatrix} 0 & -i \\ i & 0 \end{pmatrix}, \quad \sigma_z = \begin{pmatrix} 1 & 0 \\ 0 & -1 \end{pmatrix}. \quad (2.26)$$

These matrices obey the commutation relations

$$[\sigma_x, \sigma_y] = 2i\sigma_z, \quad [\sigma_y, \sigma_z] = 2i\sigma_x, \quad [\sigma_z, \sigma_x] = 2i\sigma_y \quad (2.27)$$

Due to the second term in Eq. (2.25), the Hamiltonian is no longer real. Therefore,  $T$  cannot just simply act as the complex conjugate operator as it did for systems of spinless particles.

Because the time reversal operator flips the sign of a spin, we have

$$T\sigma_x T^{-1} = -\sigma_x, \quad T\sigma_y T^{-1} = -\sigma_y, \quad T\sigma_z T^{-1} = -\sigma_z \quad (2.28)$$

and

$$UK\sigma_x KU^{-1} = -\sigma_x, \quad UK\sigma_y KU^{-1} = -\sigma_y, \quad UK\sigma_z KU^{-1} = -\sigma_z \quad (2.29)$$

where  $U$  is a unitary matrix. We know that only the Pauli spin matrix  $\sigma_y$  is complex, thus

$$K\sigma_x K = -\sigma_x, \quad K\sigma_y K = \sigma_y, \quad K\sigma_z K = -\sigma_z \quad (2.30)$$

and now we have specific requirements for the unitary matrix  $U$  in (2.29) as

$$U\sigma_x U^{-1} = -\sigma_x, \quad (2.31)$$

$$U\sigma_y U^{-1} = \sigma_y, \quad (2.32)$$

$$U\sigma_z U^{-1} = -\sigma_z. \quad (2.33)$$

We can construct this  $U$  matrix in terms of Pauli spin matrices,

$$U = a_0 I + a_1 \sigma_x + a_2 \sigma_y + a_3 \sigma_z, \quad (2.34)$$

where  $I$  is the  $2 \times 2$  unit matrix and  $a_0, a_1, a_2$  and  $a_3$  are arbitrary coefficients. The conditions given by Eqs. (2.31), (2.32) and (2.33) fix  $a_0 = 0, a_1 = 0, a_3 = 0$ , while  $a_2$  remains unrestricted. Therefore,  $U$  has the form

$$U = a_2 \sigma_y. \quad (2.35)$$

Unitarity  $UU^\dagger = 1$  imposes  $a_2$  to have unit modulus and it is possible to set  $a_2 = i$ , so that  $U$  for spin-1/2 particles reads

$$U = \begin{pmatrix} 0 & 1 \\ -1 & 0 \end{pmatrix}. \quad (2.36)$$

At the end, the conventional time reversal operator for a system of spin-1/2 particles will take the form

$$T = UK = i\sigma_y K = e^{i\frac{\pi}{2}\sigma_y} K. \quad (2.37)$$

We have already seen that if we flip twice the time arrow for a spinless time reversal invariant (TRI for short) system, everything should go back to itself, as shown by Eq. (2.17). Due to the spin-1/2 interaction in TRI system, the  $T$  operator has the unique form given in Eq. (2.37) and if we flip the time arrow two times,

$$T^2 = i\sigma_y K i\sigma_y K \quad (2.38)$$

$$= \begin{pmatrix} -1 & 0 \\ 0 & -1 \end{pmatrix} \quad (2.39)$$

$$= -I \quad (2.40)$$

For the wave function  $|\psi\rangle$  of spin-1/2 system one gets

$$T^2 |\psi\rangle = -|\psi\rangle, \quad (2.41)$$

thus applying  $T$  twice changes the sign. This unique feature of  $T$  for a spin-1/2 TRI system might be understood as a rotation by  $2\pi$ . If we define a rotation operator as

$$R_z(\theta) = \exp(-iS_z\theta/\hbar) \quad (2.42)$$

$$= \exp(-i\sigma_z \frac{\theta}{2}) \quad (2.43)$$

$$= \cos(\frac{\theta}{2}) - i\sigma_z \sin(\frac{\theta}{2}) \quad (2.44)$$

then for  $\theta = 2\pi$

$$R_z(2\pi) = \cos\left(\frac{2\pi}{2}\right) - i\sigma_z \sin\left(\frac{2\pi}{2}\right) \quad (2.45)$$

$$= \cos(\pi) \quad (2.46)$$

$$= -1. \quad (2.47)$$

For a spin-1/2 system, changing the sign of a wave function by  $2\pi$  rotation is equivalent to applying  $T$  two times.

### 2.1.3 Kramers degeneracy

Whenever the system has a time reversal symmetry (TRS) the full Hamiltonian always commutes with  $T$

$$[H, T] = 0, \quad (2.48)$$

it means, in other words, if  $|\psi\rangle$  is an eigenfunction of  $H$  with corresponding eigenvalue  $E$ , then  $T|\psi\rangle$  is also an eigenfunction to the same eigenvalue  $E$ . This is true regardless of whether the system does or does not have spin-1/2 interaction. However, by employing  $T^2 = +1$  one can find time reversal invariant basis vectors which obey

$$|\psi\rangle = T|\psi\rangle. \quad (2.49)$$

In contrast, in a system with antiunitary symmetry  $T^2 = -1$ , the eigenfunctions  $|\psi\rangle$  and  $T|\psi\rangle$  are always orthogonal to each other,

$$\langle\psi|T\psi\rangle = \langle T\psi|TT\psi\rangle^* \quad (2.50)$$

$$= -\langle T\psi|\psi\rangle^* \quad (2.51)$$

$$= -\langle\psi|T\psi\rangle \quad (2.52)$$

$$= 0. \quad (2.53)$$

Thus, it is easy to see that each eigenvalue of  $H$  corresponds to two linearly independent eigenfunctions  $|\psi\rangle$  and  $T|\psi\rangle$ , in other words the Hamiltonian  $H$  has doubly degenerate eigenvalues. This is the well known Kramers degeneracy.

### 2.1.4 Structure of $H$ matrix for $T^2 = -1$ system

In the previous sections we have seen that a Hamiltonian matrix is real for a system with TRI and without spin-1/2 interaction, and is complex in absence of TRI. Here, we will look at the elements of  $H$  matrix of a system with  $T^2 = -1$ . When it comes to such system,  $T$  is defined by multiplying complex conjugate operator  $K$  by  $i\sigma_y$  (see Eq. (2.37)) instead of just by  $K$  itself, as for systems with TRS  $T^2 = +1$ . Thus, it is convenient to use the quaternion  $\tau$  expressed in terms of the Pauli spin matrices as

$$\tau = i\sigma \quad (2.54)$$

with components

$$\tau_x = \begin{pmatrix} 0 & i \\ i & 0 \end{pmatrix}, \quad \tau_y = \begin{pmatrix} 0 & 1 \\ -1 & 0 \end{pmatrix}, \quad \tau_z = \begin{pmatrix} i & 0 \\ 0 & -i \end{pmatrix} \quad (2.55)$$

each of them squares minus one,

$$\tau_x^2 = \tau_y^2 = \tau_z^2 = -1, \quad (2.56)$$

and any two of them are anti-commutative to each other,

$$\{\tau_x, \tau_y\} = 0, \quad \{\tau_y, \tau_z\} = 0, \quad \{\tau_z, \tau_x\} = 0, \quad (2.57)$$

where  $\{A, B\} = AB + BA$  is the anti-commutation relation and all quaternion matrices commute with themselves

$$[\tau_i, \tau_i] = 0, \quad \text{where } i = x, y, z \quad (2.58)$$

Now by using the quaternion  $\tau$  instead of  $\sigma$ , the full system Hamiltonian of TRI system with spin-1/2 particles given by Eq. (2.25) can be written in nicer form,

$$\begin{aligned} H &= H_0 + H\tau \\ &= H_0 + H_x\tau_x + H_y\tau_y + H_z\tau_z, \end{aligned} \quad (2.59)$$

here  $H_0$  is real operator and due to the cancellation of the complex number  $i^{-1}$  in the spin-orbit Hamiltonian term in Eq. (2.25) by replacing the Pauli operator  $\sigma$  with the quaternion one  $\tau$ , operators  $H_x, H_y, H_z$  are real as well. If we utilize the quaternion operator  $\tau$ , the time reversal operator for spin-1/2 system can be rewritten as

$$T = \tau_y K = K\tau_y \quad (2.60)$$

Because of the anti-commutation relations given in (2.57),  $T$  commutes with all components of quaternion  $\tau$

$$[T, \tau_x] = 0, \quad [T, \tau_y] = 0, \quad [T, \tau_z] = 0. \quad (2.61)$$

it is then straightforward to see that the full Hamiltonian  $H$  commutes with  $T = K\tau_y$ . Due to the Kramers degeneracy the basis functions always come in pairs  $\psi$  and  $\psi' = K\tau_y\psi = T\psi$ , and where  $K$  is the complex conjugate operator. We can construct  $2 \times 2$  matrix of  $H$  by simply using two pairs of these basis vectors as

$$H_{nm} = \begin{pmatrix} \langle \psi'_n | H | \psi'_m \rangle & \langle \psi'_n | H | \psi_m \rangle \\ \langle \psi_n | H | \psi'_m \rangle & \langle \psi_n | H | \psi_m \rangle \end{pmatrix}. \quad (2.62)$$

The elements of  $H_{nm}$  are not independent of each other, but related by

$$\begin{aligned} \langle \psi'_n | H | \psi'_m \rangle &= (\langle \psi_n | H | \psi_m \rangle)^* \\ \langle \psi_n | H | \psi'_m \rangle &= -(\langle \psi'_n | H | \psi_m \rangle)^* \end{aligned}$$

If we set  $a = \langle \psi'_n | H | \psi'_m \rangle$  and  $b = \langle \psi_n | H | \psi'_m \rangle$ , then the matrix  $H_{nm}$  can be rewritten as

$$H_{nm} = \begin{pmatrix} a & -b^* \\ b & a^* \end{pmatrix} \quad (2.63)$$

with  $a, b \in \mathbb{C}$ . When we put the full Hamiltonian given by Eq. (2.59) into  $H_{nm}$ ,

$$H_{nm} = (H_0)_{nm}I + (H_x)_{nm}\tau_x + (H_y)_{nm}\tau_y + (H_z)_{nm}\tau_z, \quad (2.64)$$

here  $I$  is the  $2 \times 2$  unit matrix and the coefficients  $(H_0)_{nm}, (H_x)_{nm}, (H_y)_{nm}, (H_z)_{nm}$  are real. With this unique properties we call  $H_{nm}$  a quaternion real matrix.

It is worth-mentioning that the rank of the full Hamiltonian  $H$  matrix for systems without TRI or with TRI but without of spin-1/2 is  $N \times N$ . In comparison to this fact,

for systems with  $T^2 = -1$ , the Hamiltonian matrix has rank  $2N \times 2N$ . This is due to the Kramers degeneracy, where all basis vectors come in pairs and this makes the Hilbert space exactly two times larger. In any case, the Hamiltonian can be represented by  $N \times N$  matrix and each element is then  $2 \times 2$  quaternion real matrix. The allowed transformation which leaves the form (2.64) of matrix elements invariant is called symplectic transformation,

$$H' = SHS^R, \quad (2.65)$$

where  $S$  is symplectic,  $SS^R = 1$ . The dual of  $S$  is  $S^R$ , defined as

$$S^R = ZS^T Z^{-1} \quad (2.66)$$

here  $Z$  is a  $2N \times 2N$  block diagonal matrix and each diagonal element is a  $2 \times 2$  matrix block  $Z_{nm} = \tau_y \delta_{nm}$ .

### 2.1.5 System without time reversal invariant

For any given physical system of interest whether it has TRS or not, it is possible to write

$$H\psi = E\psi \quad (2.67)$$

where  $H$  is the system Hamiltonian and  $E$  is the corresponding eigenvalue for the eigenstate  $\psi$ . It is straightforward to construct real  $H$  matrix by using eigenstates as its basis

$$H = \text{diag}(E_1, E_2, E_3, \dots) \quad (2.68)$$

$$= H^*. \quad (2.69)$$

In general, the Hamiltonian of a system without time reversal invariance is a complex Hermitian matrix. Under the canonical unitary transformation the Hamiltonian preserves its Hermitian property and its eigenvalues will not change.

## 2.2 Gaussian ensembles

We have reviewed that for systems with time reversal invariance and absence of spin-1/2 interaction, the system Hamiltonian matrix can be represented as a real symmetric matrix. For systems without time reversal invariance, this Hamiltonian matrix is Hermitian complex, and for time reversal invariant system with spin-1/2 interaction, the corresponding system Hamiltonian matrix is a self-dual matrix which is invariant under symplectic transformation (see Sec. 2.1.4). Random matrix theory (RMT) is a suitable theory to model these system specific Hamiltonians. The basic idea is to model the system by replacing corresponding Hamiltonian with a matrix of randomly chosen elements. We are not, of course, totally free to choose the matrix elements, because the matrix elements should obey the restrictions set by the symmetry of the system of interest.

In a fully chaotic system, unlike the integrable system where the eigenvalues are uncorrelated, eigenvalues of the Hamiltonian matrix are correlated. Since the canonical transformations, namely orthogonal, unitary and symplectic, map the system Hamiltonian  $H$  to  $H'$  while leaving the corresponding matrix structure unchanged,

the correlated probability  $p(H_{11}, \dots, H_{NN})$  should also be unchanged

$$p(H_{11}, \dots, H_{NN}) = p(H'_{11}, \dots, H'_{NN}). \quad (2.70)$$

The procedure of deriving this correlated distribution are well explained in Ref. [8, 25]. For the aforementioned three classical symmetry classes, this correlated distribution reads

$$p(H_{11}, \dots, H_{NN}) = \left(\frac{A}{\pi}\right)^{N/2} \left(\frac{2A}{\pi}\right)^{N(N-1)/2} \exp\left(-A \sum_{n,m} H_{nm}^2\right) \quad (2.71)$$

for the orthogonal class which correspond to a system with anti-unitary symmetry where  $T$  squares to plus one,  $T^2 = +1$ , and

$$p(H_{11}, \dots, H_{NN}) = \left(\frac{A}{\pi}\right)^{N/2} \left(\frac{2A}{\pi}\right)^{N(N-1)} \exp\left(-A \sum_{n,m} [(H_R)_{nm}^2 + (H_I)_{nm}^2]\right) \quad (2.72)$$

for the unitary class where the system does not have time reversal symmetry and  $(H_R)_{nm}$ ,  $(H_I)_{nm}$  are the real and imaginary part of system Hamiltonian matrix  $H_{nm}$ . The last one is for symplectic class,

$$p(H_{11}, \dots, H_{NN}) = \left(\frac{A}{\pi}\right)^{N/2} \left(\frac{2A}{\pi}\right)^{2N(N-1)} \times \exp\left(-A \sum_{n,m} [(H_0)_{nm}^2 + (H_x)_{nm}^2 + (H_y)_{nm}^2 + (H_z)_{nm}^2]\right) \quad (2.73)$$

in this case the system has anti-unitary symmetry where  $T$  squares to minus one,  $T^2 = -1$  and  $(H_0)_{nm}$ ,  $(H_x)_{nm}$ ,  $(H_y)_{nm}$ ,  $(H_z)_{nm}$  are quaternion components of  $H_{nm}$ , which is a Hamiltonian matrix and invariant under symplectic transformation. For all three cases the matrix elements are Gaussian distributed and the quantity  $A$  is a constant, which can be identified in terms of the variance of diagonal or non diagonal matrix elements [8]. The above three expressions (2.71), (2.72) and (2.73) are so important that the set of random matrices where elements of each matrix obey them define the random matrix Gaussian Orthogonal Ensemble (GOE), Gaussian Unitary Ensemble (GUE) and Gaussian Symplectic Ensemble (GSE), respectively.

Since in experiments usually the energy is determined, the correlated distribution function of energies makes it easier to compare experiments than the probability distribution function of the matrix elements of Gaussian ensembles. For all three Gaussian ensembles, the correlated distribution function of energies takes the same form,

$$p(E_1, \dots, E_N) = C \prod_{n>m} (E_n - E_m)^\beta \times \exp\left(-A \sum_n E_n^2\right) \quad (2.74)$$

here  $C$  and  $A$  are constants. The quantity  $\beta$  here is the universality class index and takes values  $\beta = 1$  for GOE,  $\beta = 2$  for GUE and  $\beta = 4$  for GSE. For  $\beta = 0$  one obtains the Poisson distribution and there is no correlation between eigenvalues.

Perhaps the most frequently studied quantity in spectral correlation analysis of a system is the nearest neighbor spacing distribution function  $P(s)$ . Here,  $s$  is the distance between two neighboring energies  $s = E_{n+1} - E_n$ . If we just consider the simplest  $2 \times 2$  matrices for our Gaussian ensembles, then we will have ensembles



of eigenvalues  $E_1, E_2$ . By using expression given by Eq. (2.74) one can define the nearest neighbor spacing distribution  $P(s)$  as

$$p(s) = \int_{-\infty}^{+\infty} dE_1 \int_{-\infty}^{+\infty} dE_2 P(E_1, E_2) \delta(s - |E_1 - E_2|) \quad (2.75)$$

by utilizing the fact that total probability is normalized to one

$$\int_{-\infty}^{+\infty} p(s) ds = 1, \quad (2.76)$$

and the mean level spacing is one

$$\langle s \rangle = \int_{-\infty}^{+\infty} s p(s) ds = 1. \quad (2.77)$$

Since the matrix elements of the Hamiltonian of a symplectic system are described in terms of the  $2 \times 2$  quaternions, the matrix is  $4 \times 4$  for GSE case. One ends up with the following expressions for the three ensembles

$$p(s) = \begin{cases} \frac{\pi}{2} s \exp\left(-\frac{\pi}{4} s^2\right) & \beta = 1 \quad (\text{GOE}) \end{cases} \quad (2.78a)$$

$$p(s) = \begin{cases} \frac{32}{\pi^2} s^2 \exp\left(-\frac{4}{\pi} s^2\right) & \beta = 2 \quad (\text{GUE}) \end{cases} \quad (2.78b)$$

$$p(s) = \begin{cases} \frac{2^{18}}{3^6 \pi^3} s^4 \exp\left(-\frac{64}{9\pi} s^2\right) & \beta = 4 \quad (\text{GSE}) \end{cases} \quad (2.78c)$$

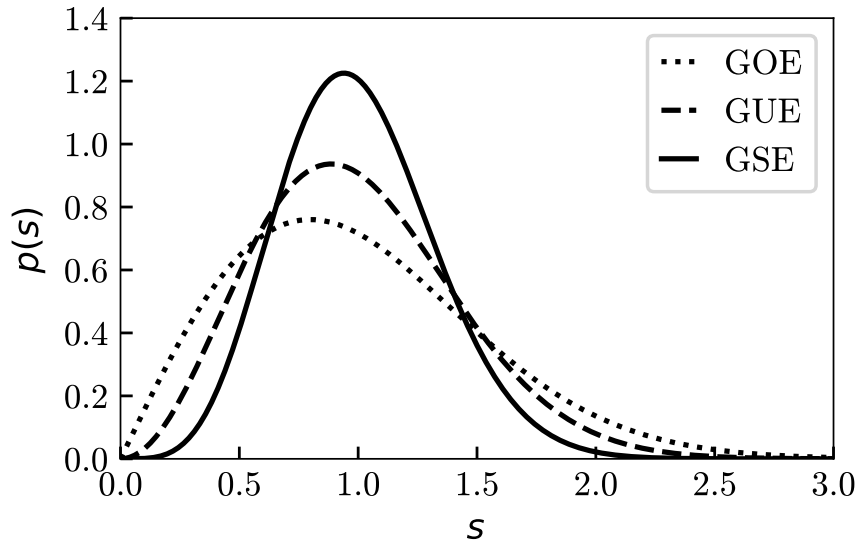


**Fig. 2.1.** Theoretical level-spacing distributions  $p(s)$  of Wigner GOE given by Eq. (2.78a), GUE given by Eq. (2.78b) and GSE given by Eq. (2.78c)

Although these distributions are obtained from Gaussian ensembles of  $2 \times 2$  matrices, they only differ little from the asymptotic level spacing distributions for ensemble of matrices with infinitely large rank (see Section 4.5 and Section 4.12 of Ref. [25] for more details). The level spacing distributions in Fig. 2.1 show different behaviors

of level repulsion for small spacing  $s \rightarrow 0$ : linear for  $\beta = 1$ , quadratic for  $\beta = 2$  and quartic for  $\beta = 4$  and overall Gaussian fall-offs for large  $s$ .

## 2.3 An idea to realize Gaussian symplectic ensemble

In this section we will study the main idea introduced in Ref. [23] to realize a system corresponding to the Gaussian symplectic ensemble.

### 2.3.1 Universality in subspectra

In quantum mechanics, the quantum mechanical symmetry operator  $U(s)$  can be defined as

$$U(g)\psi(\mathbf{r}) = \psi(g^{-1}(\mathbf{r})) \quad (2.79)$$

where  $g$  is the classical symmetry operator and the Hamiltonian of the symmetric quantum system commutes with this operator. The representation of the symmetry group  $G$  can be formed with these unitary operators  $U(g)$  and they satisfy  $U(g)U(g') = U(gg')$  for  $g, g' \in G$ . For an appropriately chosen basis of eigenfunctions of the Hamiltonian, the operators  $U(g)$  have block diagonal form and each of these blocks correspond to one irreducible representation of  $G$ . When the group  $G$  has a finite number of elements, there are only a finite number of irreducible representations labeled by  $\alpha$ , and the dimension  $s_\alpha$  of the irreducible representation  $\alpha$  is the corresponding block size. Therefore, the irreducible representation  $\alpha$  has  $s_\alpha$  energy-degenerate eigenfunctions. We can form these  $s_\alpha$  eigenfunctions into  $s_\alpha$ -dimensional vector  $|\alpha, n\rangle$ , then the symmetry operator acts on it as

$$U(g) |\alpha, n\rangle = M^{(\alpha)}(g)^T |\alpha, n\rangle, \quad (2.80)$$

where the label  $n$  is for different blocks which are corresponding to the same irreducible representation  $\alpha$  and  $M^{(\alpha)}(g)$  is the matrix representation of the operator  $g$  in the irreducible representation  $\alpha$ . Eq. (2.80) defines the subspectra of the irreducible representation  $\alpha$ . If we consider the behavior of a system under time reversal operation, all irreducible representations can be classified into one of the three types, depending on how an irreducible representation relates to its own complex conjugate. Firstly, if there does not exist a unitary matrix  $S$  such that

$$M^{(\alpha)}(g) = S^{-1} M^{(\alpha)}(g)^* S, \quad \text{for } g \in G \quad (2.81)$$

then  $\alpha$  is said to be complex. Secondly, if there exist such a unitary matrix  $S$  that satisfies the Eq. (2.81) and  $S = S^T$ , then  $\alpha$  is said to be real, meaning all  $M^\alpha(g)$  can be made real by performing some unitary transformation. Finally, if Eq. (2.81) holds true and  $S = -S^T$ , then an appropriate unitary transformation leads to a quaternion real form consisting of  $2 \times 2$  blocks  $\begin{pmatrix} a & -b^* \\ b & a^* \end{pmatrix}$  with  $a, b \in \mathbb{C}$ , thus the representation  $\alpha$  is called pseudo-real or quaternionic (see also Sec. 2.1.4).

Following Ref. [26], one can construct the transferred time-reversal operator  $\tilde{T} = ST$ , where  $T$  is complex conjugate operator and  $S$  is given by Eq. (2.81). The symmetry operator  $U(g)$  acts on the vector  $\tilde{T} |\alpha, n\rangle$  in the same fashion as it did on the vector  $|\alpha, n\rangle$  as

$$U(g)\tilde{T} |\alpha, n\rangle = M^{(\alpha)}(g)^T \tilde{T} |\alpha, n\rangle, \quad (2.82)$$

only when the irreducible representation  $\alpha$  is real or quaternionic. Thus,  $\tilde{T}$  is the correct antiunitary symmetry of the subspace associated to the irreducible representation  $\alpha$ .

According to the above analysis, such an operator  $\tilde{T}$  can be obtained for the subspace corresponding to pseudo-real or quaternionic representation. In sections 2.1.3, 2.2 we have seen that, when the antiunitary symmetry operator  $\tilde{T}^2 = -1$ , eigenvectors  $|\alpha, n\rangle$  and  $\tilde{T}|\alpha, n\rangle$  are orthogonal and in the eigenvalue spectrum one should expect the Kramer doublets and the statistics of these doublets for chaotic system should obey random matrix GSE statistics. In the next section, we will see how one can obtain the subspace associated to the pseudo-real representation.

### 2.3.2 Quantum graph with GSE statistics

Since the spectral statistics of a well connected large quantum graph agreed with the corresponding random matrix predictions for classically chaotic quantum systems [12, 24, 27], the quantum graph would be the good tool to realize a pseudo-real subspace and show GSE statistics from the corresponding spectrum. To do this one must consider a discrete symmetry group with pseudo-real irreducible representation, where isolating the necessary subspace is easier. The simplest possible one is the quaternion group  $Q8$

$$Q8 := \{\pm 1, \pm I, \pm J, \pm K : I^2 = J^2 = K^2 = IJK = -1\}. \quad (2.83)$$

All group elements can be written as products [29] involving two generators, say, for

TABLE 2.1: Multiplication table ( Cayley table ) of group  $Q8$  [28]

	1	I	J	K	-1	-I	-J	-K
1	1	I	J	K	-1	-I	-J	-K
I	I	-1	K	-J	-I	1	-K	J
J	J	-K	-1	I	-J	K	1	-I
K	K	J	-I	-1	-K	-J	I	1
-1	-1	-I	-J	-K	1	I	J	K
-I	-I	1	-K	J	I	-1	K	-J
-J	-J	K	1	-I	J	-K	-1	I
-K	-K	-J	I	1	K	J	-I	-1

instance,  $I$  and  $J$ . This group possesses 5 conjugacy classes which are  $\{1\}$ ,  $\{-1\}$ ,  $\{\pm I\}$ ,  $\{\pm J\}$ ,  $\{\pm K\}$ , therefore there are 5 different irreducible representations and since the sum of squares of dimensions of those irreducible representations is 8, their dimensions should be 1, 1, 1, 1, 2. In other words, this quaternion group has four one dimensional real irreducible representations given by  $M(I) = \pm 1$ ,  $M(J) = \pm 1$  and one two dimensional pseudo-real or quaternion irreducible representation, given by

$$M^{(5)}(I) = \begin{pmatrix} i & 0 \\ 0 & -i \end{pmatrix} \quad (2.84)$$

and

$$M^{(5)}(J) = \begin{pmatrix} 0 & 1 \\ -1 & 0 \end{pmatrix}. \quad (2.85)$$

Now if we set  $S = M^{(5)}(J)$ , then it automatically satisfies  $S = -S^T$  and it leads to

$$\tilde{T}^2 = STST \quad (2.86)$$

$$= M^{(5)}(J)TM^{(5)}(J)T \quad (2.87)$$

$$= M^{(5)}(J)M^{(5)}(J) \quad (2.88)$$

$$= -1 \quad (2.89)$$

So, this is the right symmetry group and we have to construct a quantum graph with it. To do that one could employ the so called Cayley graph of the group  $Q8$ . This is the straightforward and standard group theoretical tool in which one could encode the abstract structure of the group by using a finite set of generators which are, in our case, group elements  $I$  and  $J$ . Cayley graph can be connected by setting all group elements as vertices and connecting them by bonds which are corresponding to the generators of the group. We add arrows on bonds which are connecting the two vertices via the right generator either  $I$  or  $J$  obeying the group multiplication rule as shown in the table 2.1. The resulting graph is shown in Fig. 2.2 (a)

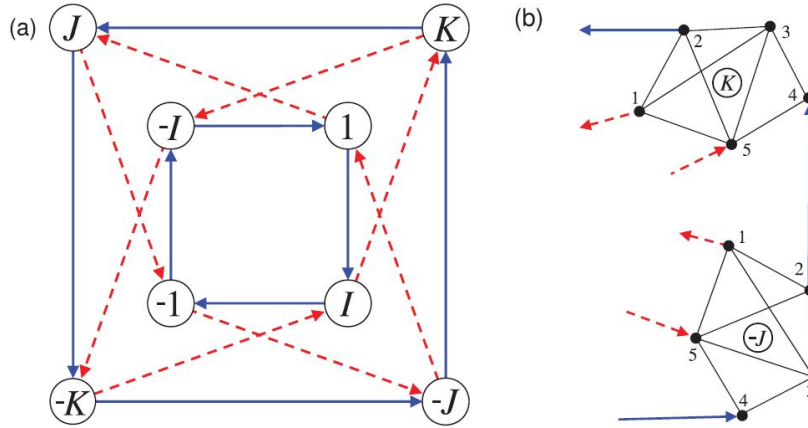


**Fig. 2.2.** (a) is the Cayley graph of the quaternion group  $Q8$ ; (b) is the part of the extended version of (a) by simply replacing each vertex with a subgraph to get more complex spectra. This figure is from Ref. [23].

where all blue bonds are corresponding to the same generator  $I$  and all red bonds are corresponding to the same generator  $J$ . For example, the bond  $b = (K, J)$  with assigned arrow shows the action of the generator  $I$  by right multiplication as  $J = KI$  and in the same manner, the arrow along the red bond  $b = (K, -I)$  shows the action of the generator  $J$  as  $-I = KJ$ . In order to treat this Cayley graph as a quantum graph, one should assign certain lengths to each bond. We set  $L_I$  for all bonds which are correspond to the group element  $I$  and  $L_J$  for all bonds which correspond to the group element  $J$ . Furthermore, the graph is symmetric with respect to left multiplication such that  $\forall g, g' \in Q8$  for a bond of length  $L_I$  defined by  $b = (g, g'I)$ , the application of any element  $h$  of  $Q8$  gives a bond  $b' = (g', g'I)$  with  $g' = hg$  of the same length  $L_I$ .

Now the resulting quantum graph can be made more complex in order to observe random matrix statistics by simply replacing each vertex with a complex enough identical subgraph as shown in Fig. 2.2 (b) and keeping the connecting rules which obeys the symmetry of original Cayley graph. Another point to be considered is that the spectrum of the whole graph includes not only the spectrum of four one dimensional irreducible representations, but also the spectrum of one two dimensional irreducible representations. To get pure GSE statistics, one has to isolate the subspace of this pseudo-real irreducible representation from the whole graph. This can be achieved by implementing the technique called quotient graph introduced in Ref. [30, 31]. The strategy is mainly based on reducing the eigenfunctions of the whole Q8 graph to one eighth of it. This quotient graph can be constructed by taking one of the eight vertices and half of each bonds attached to this vertex of the Cayley graph of Q8 group.

We can take any arbitrary vertex, for instance  $K$  and cut exactly in the middle of its directly attached bonds  $(-J, K)$ ,  $(K, J)$ ,  $(I, K)$  and  $(K, -I)$  and introduce  $v_1, v_2, v_3, v_4$  at the middle points of these bonds, respectively. The generator  $I$  takes the point  $v_2$  of bond  $(K, J)$  to the point  $v_1$  of bond  $(-J, K)$ . Similarly, the generator  $J$  brings the point  $v_4$  to the point  $v_3$ , as shown in Fig. 2.3 (b). A subspectrum associated to the pseudo-real irreducible representation can be isolated by imposing correct boundary conditions on boundaries  $v_1, v_2, v_3$  and  $v_4$  at any given position.

Let us say the wave function associated to pseudo-real irreducible representation at arbitrary position  $x$  on this quotient graph is  $\psi(x) = \langle x | \alpha, n \rangle$  with two components  $\psi_1(x)$  and  $\psi_2(x)$  which correspond to the same eigenenergy. If we simply look at the fig. 2.3 (b), we can see that the wave function  $\psi(v_1)$  is a result of the operation of  $U(I)$  on  $\psi(v_2)$  combining this with corresponding definition in Eq. (2.79) of  $U(I)$ ,

$$U(I)\psi(v_2) = \psi(I^{-1}v_2) = \psi(v_1) \quad (2.90)$$

according to the relation (2.80), we can write the action of  $U(I)$  as

$$U(I)\psi(v_2) = M^{(5)}(I)^T \psi(v_2), \quad (2.91)$$

By comparing the above two Eqs. (2.90) and (2.91) we have

$$\psi(v_1) = M^{(5)}(I)^T \psi(v_2). \quad (2.92)$$

If we set the coordinate on a bond which is increasing along the direction as shown in Fig. 2.3, then Eq. 2.92 is defined at each position along the bond, and the boundary condition holds a similar relation for the derivative of the wave function, i.e,

$$\psi'(v_1) = M^{(5)}(I)^T \psi'(v_2) \quad (2.93)$$

By going through a similar process we will have

$$\psi(v_3) = M^{(5)}(J)^T \psi(v_4) \quad (2.94)$$

$$\psi'(v_3) = M^{(5)}(J)^T \psi'(v_4) \quad (2.95)$$

The above equations from Eq. 2.92 to Eq. 2.95 are boundary conditions to isolate the pseudo-real irreducible representation on this quotient graph, which is exactly one eighth of the original Cayley graph of Q8. Since the eigenfunction of this quotient graph shown in Fig. 2.3 (b) has two components which are energy degenerate

eigenfunctions we write it in the form

$$\psi(x) = \begin{pmatrix} \psi_1(x) \\ \psi_2(x) \end{pmatrix}. \quad (2.96)$$

With this we can rewrite the Eq. (2.92) as

$$\begin{aligned} \begin{pmatrix} \psi_1(v_1) \\ \psi_2(v_1) \end{pmatrix} &= M^{(5)}(I)^T \begin{pmatrix} \psi_1(v_2) \\ \psi_2(v_2) \end{pmatrix} \\ &= \begin{pmatrix} i & 0 \\ 0 & -i \end{pmatrix}^T \begin{pmatrix} \psi_1(v_2) \\ \psi_2(v_2) \end{pmatrix} \\ &= \begin{pmatrix} i & 0 \\ 0 & -i \end{pmatrix} \begin{pmatrix} \psi_1(v_2) \\ \psi_2(v_2) \end{pmatrix} \\ &= \begin{pmatrix} i\psi_1(v_2) \\ -i\psi_2(v_2) \end{pmatrix} \end{aligned} \quad (2.97)$$

This shows the fact that the action associated with group element  $I$  is just giving phase  $+\frac{\pi}{2}$  and  $-\frac{\pi}{2}$  within each component of the wave function since

$$\psi_1(v_1) = i\psi_1(v_2), \quad (2.98)$$

$$\psi_2(v_1) = -i\psi_2(v_2). \quad (2.99)$$

For the derivative  $\psi'(x)$ , the analogous effect holds;

$$\psi'_1(v_1) = i\psi'_1(v_2), \quad (2.100)$$

$$\psi'_2(v_1) = -i\psi'_2(v_2) \quad (2.101)$$

Proceeding as before, we will rewrite Eq. (2.94) as

$$\begin{aligned} \begin{pmatrix} \psi_1(v_3) \\ \psi_2(v_3) \end{pmatrix} &= M^{(5)}(J)^T \begin{pmatrix} \psi_1(v_4) \\ \psi_2(v_4) \end{pmatrix} \\ &= \begin{pmatrix} 0 & -1 \\ 1 & 0 \end{pmatrix} \begin{pmatrix} \psi_1(v_4) \\ \psi_2(v_4) \end{pmatrix} \\ &= \begin{pmatrix} -\psi_2(v_4) \\ \psi_1(v_4) \end{pmatrix}. \end{aligned} \quad (2.102)$$

This shows that the operation corresponding to group element  $J$  connects the two components of this quotient graph eigenfunction  $\psi(x)$  such that one path which relates one component to the other gives a minus sign, while the other path leaves the component untouched, since

$$\psi_1(v_3) = -\psi_2(v_4), \quad (2.103)$$

$$\psi_2(v_3) = \psi_1(v_4) \quad (2.104)$$

and, for the derivative  $\psi'(x)$ ,

$$\psi'_1(v_3) = -\psi'_2(v_4), \quad (2.105)$$

$$\psi'_2(v_3) = \psi'_1(v_4) \quad (2.106)$$

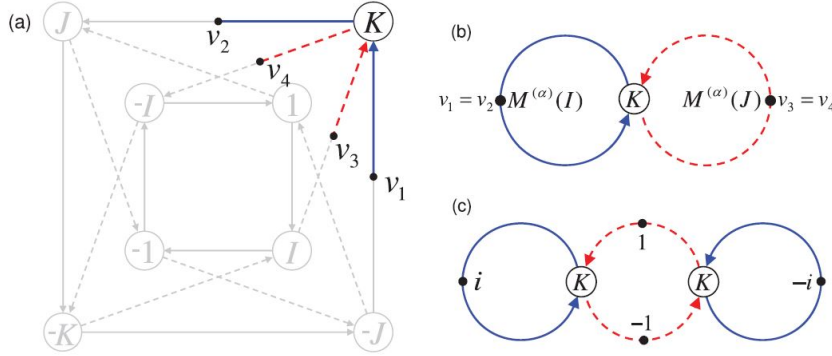


**Fig. 2.3.** (a) is the one eighth of the Cayley graph of the quaternion group Q8; (b) is the one copy of the fundamental domain with two component wave function associated with pseudo-real irreducible representation ; (c) is the two copies of the fundamental domain showed in (b) with only one component wave function. This figure is from Ref. [23].

Now it would be better to reside the two components of the wave function of the quotient graph, which is the fundamental domain, shown in Fig. 2.3 (b). We use two copies of that quotient graph as shown in Fig. 2.3 (c) to put the two components of the wave function into one of the sub quotient graph. Leads the resulting full quotient graph with one component wave function is given in Fig. 3.3 (a). In this way, these two sub-quotient graphs are coupled with each other and the resulting wave function has only one component. The resulting graph obeys the antiunitary symmetry  $\tilde{T}$  that squares to minus one, i.e,  $\tilde{T}^2 = -1$ . If we label the subgraph at the left with  $G_1$  and subgraph at the right with  $G_2$  in Fig. 3.3 (a) and any position on  $G_1$  with  $x_1$  and on  $G_2$  with  $x_2$ , then the action of  $\tilde{T}$  on the wave function  $\psi(x)$  of this whole system can be described as

$$\tilde{T}\psi(x_1) = -\psi^*(x_2), \quad (2.107)$$

$$\psi^*(x_1) = \tilde{T}\psi(x_2), \quad (2.108)$$

By this,  $\tilde{T}$  exchanges wave functions such that the wave function on one subgraph is an exact complex conjugate of the wave function on the other subgraph with a minus sign and vice versa without altering the sign. This realizes the antiunitary symmetry  $\tilde{T}$  that squares to minus one. For example,

$$\tilde{T}\tilde{T}\psi(x_1) = -\tilde{T}\psi^*(x_2) = -\psi(x_1), \quad (2.109)$$

$$\Rightarrow \tilde{T}^2 = -1. \quad (2.110)$$

Furthermore, such a symmetry introduces the Kramers degeneracy in the spectrum of this quotient graph. In Ref. [23], spectrum of this quotient graph is obtained via numerical calculation and the nearest neighbor spacing distribution  $p(s)$  of its eigenvalues agreed well with the random matrix Wigner GSE distribution as shown in

Fig. 3.1 (right). It would be important to state that this intriguing idea to realize GSE statistics without involving real spin gives more approaches to realize symplectic symmetry and GSE statistics in experiments.



# Microwave realization of Gaussian symplectic ensemble

## 3.1 Motivation

Random Matrix Theory (RMT) has achieved tremendous success in the study of statistical properties of various chaotic systems [2, 25], like hydrogen atom in a strong magnetic field, ultracold quantum gas and microwave chaotic cavities. Bohigas, Giannoni and Schmitt conjectured that the universal features of the spectrum of a chaotic system are well described by random matrix theory (RMT) [1]. The statistical fluctuation of systems with time reversal symmetry and without spin one half interaction is reproduced by corresponding statistical features of the random matrix Gaussian orthogonal ensemble (GOE). There are abundant number of experimental realizations of GOE statistics [8] including recent experiments with microwave graphs [12, 32]. For systems without time-reversal symmetry, the spectral fluctuation can be described by the random matrix Gaussian unitary ensemble (GUE). There are a few number of experimental realizations of such system [9, 11–13]. For systems with time-reversal symmetry and with spin-1/2 interactions the spectral features can be described by the corresponding features of the random matrix Gaussian symplectic ensemble (GSE). As this symmetry class is commonly associated with half-integer spin, due to such a unique feature there was no any experimental realization until a recent one [11] and my research presented in this thesis. These results are published in [13, 33].

Fig. 3.1 (left) shows the quantum graph proposed in Ref. [23]. This graph meets the two very crucial conditions, explained in detail in Sec. 2.3, which are sufficient to realize the pure GSE spectrum on this graph, and numerical studies showed that the resulting level spacing indeed follows the Wigner random matrix GSE prediction as shown in Fig. 3.1 (right).

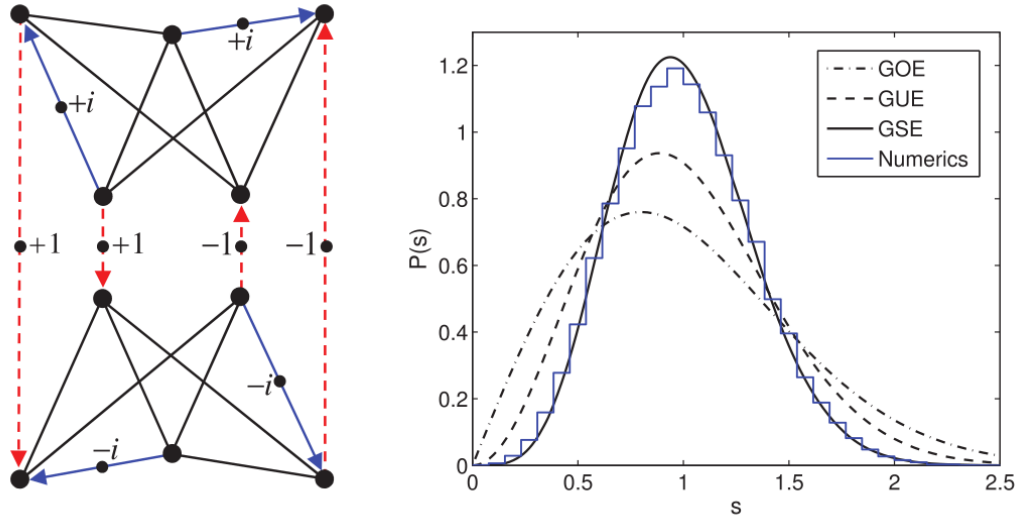


**Fig. 3.1.** The introduced quotient graph (left) and histogram of nearest neighbor spacing distribution of eigenvalues of the graph at the left side (histogram). The lines correspond to the Wigner RMT predictions for GOE, GUE and GSE. This figure is from Ref. [23].

This chapter is structured as follows: First of all, I will give the basic definition and terminologies related to quantum graphs and study some particular features of symplectic quantum graphs as well. Secondly, I will introduce the setup we have used in the experiment. Thirdly, our results about the level spacing statistics are presented. Fourthly, I will show the results concerning long range correlations such as two point correlation function  $R_2(L)$ , spectral form factor  $K(\tau)$ , number variance  $\Sigma^2(L)$  and spectral rigidity  $\Delta_3(L)$ . Lastly, we will report the dynamical transition from GSE via GUE to GOE in both experimentally and numerically. Finally, we summarize the contents presented in this chapter.

## 3.2 Brief theoretical overview

### 3.2.1 Quantum graph

Quantum graphs (networks), as an ideal tool to study quantum chaos which deals with quantum systems exhibiting chaotic motion in the classical limit, were introduced by Kottos and Smilansky [24]. Following their definition, a quantum graph is a network obtained by connecting several edges or bonds at certain number of vertices. An example of a quantum graph is shown in Fig. 3.2. A bond with the vertices  $i$  and  $j$  can be noted as  $b = (i, j)$ . In order to apply quantum mechanics, for example the Schrödinger equation, on a graph one has to determine position on any arbitrary bond on the graph, therefore a coordinate  $x_{i,j}$  is assigned to each bond  $b$  of length  $L_{i,j} \equiv L_{j,i}$ , where  $x_i$  is the distance from vertex  $i$  and similarly  $x_j$  is the distance from vertex  $j$ . The connectivity of each graph may be described in terms of its  $V \times V$  connectivity (adjacency) matrix which is denoted as  $C_{ij}$ , where  $V$  is the total number of vertices of the graph. Its matrix elements can be defined as follows:

$$C_{ij} = C_{ji} = \begin{cases} 1 & \text{if } i \text{ and } j \text{ are connected ,} \\ 0 & \text{otherwise ,} \end{cases} \quad (3.1)$$

where  $i, j = 1, 2, \dots, V$ . Quantum graph is seen as an ideal physical network where the length scale along the bonds (connecting wires) is much greater than their width.

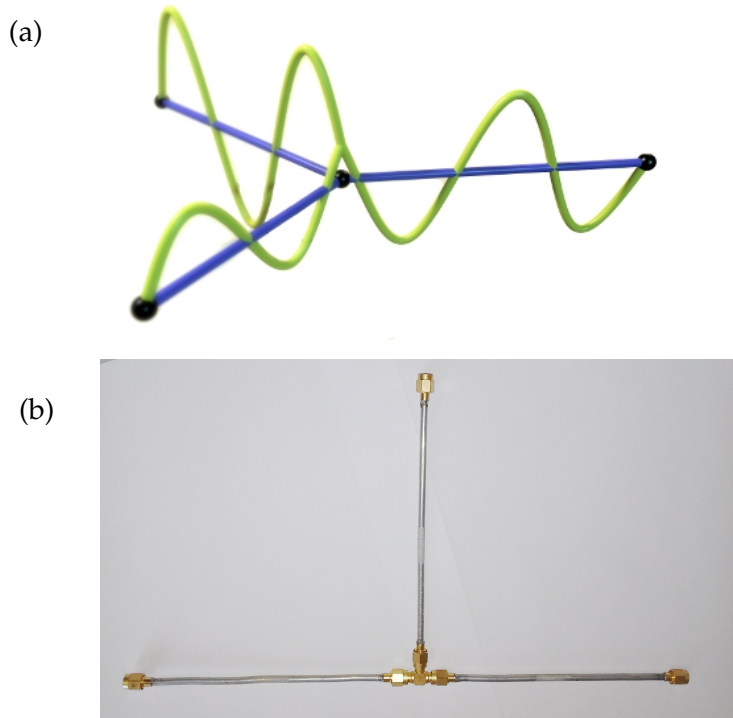


**Fig. 3.2.** An example of a quantum graph which has 4 vertices and 3 bonds. (a) is a sketch of a quantum graph and (b) is corresponding microwave quantum graph. (Lengths are not scaled)

Therefore the wave function on each bond  $b = i, j$  can be defined as a solution of one-dimensional Schrödinger equation at position  $x_i$

$$\left(-A_{ij} - i \frac{d}{dx_i}\right)^2 \psi_{ij}(x_i) = k^2 \psi_{ij}(x_i), \quad (3.2)$$

or with position  $x_j$

$$\left(-A_{ji} - i \frac{d}{dx_j}\right)^2 \psi_{ji}(x_j) = k^2 \psi_{ji}(x_j), \quad (3.3)$$

where  $A_{ij}$  and  $A_{ji}$  are the magnetic vector potentials which break time reversal symmetry for a given nonzero magnetic field. The well known solutions for the Eqs. (3.2) and (3.3) can be written as

$$\psi_{ij}(x_i) = a_{ij} e^{-i(k - A_{ij}x_i)} + b_{ij} e^{i(k + A_{ij}x_i)}, \quad (3.4)$$

and using  $x_j$

$$\psi_{ji}(x_j) = a_{ji} e^{-i(k - A_{ji}x_j)} + b_{ji} e^{i(k + A_{ji}x_j)}, \quad (3.5)$$

respectively. The two wave functions in these two representations are related via

$$b_{ij} = a_{ij} e^{-(k - A_{ij}L_{ij})}, \quad (3.6)$$

and

$$b_{ji} = a_{ji} e^{-(k - A_{ji}L_{ij})}. \quad (3.7)$$

This means that the incoming wave at vertex  $j$  coming from  $i$  is identical to the outgoing wave from the vertex  $i$  in the direction  $j$ .  $a_{ij}$  is the amplitude for propagation of the wave function from vertex  $i$  to  $j$  along the bond  $b = (i, j)$  and its corresponding time reversed propagation along this same bond is  $a_{ji}$  which is, of course, from vertex  $j$  to vertex  $i$ . The incoming and outgoing amplitudes  $a_{ij}$  and  $b_{ij}$  are related by the scattering matrix  $S$  as

$$b = Sa, \quad (3.8)$$

where  $a$ ,  $b$  are the vectors incoming and outgoing amplitudes of propagation, respectively.

Just as for quantum billiards there is a one-to-one mapping onto the corresponding microwave graphs which we are going to cover in this thesis, where the voltage at a node corresponds to the wave function and the current to the derivative of the wave function along the edges (see Ref. [12] for more details). In order to guarantee that the Schrödinger operator at Eqs. (3.2), (3.3) is self-adjoint, the wave function on the graph must satisfy two boundary conditions at the vertices. One is

$$\psi_{ij}(x_i)|_{x_i=0} = \psi_i \quad (3.9)$$

which requires that at each vertex  $i$ , the wave function assumes a value denoted by  $\psi_i$  which is independent of the bond from where the vertex is approached; the second condition is current conservation, which is specified as

$$\sum_j \left(-iA_{ij} + \frac{\partial}{\partial x_i}\right) \psi_{ij}(x_i)|_{x_i=0} = 0, \quad (3.10)$$

where the sum is over all vertices  $j$  connected to vertex  $i$ . Eq. (3.10) holds for Neumann boundary conditions, which is the case in our experiment. For microwave

graphs, these two boundary conditions are equivalent to the well-known Kirchhoff relations used mostly in electronic circuits. The continuity condition can be met by construction of the graph by properly choosing the incoming amplitude  $a_{ij}$  and outgoing one  $b_{ij}$ . However, the current conservation condition implies a system of homogeneous linear equations which has nontrivial solutions only if the determinant of the associated secular matrix  $h(k)$  vanishes,

$$\det[h(k)] = 0, \quad (3.11)$$

where the matrix elements of  $h(k)$  can be written as

$$h_{ij}(k) = \begin{cases} -\sum_{n \neq i} C_{in} \cot(kL_{in}) & \text{for } i = j, \\ C_{ij} e^{-i\phi_{ij}} [\sin(kL_{ij})]^{-1} & \text{for } i \neq j. \end{cases} \quad (3.12)$$

where  $C_{ij}$  are the elements of connectivity matrix as defined in Eq. (3.1).  $\phi_{ij} = A_{ij}L_{ij}$  is a phase resulting from a possible vector potential which breaks the time reversal invariance of the graph if a non zero magnetic field is present. The spectrum of the entire graph can then be generated from the solutions of determinant conditions given by Eq. (3.11).

### 3.2.2 Symplectic quantum graph

In Ref. [23] a quotient graph as shown in Fig. 3.3 (a) was proposed to realize GSE symmetry. It might be worthwhile to mention that the graph in Fig. 3.3 (a) is somewhat different from the one shown in Fig. 3.1 and used in Ref. [23] from which the GSE statistics was numerically achieved (the histogram at right). From the symmetry point of view both are equivalent graphs which are obeying the symmetry conditions set by Eqs. (2.98) to (2.105) on the wave function of the graph. As explained in Ref. [23], this graph has been constructed by connecting two geometrically identical subgraphs to populate two components  $\psi_1(x)$ ,  $\psi_2(x)$  of the wave function  $\psi(x)$  associated to the quaternionic representation of Quaternion group  $Q_8$ . The symmetry conditions set in Eqs. (2.98) and (2.100) are showing the fact that along the connecting bonds of one subgraph there is a phase shift of  $+\frac{\pi}{2}$  and  $-\frac{\pi}{2}$  on the second subgraph. The Eqs. (2.103) and (2.105) are setting conditions to the connection between two subgraphs via one (or more) pair (or pairs) of connecting bonds such that on one of these bonds correspond to  $\psi_2 \rightarrow \psi_1$ , gives a phase shift of  $\pi$  while the second ones associated to  $\psi_1 \rightarrow \psi_2$  does not give phase shift or zero phase shift. Such a unique configuration ensures the whole graph has a geometric inversion center. Due to these symmetry conditions, the whole graph is symmetric with respect to an antiunitary operator  $T$  that squares to minus one,  $T^2 = -1$  as shown in Eq. (2.109). The graph in Fig. 3.1 has two pairs of connecting bonds between the two subgraphs in order to get rather stronger coupling and more complex spectrum while the one in Fig. 3.3 (a) has only one pair of connecting bonds. In our experiments we will deal with both configurations. For the graph with one pair of connecting bonds shown in Fig. 3.3 the secular matrix  $h(k)$  can be written as

$$h = h_{dis} + v, \quad (3.13)$$

where the first term at the right side corresponds to the secular matrix of the disconnected subgraphs and second term accounts for the connecting bonds. It is convenient to introduce an order for rows and columns with labels the vertices on the

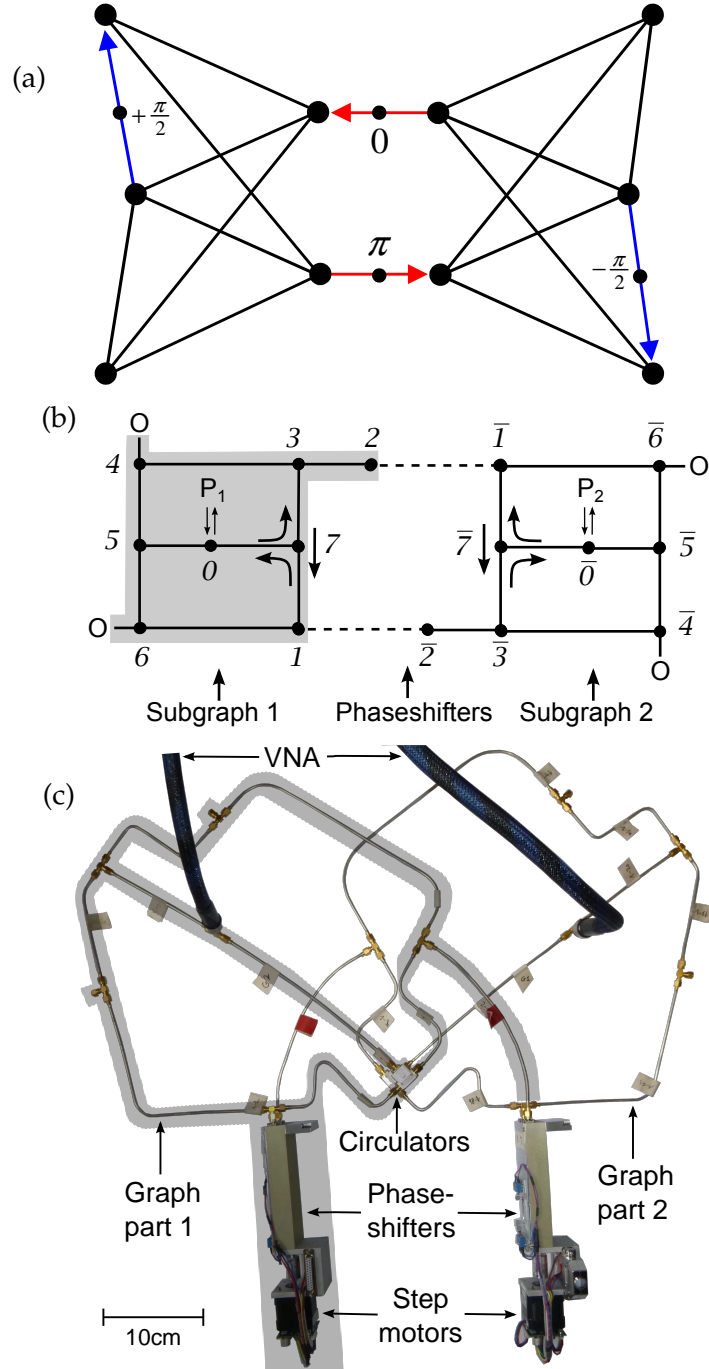


**Fig. 3.3.** (Color online) (a) Sketch of the graph proposed in Ref. [23] to study GSE statistics without spin. The four arrows denote bonds along which additional phases are acquired. (b) Schematic drawing of one of the realized microwave graphs. Subgraph 1 is highlighted by a grey background. The dashed lines correspond to phaseshifters with variable lengths. The two subgraphs contain microwave circulators at nodes 7 and  $\bar{7}$ , respectively, with opposite sense of rotation. The nodes marked by "O" are closed by open end terminators. They were used to allow for an easy realization of alternative graphs. Subgraphs 1 and 2 are connected at nodes 0 and  $\bar{0}$ , respectively, to ports  $P_1$  ( $P_2$ ) of the VNA. (c) Photograph of the graph sketched in (b) consisting of T-junctions, semirigid cables with identification tags, circulators, open end terminators, and phaseshifters with step motors. Again subgraph 1 is highlighted.

whole graph as  $\{1, 2, 3, \dots, n; \bar{1}, \bar{2}, \bar{3}, \dots, \bar{n}\}$ , where the labels without bar correspond to the vertices on subgraph 1 and labels with bar correspond to the vertices on subgraph 2. In this way the secular matrix  $h_{dis}$  can be written as

$$h_{dis} = \begin{pmatrix} h_0 & \cdot \\ \cdot & h_0^* \end{pmatrix} \quad (3.14)$$

where  $h_0$  is the secular matrix of one subgraph and  $h_0^*$  is of the second one. The empty off-diagonal elements are denoted with dots. We have seen that the symmetry conditions (2.98) and (2.100) imposed on corresponding wave functions of each subgraphs are showing the fact that the only difference between the two subgraphs is the sign of  $i$  (or phase shift of  $\frac{\pi}{2}$ ) in one of the bonds. This makes their corresponding secular matrices just complex conjugates of each other. For simplicity, consider only one pair of bonds which are connecting vertex 1 with vertex  $\bar{2}$  and vertex  $\bar{1}$  with vertex 2, respectively. Then the matrix elements of  $v$  will be

$$v_{11} = v_{22} = v_{\bar{1}\bar{1}} = v_{\bar{2}\bar{2}} = -\cot(kl) \quad (3.15)$$

$$v_{1\bar{2}} = v_{\bar{2}1} = -v_{\bar{2}\bar{1}} = -v_{\bar{1}2} = [\sin(kl)]^{-1} \quad (3.16)$$

$$v_{ij} = v_{i\bar{j}} = v_{\bar{i}j} = v_{\bar{i}\bar{j}} = 0 \quad \text{otherwise} \quad (3.17)$$

where  $l$  is the length of these two connecting bonds. Now we can extend this to the entire graph by simply changing the sequence of rows and columns to  $\{1, \bar{1}; 2, \bar{2}; 3, \bar{3}; \dots; n, \bar{n}\}$  and the resulting  $2n \times 2n$  matrix  $\tilde{h}(k)$  can be written as  $n \times n$  matrix by means of quaternion matrix (see Chap. 2) elements

$$[\tilde{h}(k)]_{nm} = [\text{Re}(h_0)_{nm} + v_{nm}] \mathbf{1} - \text{Im}(h_0)_{nm} \tau_z - v_{n\bar{m}} \tau_y \quad (3.18)$$

where

$$\mathbf{1} = \begin{pmatrix} 1 & \cdot \\ \cdot & 1 \end{pmatrix}, \quad \tau_z = \begin{pmatrix} -1 & \cdot \\ \cdot & 1 \end{pmatrix}, \quad \tau_y = \begin{pmatrix} \cdot & -1 \\ 1 & \cdot \end{pmatrix} \quad (3.19)$$

The rearranging of rows and columns does not change the determinant such that  $\det[h(k)] = \det[\tilde{h}(k)]$ . The matrix elements  $[\tilde{h}(k)]_{nm}$  commute with  $\mathcal{C}\tau_y$ , where  $\mathcal{C}$  denotes the complex conjugate operator, and hence the whole matrix commutes with the generalized time reversal operator

$$\mathcal{T} = \text{diag}(\mathcal{C}\tau_y, \dots, \mathcal{C}\tau_y), \quad (3.20)$$

where  $\mathcal{T}$  squares to minus one,

$$\mathcal{T}^2 = -1. \quad (3.21)$$

A system with such symplectic symmetry has always been considered to require a spin-1/2 particle or odd number of spin-1/2 particles. Thus, we expect Kramers doublets in the spectrum showing the signatures of GSE statistics provided the system is chaotic [25]. The idea introduced in Ref. [23] allows us to realize GSE experimentally without considering the involvement of a real spin-1/2 particle. To realize such a system with symplectic symmetry by means of graph, there are only two crucial conditions to meet: one is to preserve of two identical subgraphs with secular matrices  $h_0(k)$  and  $h_0^*(k)$  being complex conjugates of each other; the second one is a phase difference of  $\pi$  between the two bonds connecting the two subgraphs.

### 3.2.3 Scattering properties of GSE graphs

To get the spectral properties of a quantum graph, we have to connect external leads as a probe to certain vertices of the graph to perform the measurement. These external cables must be connected in a symmetric fashion such that the symplectic symmetry of the graph is unchanged. For example, if one cable connected to the vertex at the lower left in Fig. 3.3 (a), then the second cable must be connected to the vertex at upper right. Following the results of Ref. [27], for a quantum graph of  $N$  vertices and  $L$  connecting leads, the  $L \times L$  scattering matrix is given by

$$S = 2iW^T \left[ h(k) + iWW^T \right]^{-1} W - 1 \quad (3.22)$$

where  $h(k)$  is the secular matrix defined in Eqs. (3.12) and (3.13) and  $W$  is a  $N \times L$  vertices-leads matrix which corresponds to the coupling of the graph to the environment. For our experiments with microwave graphs, the coupling is ideal due to the whole standard  $50 \Omega$  impedance matching technology. Therefore the coupling constant of these external probing leads to the system of interest will be perfect. Thus the elements of coupling matrix  $W$  in Eq. (3.22) are

$$W_{vl} = \begin{cases} 1 & \text{if } l \text{ is attached to the vertex } v, \\ 0 & \text{otherwise,} \end{cases} \quad (3.23)$$

Since  $h(k)$  is hermitian, the scattering matrix  $S$  in Eq. (3.22) is unitary which ensures the current conservation condition, meaning that there are no energy losses through any existing scattering channels which are, in our case, the probing leads (or cables). Since in experiments absorption is inevitable, scattering matrices obtained by measurements will not be perfectly unitary but subunitary. One can model this finite absorption effect in terms of large number of weakly coupled fictitious channels [34]. The effects of absorption and imperfect coupling in our microwave graphs shall be discussed in a later section.

By setting the Green function  $G = h^{-1}(k)$  which has been defined as  $G = [E - H]^{-1}$  with  $H$  being the Hamiltonian of uncoupled system in the context of quantum billiards and quantum dots, the graph scattering matrix given in Eq. (3.22) may be transformed:

$$\begin{aligned} S &= 2iW^T G \frac{1}{1 + iWW^T G} W - 1 \\ &= 2iW^T G \sum_{n=0}^{\infty} (-i)^n (WW^T G)^n W - 1 \\ &= 2iW^T G W \sum_{n=0}^{\infty} (-i)^n (W^T G W)^n - 1 \\ &= 2iW^T G W \frac{1}{1 + iW^T G W} - 1 \\ &= -\frac{1 - iW^T G W}{1 + iW^T G W} \end{aligned} \quad (3.24)$$



Application of the time reversal operator  $\mathcal{T}$  to  $S$  yields

$$S = \mathcal{T}^{-1} S^\dagger \mathcal{T} \quad (3.25)$$

If there are only two channels, as in the present experiment,  $S$  is a  $2 \times 2$  matrix

$$S = \begin{pmatrix} a & b \\ c & d \end{pmatrix}. \quad (3.26)$$

For this special situation Eq. (3.25) yields

$$S = \mathcal{T}^{-1} S^\dagger \mathcal{T} = -\tau_y \mathcal{C} \begin{pmatrix} a^* & c^* \\ b^* & d^* \end{pmatrix} \mathcal{C} \tau_y = \begin{pmatrix} d & -b \\ -c & a \end{pmatrix} \quad (3.27)$$

whence follows  $a = d$  and  $b = c = 0$ , or

$$S = e^{i\alpha} \begin{pmatrix} 1 & 0 \\ 0 & 1 \end{pmatrix}. \quad (3.28)$$

The antiunitary symmetry  $\mathcal{T}$  with  $\mathcal{T}^2 = -1$  thus implies that there is no transmission. The information of the graph properties is thus encoded in the reflection phase  $\alpha$ . Let's set "0" as label to vertices where both probing cables are attached to the graph, then the elements  $S_{00}$  of  $S$  can be written as

$$S = e^{i\alpha} = -\frac{1 - iG_{00}}{1 + iG_{00}}, \quad (3.29)$$

where the phase  $\alpha$  is

$$\alpha = \pi - 2 \arctan \left( \sum_n \frac{a_n}{k - k_n} \right), \quad (3.30)$$

with  $k_n$  the zeros of secular determinant  $|h(k)|$  from Eq. (3.11) and for each of these zeros there will be a significant jump in the reflection phase. This point makes the eigenvalue extraction process much easier. It will be discussed in section related to data extraction.

### 3.2.4 Single pair of bonds approximation

Although for the proposed graph in Fig. 3.3 (a), the time reversal operator  $\mathcal{T}$  with  $\mathcal{T}^2 = -1$  ensures that all eigenvalues are doubly degenerate and nearest neighbor spacing distribution follows GSE, it does not guarantee that the coupling of two GUE subgraphs via one pair of connecting bonds is strong enough to turn these two identical GUE spectra into a complete GSE spectrum which fully obeys Wigner GSE statistics. In order to address this question the secular matrix given by Eq. (3.12) is not so convenient. Since the spectrum of a system is a set of eigenvalues of corresponding Hamiltonian, this allows us to model the whole graph in terms of a properly constructed Hamiltonian. Assuming that the Hamiltonian of one subgraph is  $H_0$  and the other one is  $\bar{H}_0$ , then the total Hamiltonian  $H$ , according to scattering theory, can be written as

$$H = \begin{pmatrix} H_0 & V\bar{V}^\dagger \\ \bar{V}V^\dagger & \bar{H}_0 \end{pmatrix} \quad (3.31)$$

where the off-diagonal blocks are responsible for the coupling of these two subgraphs. The matrix elements of the diagonal blocks, in the eigenbases of  $H_0$  and  $\bar{H}_0$ , are corresponding eigenvalues  $(H_0)_{nm} = E_n^0 \delta_{nm}$  and  $(\bar{H}_0)_{nm} = \bar{E}_n^0 \delta_{nm}$  of disconnected subgraphs with Neumann boundary conditions at the coupling point, respectively. In the off-diagonal blocks,  $V$  and  $\bar{V}$  are  $N \times K$  matrices with  $N$  being the size of  $H_0$  and  $\bar{H}_0$  and  $K$  being the number of bonds which connect the two GUE subgraphs. In the bases of  $H_0$  and  $\bar{H}_0$ , the elements of  $V$  and  $\bar{V}$  are just values of the wave functions of each disconnected subgraphs at the coupling points, i.e.,  $V_{nk} = \psi_n(x_k) = \psi_{nk}$  and  $\bar{V}_{nk} = \bar{\psi}_n(x_k) = \bar{\psi}_{nk}$ , respectively. Since for the graph we are taking into account  $H_0$  and  $\bar{H}_0$  are complex conjugate of each other, their corresponding eigenvalues are equal,  $E_n^0 = \bar{E}_n^0$  and  $V_{nk}^* = \bar{V}_{nk}$ . If we consider the case in Fig. 3.3, where only one pair of connecting bonds is used to couple the two subgraphs, we may set a zero phase shift on the bond  $b = (\bar{2}, 1)$  and phase shift of  $\pi$  on the other bond  $b = (2, \bar{1})$  at their coupling points. For this specific case, the corresponding off-diagonal elements in Eq. (3.31) are

$$\begin{aligned} [V\bar{V}^\dagger]_{nm} &= V_{n1}\bar{V}_{m\bar{2}} + e^{i\pi}V_{n2}\bar{V}_{m\bar{1}} \\ &= \psi_{n1}\psi_{m2} - \psi_{n2}\psi_{m1} = \tilde{V}_{nm} \end{aligned} \quad (3.32)$$

and  $[\bar{V}V^\dagger]_{mn} = -\tilde{V}_{nm}^*$ . When it comes to the nearest neighbor spacing distribution, despite the small difference [4] between random matrix prediction where infinitely large matrices are considered and the one by Wigner approximations, we will follow the latter since such a small deviation is hard to distinguish in most experimental studies and they are exact for  $2 \times 2$  Gaussian random matrix ensembles. In the spirit of Wigner approximation we will restrict the size of the total Hamiltonian  $H$  in Eq. (3.31) to 2. However, due to the  $2 \times 2$  quaternions the actual  $H$  matrix is  $4 \times 4$  for the symplectic case. Without loss of generality, we set the average energy to be zero,

$$E_{1/2} = \pm \frac{a}{2}. \quad (3.33)$$

To find the eigenvalues of  $H$ , we will write down its characteristic polynomial as follows

$$\chi(E) = \begin{vmatrix} E - a/2 & \cdot & \cdot & -\tilde{V}_{12} \\ \cdot & E + a/2 & \tilde{V}_{12} & \cdot \\ \cdot & \tilde{V}_{12}^* & E - a/2 & \cdot \\ -\tilde{V}_{12}^* & \cdot & \cdot & E + a/2 \end{vmatrix} \quad (3.34)$$

$$= \left[ E^2 - (a/2)^2 - |\tilde{V}_{12}|^2 \right]^2. \quad (3.35)$$

We can clearly see that  $\chi(E)$  is the product of two identical quadratic equations. This means that all eigenvalues are doubly degenerate which is exactly the manifestation of Kramers degeneracy. The distance of two eigenvalues is

$$s = \sqrt{a^2 + 4|\tilde{V}_{12}|^2} \quad (3.36)$$

and distribution of these nearest neighbor spacing is

$$p_0(s) = \left\langle \delta \left( s - \sqrt{a^2 + 4|\tilde{V}_{12}|^2} \right) \right\rangle \quad (3.37)$$

After some calculation, for more details look at Ref. [13], one ends up with

$$p_0(s) = 16s^4 \int_0^\pi d\varphi \sin \varphi \cos^2 \varphi e^{-\frac{4}{\pi}s^2 \cos^2 \varphi} \hat{K}_1(\pi s \sin \varphi) \quad (3.38)$$

where  $\hat{K}(t) = tK(t)$  is a modified Bessel function. The factor  $t$  compensates the singularity of  $K(t)$  for  $t \rightarrow 0$ .  $\hat{K}(t)$  is regular for  $t \rightarrow 0$ ,  $\hat{K}(0) = 1$ .  $p_0(s)$  thus shows a quartic level repulsion for  $s \rightarrow 0$ , just as the Wigner GSE distribution. From the definition of  $p_0(s)$  by Eq. (3.37), the total probability is one, as it should be:

$$\int_0^\infty p_0(s) ds = 1 \quad (3.39)$$

but the mean level spacing must be one as well and it does not fulfill this condition automatically as

$$\bar{s} = \langle s \rangle = \int_0^\infty s p_0(s) ds = 1.32417 \dots \quad (3.40)$$

Thus, by rescaling  $p_0(s)$  one gets the new level spacing distribution

$$p(s) = \bar{s} p_0(\bar{s}s) \quad (3.41)$$

which has the mean level spacing of one. In Fig. 3.4 this distribution based on one pair of connecting bonds approximation is compared with both random matrix simulation and Wigner GSE distribution, which is given as

$$p_{\text{GSE}}(s) = \frac{2^{18}}{3^6 \pi^3} s^4 \exp \left( -\frac{64}{9\pi} s^2 \right). \quad (3.42)$$

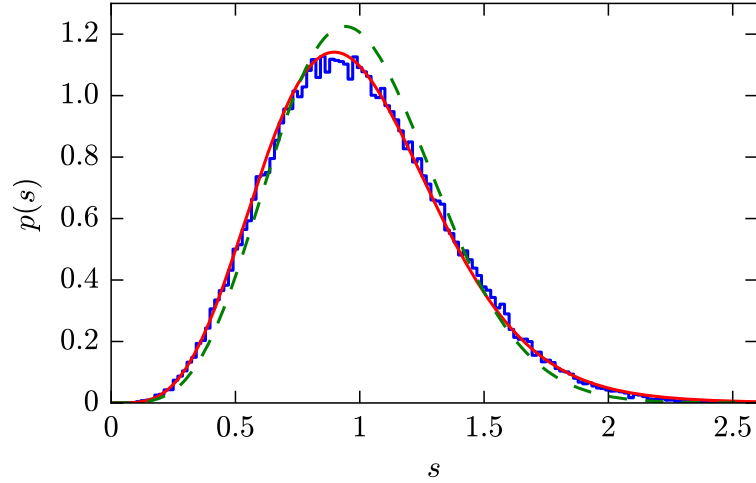


**Fig. 3.4.** Level-spacing distribution for the single pair of bonds approximation (solid line), see Eq. (3.41), and for the Wigner GSE distribution (dashed line), see Eq. (3.42). In addition the result of a random matrix simulation is shown (blue histogram). In the simulations we created random matrices for an ensemble of 2000 matrices of size  $1000 \times 1000$ , i.e. the size of each GUE subblock  $H_0$  and  $\tilde{H}_0$ , see Eq. (3.31), was  $500 \times 500$ . We used only the central 0.1 fraction of each spectrum to calculate the distribution of next-nearest neighbor spacings  $s$  in order to avoid problems with the non-constant density of states.

From this figure we can see that there is a good agreement in overall features between the Wigner GSE distribution and the distribution based on one pair of bonds approximation, most importantly for the case of small spacing (for example,  $s < 0.5$ ). Furthermore, the histogram shows the result of random matrix simulation with matrices of size 1000 which is much larger than the size of the Hamiltonian matrix  $H$  which is used to derive the analytic result of one pair of connecting bonds approximation. We can see that the histogram follows with the analytical distribution, Eq. (3.41) very well. To get such a good agreement between the two-bond approximation and random matrix simulation and to clearly distinguish the two-bond approximation approach from Wigner GSE distribution, in random matrix simulation  $10^5$  Kramers doublets had been needed which is hard to achieve in experiments. Lastly, this two-bond approximation approach allows us to study how many pairs of such connecting bonds are sufficient to get full overlap of the spectrum of whole GSE graph with Wigner GSE statistics, at least numerically. We will discuss this point in a later section.

### 3.3 Experimental setup

In order to realize the Gaussian Symplectic Ensemble (GSE) experimentally on the basis of the idea proposed by Joyner *et al.* [23] we have performed measurements on microwave graphs. One of the two important ingredients of the idea introduced by Ref. [23] is the phase shift of  $+\frac{\pi}{2}$  on bonds of one subgraph and phase shift of  $-\frac{\pi}{2}$  on the second subgraph. Since we did not know an easy way to achieve this condition, we took the main idea but proceeded in a somewhat different way namely by constructing two geometrically identical subgraphs with an opposite direction of propagation in the two subgraphs by means of two circulators. One can see this clearly from the sketch and photograph of whole GSE graph in Fig. 3.3 (b), (c), respectively.

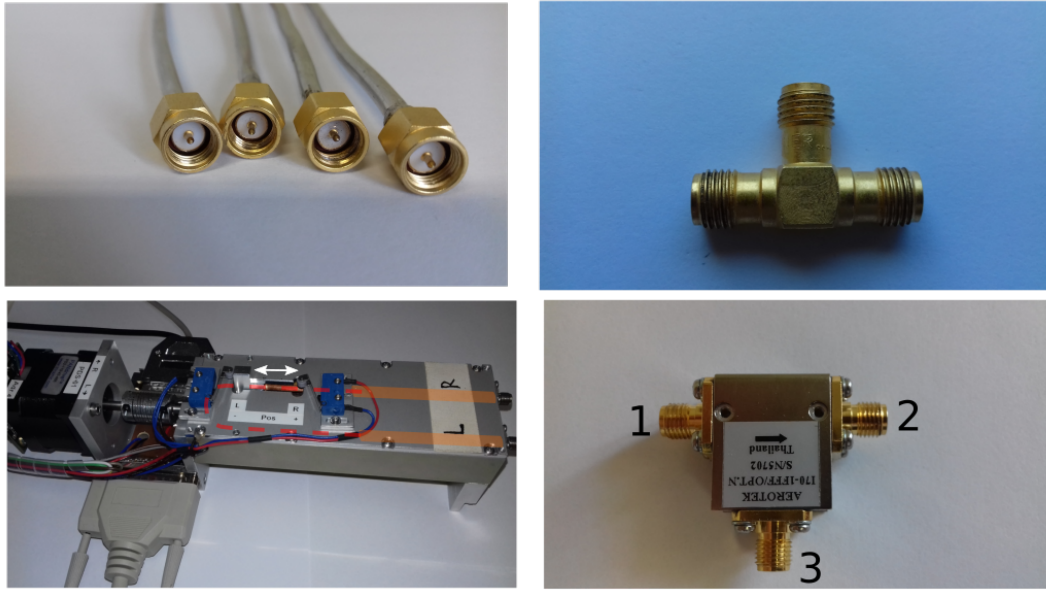


**Fig. 3.5.** Components we used to build our microwave graphs. Upper left are coaxial cables; Upper right shows a T-junction; Lower left is a mechanical phase shifter; Lower right is a circulator (the arrow indicates that propagation from port 1 to port 2 is allowed and the opposite is forbidden).

A circulator is a microwave device which allows the microwave to propagate in specific directions only. For instance, the circulator shown in Fig. 3.5 allows the microwave from port 1 to port 2, from port 2 to port 3 and from port 3 to port 1 only. This will be done, in reality, by allowing maximum propagation in allowed directions and minimum propagation in forbidden directions. This feature can also be seen from the scattering matrix of a circulator,

$$S = \begin{pmatrix} 0 & 0 & 1 \\ 1 & 0 & 0 \\ 0 & 1 & 0 \end{pmatrix}. \quad (3.43)$$

As most experimental devices our circulator is not perfect. The performance of the circulator used in the experiment is illustrated in Fig. 3.6. The transmission from port 2 to port 1,  $|S_{12}|^2$ , is suppressed and transmission in opposite direction  $|S_{21}|^2$  is maximum within the documented operating frequency range from 6-12 GHz.

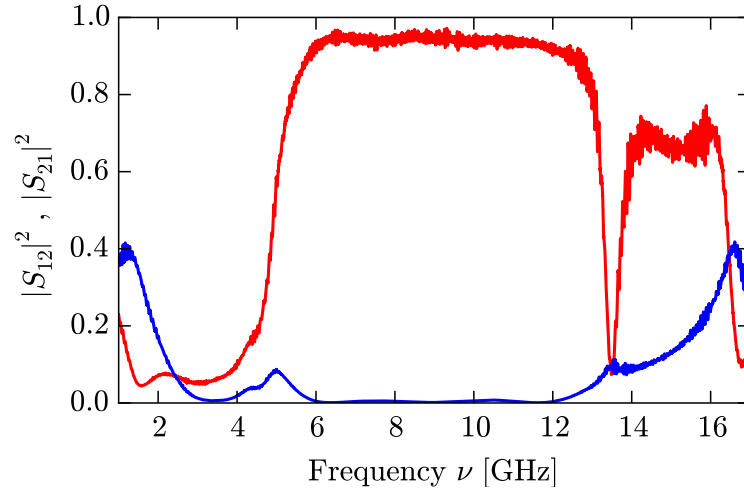


**Fig. 3.6.** Example of the performance of a circulator. Port 3 of the circulator showed in Fig. 3.5 is terminated with standard  $50\ \Omega$  terminator to avoid the possible reflection from port 3. Transmission coefficients  $|S_{21}|^2$  (red line) and  $|S_{12}|^2$  (blue line) are measured.

Due to this unique feature, the circulators break the time reversal symmetry, resulting in identical GUE spectra on each of the two subgraphs with the same secular matrix  $h_0$ . However, the two circulators have to be connected in opposite sense of rotations (see the circulator at vertices 7 and  $\bar{7}$  in Fig. 3.3 (b)) which turns one secular matrix  $h_0$  of one subgraph into its complex conjugate  $h_0^*$  on the second. Such special configuration of the two subgraphs has the same effect as the  $\pm \frac{\pi}{2}$  phase shifts on the bonds of the two subgraphs.

The second ingredient is the phase difference of  $\pi$  between connecting bonds of two subgraphs. At the beginning, we will start with the case of only one pair of connecting bonds. We have tried several different approaches. First we inserted pairs of circulators in each bond oriented such that the waves could pass in both directions. Both open ends were closed with short-end terminators in one bond and open-end terminators in the other one. This should result in the desired phase difference of  $\pi$  between the two bonds. The idea worked in principle, but the phase difference showed up not to be  $\pi$ , but deviated several percent from  $\pi$  as shown in Fig. 3.7. Probably this could be improved by a suitable fine-tuning of the terminators, but for the moment we discarded this option. Next we tried it with I&Q vector modulators (Model: M2L-68N-S from GT Microwave Inc.) which allow to adjust arbitrary phases and amplitudes in transmission. The observed spectra, however, showed up to be mostly independent on the phase difference imposed. We attribute this to the large insertion loss of 12 dB of the IQ modulators.

Since these two approaches did not work properly, we have overcome this problem by using two mechanical phase shifters which change the phase of microwave within the bonds by changing its length (like in a trombone). Fig. 3.5 shows a photo of one phase shifter with a sketch of its internal U shaped moving part.

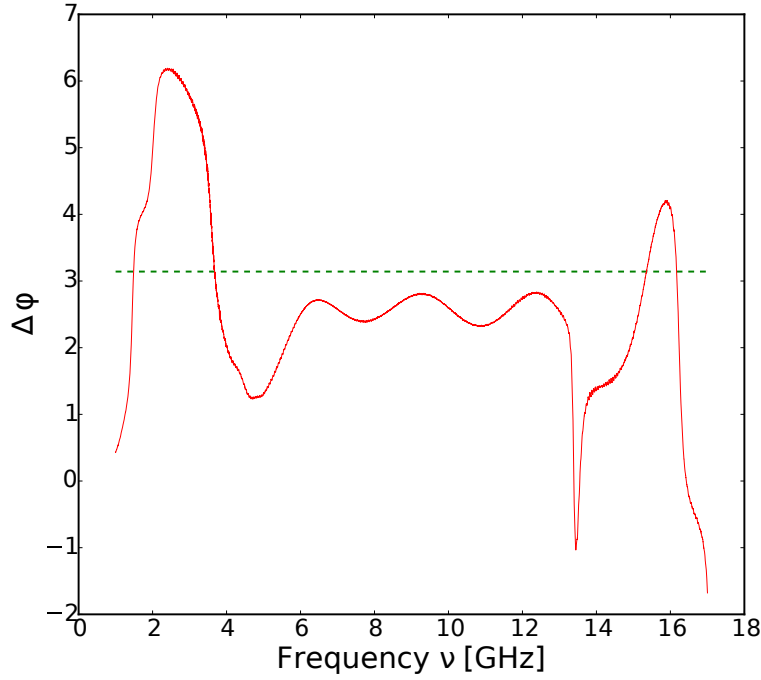


**Fig. 3.7.** The phase difference obtained by using a pair of circulators. The red line is the measured phase difference and the green dashed line is the  $\Delta\varphi = \pi$ .

In this approach the phase shift  $\Delta\varphi$  not only depends on the change of optical length  $\Delta l$ , but also on frequency  $\nu$  via the relation,

$$\Delta\varphi = k\Delta l = \frac{2\pi\nu}{c}\Delta l, \quad (3.44)$$

where  $k$  is the wave number and  $c$  is the velocity of light within the phaseshifter.

A sketch of the microwave graph we used in our experiments is given in Fig. 3.3 (b) to make it easier for the reader to visualize the connection of whole graph and a photograph of one of the graphs used in the experiment. Microwave coaxial semi-rigid cables with SMA (see Fig. 3.5) connectors by Huber and Suhner EZ-141 are used as bonds of the graph and are connected by T-junctions (see Fig. 3.5) representing the vertices. The inner and outer radii of the cables are 0.45 and 1.45 mm, respectively, hence, below 34.8 GHz only the lowest TEM is propagating (see Sec. 8.8 of Ref. [35]). The index of refraction of the cables is 1.43. The phase shifters (ATM, P1507) are equipped with step motors to control the length change automatically. The measurements of all scattering matrix elements were performed with an Agilent 8720ES vector network analyzer (VNA) by coupling its two probing ports to symmetrically equivalent vertices of the two subgraphs. The corresponding reflection and transmission amplitudes will be denoted in the following by  $S_{ij}$ ,  $i, j = 0, \bar{0}$ . Since the operating frequency range of our circulators (Aerotex I70-1FFF) is from 6 GHz to 12 GHz as shown in Fig. 3.6, our data analysis process will be focused on this frequency interval. Both the step motor and vector network analyzer are controlled via a computer program.

### 3.4 Measurement results

#### 3.4.1 Transmission spectra

We have seen that the two subgraphs are complex conjugates of each other by construction. Since the phase difference between the two connecting bonds depends on both the microwave frequency  $\nu$  and the length change  $\Delta l$  introduced by phase shifters, in order to get the phase difference of  $\pi$  we have performed series of measurements, where each single measurement is taken for a constant  $\Delta l$ . Then the spectrum of this one measurement contributes only once the condition of  $\Delta \varphi = \pi$  or we may meet equivalent conditions such as  $\Delta \varphi = 3\pi, \Delta \varphi = 5\pi \dots$  if the frequency is high enough that length variation is larger than several half wavelengths.

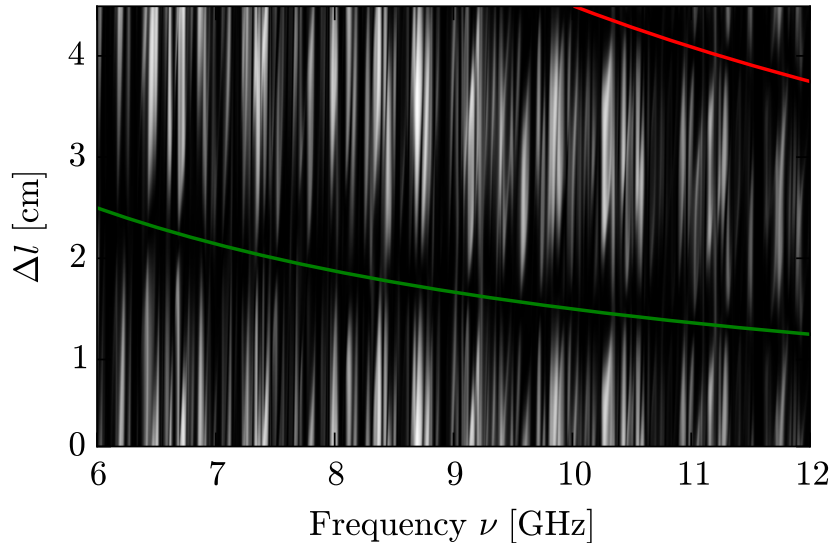


**Fig. 3.8.** Transmission  $|S_{00}|^2$  in dependence of frequency in a gray scale, where the white corresponds to the maximum and the black corresponds to the minimum. Spectra for different  $\Delta l$  are stacked on top of each other. The green and red solid curves of  $\Delta l = c/(2\nu)$  and  $\Delta l = 3c/(2\nu)$  correspond to  $\Delta \varphi = \pi$  and  $\Delta \varphi = 3\pi$ , respectively.

Fig. 3.8 shows a set of transmission spectra, which is the modulus square of the transmission coefficient  $|S_{00}|^2$ , in gray scale with white corresponding to maximum transmission and black corresponding to minimum transmission. This plot is obtained by stacking altogether 396 spectra above of each other, where each spectrum corresponds to a single  $\Delta l$  of the phase shifter. The range of  $\Delta l$  is from  $\Delta l_{min} \approx 0$  to  $\Delta l_{max} = 4.4$  cm. The green line corresponds to  $\Delta l = c/(2\nu)$  and the red line corresponds to  $\Delta l = 3c/(2\nu)$ , which means  $\Delta \varphi = \pi$  and  $\Delta \varphi = 3\pi$ , respectively.

In order to get the transmission spectrum  $S_{00}$  for constant phase from Fig. 3.8 we made a transformation from  $\Delta l$  to  $\Delta \varphi$  by using the relation given by Eq. (3.44). The rearranged spectrum is shown in Fig. 3.9. By using the Eq. (3.44), one can calculate the possible maximum phase difference  $\Delta \varphi$  for a given frequency  $\nu$  as

$$\Delta \varphi_{max} = \frac{2\pi \Delta l_{max}}{c} \nu \quad (3.45)$$

The inaccessible region set by this limit is left white. From the plot one can clearly see that the pattern on the spectrum has  $2\pi$  periodicity as expected. We can see that



at positions  $\Delta\varphi = \pi$  (green line) and  $\Delta\varphi = 3\pi$  (red line) the transmission has a minimum. This is exactly what is expected for graphs with symplectic symmetry by Eq. (3.28), where for a GSE graph the total transmission between symmetry equivalent vertices  $i$  and  $\bar{i}$  is zero. In our experiment it is not exactly zero, but strongly suppressed.

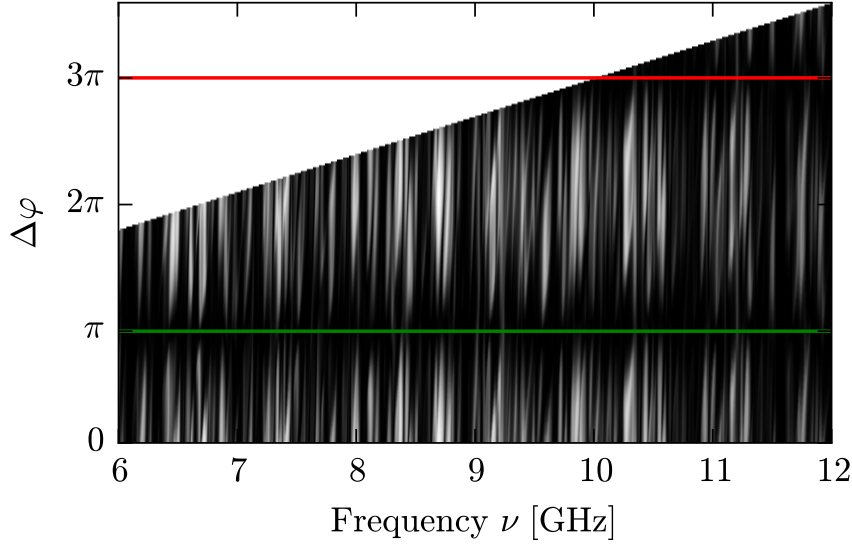


**Fig. 3.9.** The same data set with Fig. 3.8, but rearranged to yield spectra for constant  $\Delta\varphi$ . The green and red solid line corresponds to constant  $\Delta\varphi = \pi$  and  $\Delta\varphi = 3\pi$ , see Eq. (3.44).

This can be understood as an interference effect. All possible transmission paths between coupling points  $0, \bar{0}$  to VNA probes  $P_1, P_2$ , respectively, come in pairs and due to the special configuration of two circulators the propagation on one path is opposite to its symmetrically corresponding partner. And one of this path goes through one of the phase shifter while the second one goes through another phase shifter and it results in lengths differences  $\Delta l$  between these paired paths. Depending on their corresponding phase difference  $\Delta\varphi$ , there will be a constructive or destructive interference on bonds. It can be directly observed from Fig. 3.9 that the regions at  $\Delta\varphi = 0$  and  $\Delta\varphi = 2\pi$  are much brighter and the regions at  $\Delta\varphi = \pi$  and  $\Delta\varphi = 3\pi$  are much darker. Apart from this, the periodicity of the pattern is easily observable: for instance, the patterns just below the lines at  $\Delta\varphi = \pi$  and  $\Delta\varphi = 3\pi$  and in the frequency window from 9.5 GHz to 12 GHz are repeated.

In order to better visualize this interference effect, the whole transmission spectrum is projected onto  $\Delta\varphi$  axis. The result is shown in Fig. 3.10. At  $\Delta\varphi = \pi$  and  $\Delta\varphi = 3\pi$  the transmission, which must be zero as predicted by Eq. (3.28), is not exactly zero, but about 10% of the maximum transmission. This is reflecting the inevitable tolerances in the construction of the two subgraphs. The dashed green and red lines are corresponding to  $\Delta\varphi = \pi$  and  $\Delta\varphi = 3\pi$  when the  $\Delta\varphi$  is obtained from the length change  $\Delta l$  introduced by two phase shifters and lengths of the cables. We can see that these dashed lines are not at the minima of frequency averaged transmission  $\langle |S_{00}|^2 \rangle_\nu$ . In comparison, there are also solid green and red lines which are exactly at the minima which are obtained by calibration of the length change in the experiment. The discrepancy between calculated and measured phase differences  $\Delta\varphi$  associated to the dashed and solid lines, respectively, correspond to an optical length of about 1.4 mm. Such a length difference is small enough to be neglected

when we consider the total typical optical length of 3.3 m of the graphs used in the measurements. This is also within the range of tolerance provided by the mechanical workshop. Therefore, we can rely on this approach to adjust the  $\Delta l$  such that the transmission minima are exactly at the position  $\Delta\varphi = \pi$  and  $\Delta\varphi = 3\pi$ .

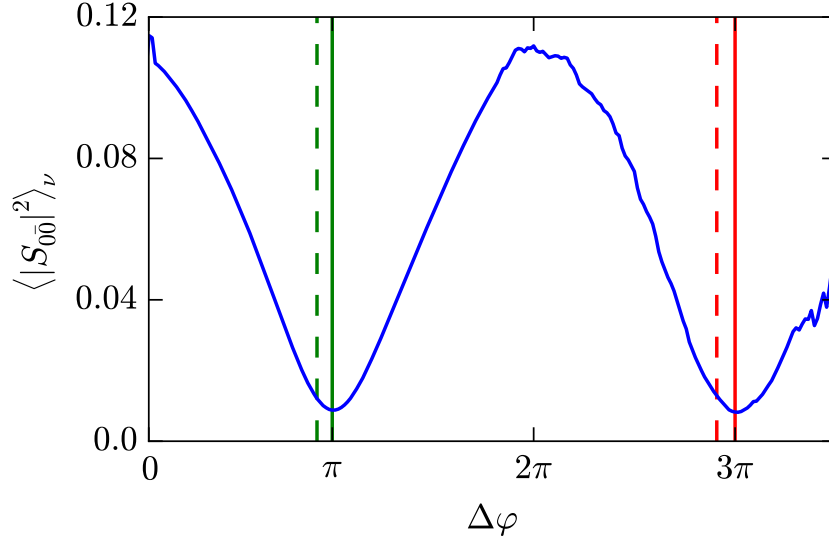


**Fig. 3.10.** Transmission  $\langle |S_{00}|^2 \rangle_\nu$ , averaged over all frequencies  $\nu$  between 6 and 12 GHz in dependence of  $\Delta\varphi$ . See the text for the discussion of the solid and dotted lines.

### 3.4.2 Reflection spectra and resonance extraction

In the description of the experimental setup we have stated that the two circulators on subgraphs break time reversal symmetry and turn the disconnected subgraphs into GUE graphs, meaning that spectral statistics of each of these disconnected subgraphs obeys corresponding statistical features of Gaussian unitary random matrix ensembles. Breaking the time reversal symmetry by means of special techniques and devices by introducing vector potential to the system is not unusual in microwave experiments. As the first experimental study of quantum graphs with microwaves Hul *et al.* [12] have used a Faraday isolator on one bond to break time reversal symmetry. In a recent work [32] by our group, a microwave circulator, exactly of the type we used in our graph, was used on one bond of quantum microwave graphs to break time reversal symmetry. In the case of quantum billiards [9, 10] ferromagnetic stripes are used to break time reversal invariance. In order to check that the two disconnected subgraphs are identical we have measured reflection spectra of them and observed that indeed they have identical spectra within the limits of our measurement resolution. To make sure that the subgraph with one circulator, just the half of the graph shown in Fig. 3.3 (b) (c) without phase shifter, obeys GUE statistics we have prepared 7 different graphs by simply replacing one of the cables with different lengths and extracted their resonances from corresponding reflection spectra. Fig. 3.11 shows the obtained nearest neighbor spacing distribution which agrees well with Wigner GUE distribution given by Eq. (2.78b). This check guarantees that we have indeed constructed two identical GUE subgraphs.

Let us now look into the spectra of the whole combined graph with a single pair of connecting bonds. In Fig. 3.9 and Fig. 3.10 we have observed that there is almost

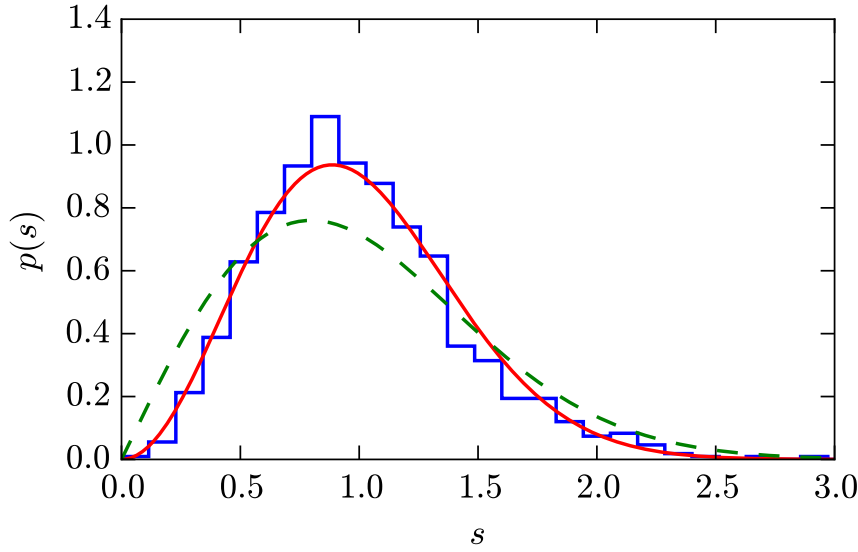


**Fig. 3.11.** Level-spacing distribution for the disconnected subgraph. The results of 7 different subgraphs have been superimposed to improve the statistics. The green dashed line corresponds to the Wigner GOE distribution given by Eq. (2.78a) and the red solid line corresponds to the Wigner GUE distribution given by Eq. (2.78b).

zero transmission at  $\Delta\varphi = \pi$  and  $\Delta\varphi = 3\pi$ , as already expected by Eq. (3.28). Therefore, we rather analyzed the reflection spectra, more precisely the modulus square of the reflection coefficient  $|S_{00}|^2$  measured at vertex 0 coupled to Port1 (P1 in the sketch of the setup, see Fig. 3.3) of Vector Network Analyzer (VNA). Again, as we did for the transmission spectra, we stacked all 396 individual reflection spectra above of each other for constant length change  $\Delta l$  of phase shifters. We then rearranged the data set to the constant phase difference  $\Delta\varphi$  which we plotted in gray scale with dark being the minimum reflection and white being the maximum reflection. The result is shown in Fig. 3.12 in the working range of circulators from 6 GHz to 12 GHz. From this figure one may not see too much information. Thus to see more details we plotted a smaller frequency window from 7.37 GHz to 7.712 GHz (the left shaded region in Fig. 3.12) shown in Fig. 3.13 (a) where the part of the spectra below the red line is repeated on the top of the spectra (the part above the white horizontal line) to emphasize the periodicity of the spectra as a function of the phase difference  $\Delta\varphi$  with a period of  $2\pi$ . Each dip in a reflection spectrum is a resonance which is encoded as dark and the corresponding frequency is the eigenfrequency. We have additionally edited the figure by adding red and green dashed lines along the dark patterns which are eigenfrequencies periodically shifting with the change of  $\Delta\varphi$  just to lead the readers eye.

Due to the limited dynamic range of our phase shifters we are only able to directly measure the spectra including the repetition of the pattern at around  $\Delta\varphi = \pi$  for the frequency windows of around 9.8 GHz to 12 GHz, this is limited by the relation (3.45), which can be seen from the Fig. 3.9 and Fig. 3.12. We have zoomed in a smaller frequency window ranges 11.3 GHz to 11.75 GHz (the right shaded region in Fig. 3.12) shown in Fig. 3.13 (b). From this figure we can clearly see that spectra around  $\Delta\varphi = \pi$  have been repeated full details after exactly  $2\pi$  of change in phase difference  $\Delta\varphi$ , it means around  $\Delta\varphi = 3\pi$ .

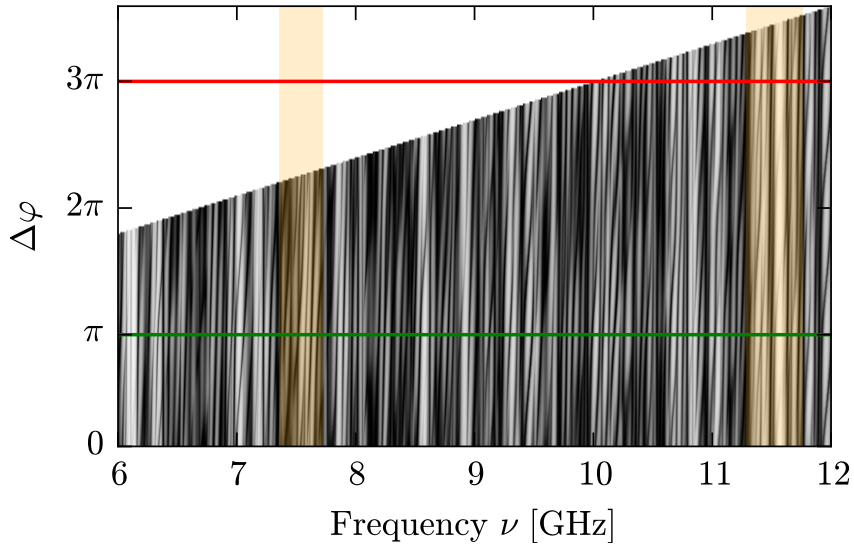


**Fig. 3.12.** Reflection  $|S_{00}|^2$  spectra for constant  $\Delta\varphi$ . The green and red solid line corresponds to constant  $\Delta\varphi = \pi$  and  $\Delta\varphi = 3\pi$ , see Eq. (3.44). The shaded regions are presented in more detail in Figs. 3.13 (a), (b), respectively.

One can easily notice that at some regions two nearby resonances are hard to be resolved or in some cases resonances just disappear for short ranges of  $\Delta\varphi$ . And such cases are observed more at higher frequency range. Hence in the measurement a resonance may be overlooked for some unknown reasons or the reflection amplitude is so small to be observed, meaning that the resonance must be there because a resonance is defined by the graph itself and can not be destroyed or created by the parametric change of the phase difference  $\Delta\varphi$  which can only shift a resonance and may also effect its intensity.

If we look more closely at Fig. 3.13 (a) and Fig. 3.13 (b) starting from  $\Delta\varphi = 0$  along the increasing of  $\Delta\varphi$  up to the top of the figures, one notices that the resonances are experiencing a breathing pattern, forming Kramers doublets at the  $\pi$  line in Fig. 3.13 (a) and at  $\pi$  and  $3\pi$  lines in Fig. 3.13 (b). If we guide our eyes along the red and green dashed lines with the increasing  $\Delta\varphi$ , then it can be noticed that two singlets are coming close each other along  $\Delta\varphi = 0 \rightarrow \Delta\varphi = \pi$  (and  $\Delta\varphi = 2\pi \rightarrow \Delta\varphi = 3\pi$ ), exactly at  $\Delta\varphi = \pi$  (and  $\Delta\varphi = 3\pi$ ) they overlap each other and form the Kramers doublets. We have observed such Kramers doublets along the whole frequency window from 6 GHz to 12 GHz for each single graph. When  $\Delta\varphi$  departs from this position(s) the doublets are split, see Fig. 3.13. Such dynamics is better visible in Fig. 3.14 showing the evolution of individual spectra in orange. The dashed orange line corresponds to the spectrum at  $\Delta\varphi = \pi$  with resonances, Kramers doublets, at 7.40092 GHz, 7.45191 GHz, 7.51599 GHz, 7.57799 GHz, 7.625 GHz, 7.679 GHz which are marked with blue dots in Fig. 3.14. The full reflection spectrum from 6 GHz to 12 GHz of one GSE graph is given in Appendix (A).

There is a complete equivalence to the Zeeman splitting of spin doublets: In our experiment the antiunitary symmetry is destroyed when departing from the  $\pi$  (and

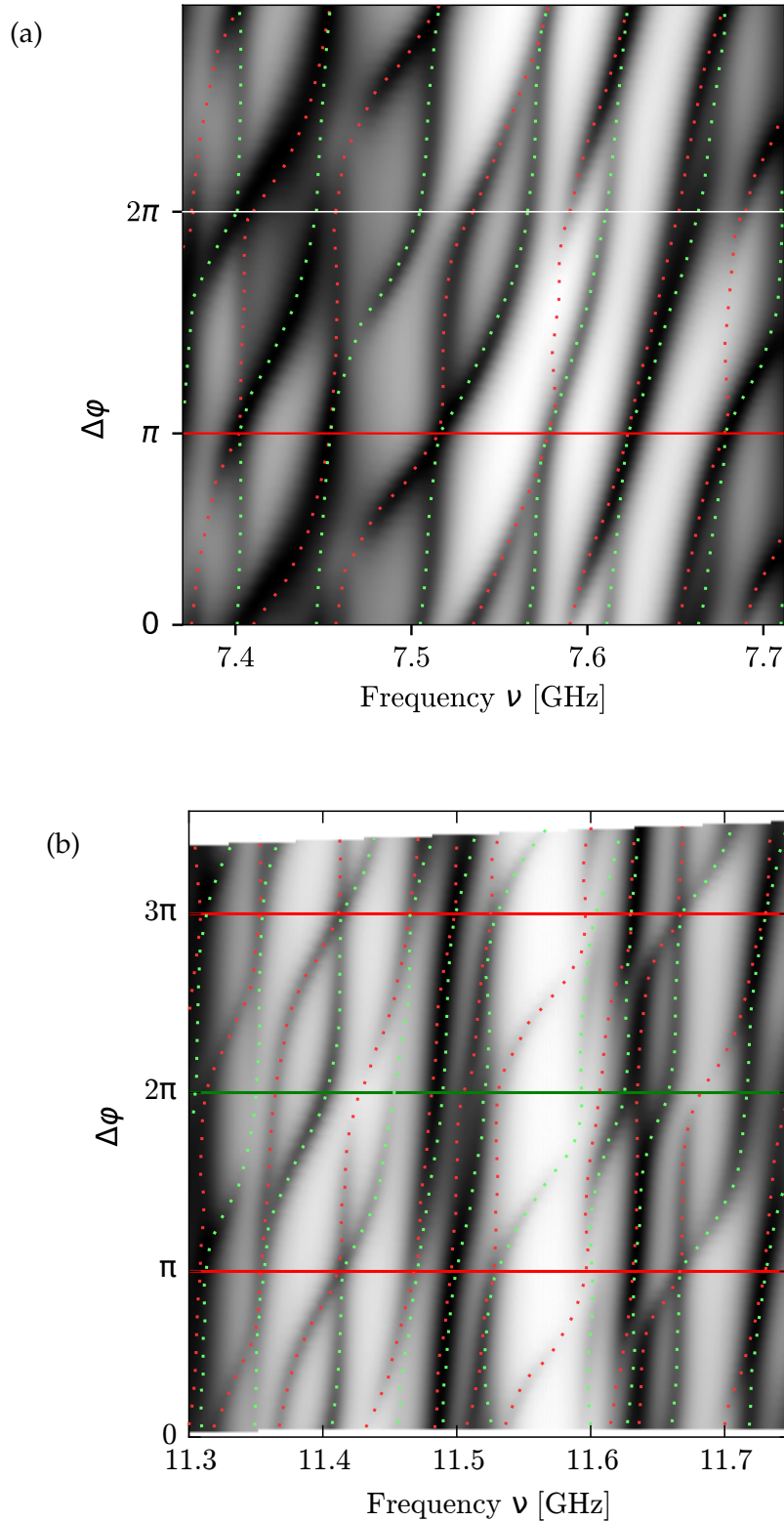


**Fig. 3.13.** Reflection  $|S_{00}|^2$  in dependence of frequency in a gray scale. The spectra for different  $\Delta\phi$  are stacked onto each other. (a) At frequency range from 7.37 - 7.712 GHz. The bottom part of the spectra has been repeated at the top, the part above the white line, to emphasize the periodic structure. The colored dotted lines are guides to the eye to emphasize the parametric dynamics of the resonances. (b) At higher frequency range from 11.3 - 11.75 GHz. In this window the  $2\pi$  periodic repetition is directly observed from the measurement data.

$3\pi$ ) line, whereas for conventional spin systems this effect occurs when a magnetic field is applied. Such a Zeeman splitting of Kramers doublets is reported in Ref. [11], where magnetic field dependence of resonances of a chaotic quantum dot, a nominally 10 nm diameter gold colloid, is studied. This demonstrates that we have been successful in constructing a graph with antiunitary symmetry  $\mathcal{T}$  with  $\mathcal{T}^2 = -1$ . The mutual distances between the doublets are same within 20%. This shows a clear tendency towards an constant level spacing at the  $\pi$  line, which is one of the fingerprints of a GSE spectrum.

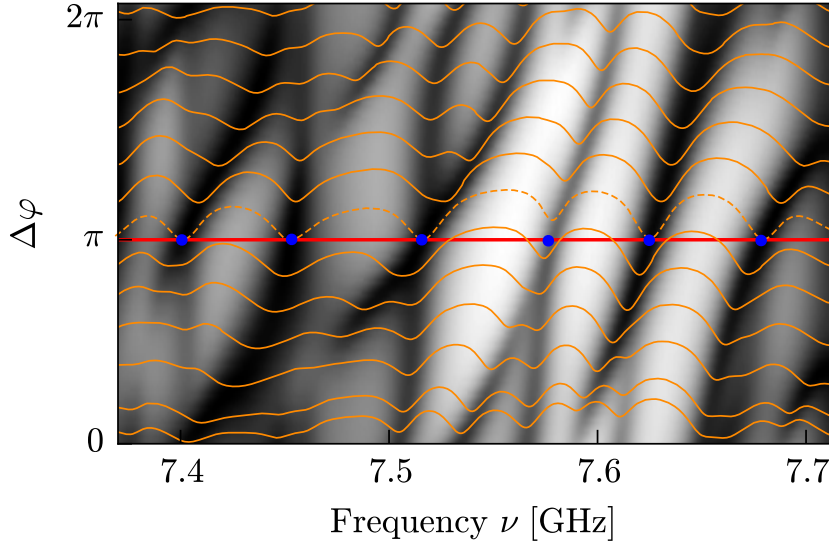


**Fig. 3.14.** Reflection  $|S_{00}|^2$  in dependence of frequency in a gray scale. The spectra for different  $\Delta\varphi$  are stacked onto each other. This shows the same window shown in Fig. 3.13 (a) the part below the white line. The orange lines are showing individual spectra  $|S_{00}|^2$  for several constant values of  $\Delta\varphi$ , the dashed orange line corresponds to the spectrum at  $\Delta\varphi = \pi$ , which is separately analyzed in Fig. 3.15. The six Kramers doublets are marked with blue dots and the solid horizontal red line is for constant  $\Delta\varphi = \pi$ .

In Sec. 3.2.3 we have seen that the scattering matrix of a graph with symplectic symmetry does not have transmission, and reflection coefficients are unity, see Eq. (3.28). The effect of absorption within the bonds of the graph was not considered. Taking absorption into account each eigenfrequency results in a dip in the reflection spectrum. In standard methods, one has to fit the resonance to Lorentzian line shape in order to obtain the associated eigenfrequency. By Eq. (3.28) it was shown that the most information about the GSE graph properties are stored in the reflection phase such that each zeros of the determinant of the graph secular matrix  $|h(k)|$  give jumps in the reflection phase. Fig. 3.15 shows the spectrum of the same six Kramers doublets at  $\Delta\varphi = \pi$  of Fig. 3.13 (a). The upper panel shows the modulus square of reflection coefficient  $|S_{00}|^2$ . In the middle panel the corresponding reflection phase  $\alpha_{00}$  is plotted. One can see that the phase jumps are not so sharp as one may expect, but with some finite width due to the unavoidable absorption within the bonds. The imperfect calibration is responsible for the overall decrease of the phase along the frequency  $\nu$ . The phases introduced during the propagation of the microwave along the whole graph are possible to be removed via calibration. Nonetheless, some phases resulting from the connectors are not easy to handle. The

plot in lower panel shows the modulus square of the phase derivative, where the contribution from the overall decrease had been subtracted before. We can clearly note that now all the six resonances are much more narrower than the directly obtained original resonances showed in upper panel.

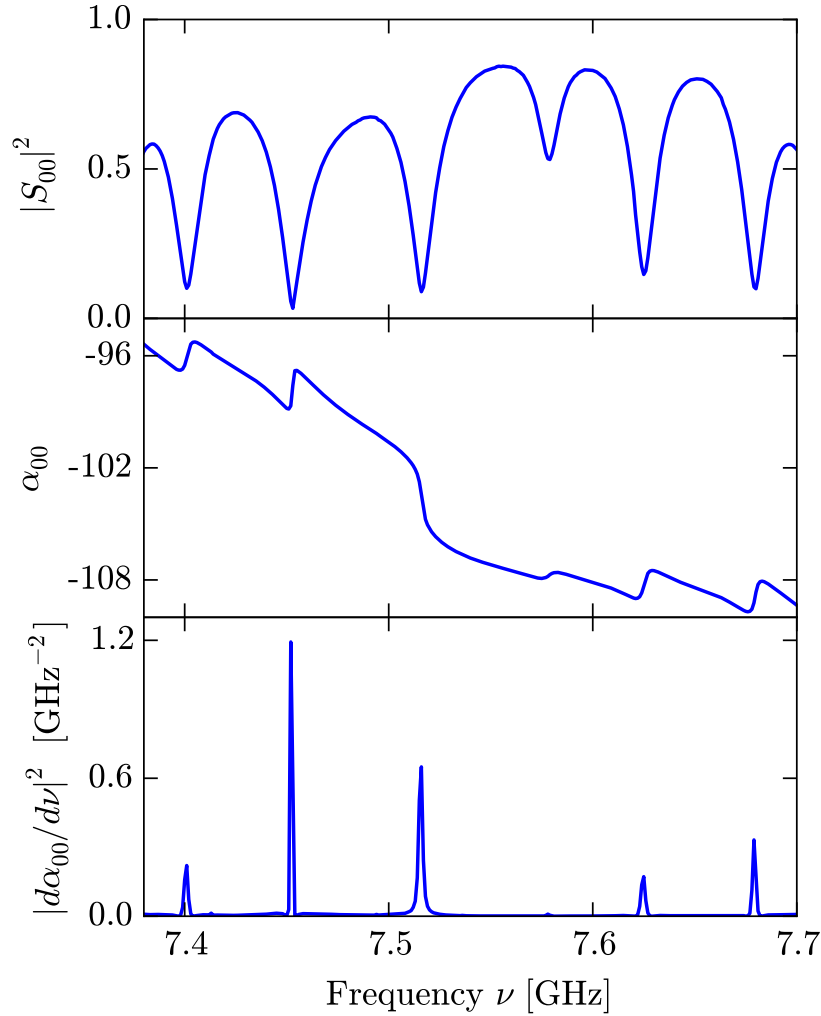


**Fig. 3.15.** (top) Reflection  $|S_{00}|^2$  for  $\Delta\varphi = \pi$  for the same frequency range as in Fig. 3.13 (b). (middle) Phase  $\alpha_{00}$  of the reflection. (bottom) Squared phase derivative  $|d\alpha_{00}/d\nu|^2$ .

This method provides us with a more efficient approach towards the process of the resonance extraction than performing Lorentzian line fitting as mentioned earlier. By setting a discrimination level to the value of modulus squared phase derivative  $\langle |S_{00}|^2 \rangle_\nu$  along the whole range of 6 to 12 GHz approximately 90 % of all resonances can be automatically identified in few minutes. As we can see from the lower panel of Fig. 3.15 that due to absorption there are some resonances which can not be identified automatically, for instance the one at 7.57799 GHz, due to the very small value of  $\langle |S_{00}|^2 \rangle_\nu$ . Then we can look at the dynamics of the singlets at both sides of  $\Delta\varphi = \pi$  line. The  $\Delta\varphi$  depending evolution of the left member of a doublet is marked with a red dotted line and the corresponding right member is marked with



a green dotted line, see Fig. 3.13 (a) and Fig. 3.13 (b). While  $\Delta\varphi$  is approaching the  $\pi$  line or  $3\pi$  line, the left and right singlets gradually come close to each other and eventually at  $\pi$  or  $3\pi$  merge into one doublet. By this way, we can identify several more resonances. Due to the imperfection in our setup around 10% of doublets do not appear exactly at  $\Delta\varphi = \pi$ , but somewhere above or below the  $\Delta\varphi = \pi$  line. This means that there two already separated singlets at  $\Delta\varphi = \pi$  line instead a doublet. In this case we have taken the eigenfrequencies of these two singlets and taken the average of them as the eigenfrequency of the corresponding doublet. The possible uncertainty such introduced to the resonance frequency is around 10 % of the mean level spacing. As a result, this will not give noticeable disturbances to the level spacing distributions and correlation of energy levels, as we shall show later.

The Weyl law for a quantum graph of total length  $L$  given in Eq. (3.48) at the next section allows us to predict the average number of resonances in certain frequency range. Here  $L$  is the optical length  $L = n L_g$  with  $L_g$  being the total geometrical length of the graph and  $n$  the refractive index of the dielectric material filled between the inner and outer conductors, in our case  $n = 1.43$ . By comparing the expected average number given by the Weyl law and experimentally extracted resonances we conclude that in average 7.5 % of eigenvalues have been missed. In microwave experiments, it is hard to avoid few percent of missing levels. In our experiment the following two sources may be responsible for missed eigenvalues: one, misidentification of nearby resonances by a single one; second, when the coupling point of the VNA port is very close to the nodal line, resonances will be missed. Thanks to the strong repulsion between neighboring eigenvalues of GSE spectrum the eigenvalues are well isolated and tend to equally spacing as can be seen from the Fig. 3.13. Therefore the first case can be excluded. For the second case it is possible to avoid missing level or decrease the number of possible missing levels by repeating the measurement at different coupling point of the system to the VNA port. However, as will be seen later, the results are sufficient to show the GSE behavior.



### 3.5 Spectral fluctuations

After the extraction of the eigenfrequencies of Kramers doublets for the whole graph, we are able to calculate the density of states by the standard definition

$$\rho(k) = \sum_i \delta(k - k_i), \quad (3.46)$$

where  $k = (2\pi\nu)/c$  is the wave number of the microwave and  $c$  is the vacuum velocity of light. With this level density we can construct a staircase function  $N(k) = \int \rho(k') dk'$  which fluctuates around a smoothly varying part which is described by the Weyl law for the mean level density and one fluctuating part as

$$N(k) = N^{Weyl}(k) + N^{fluc}(k), \quad (3.47)$$

This is actually a special case of Gutzwiller's trace formula [36] (see also chapter 7 and 8 of Ref. [8] for more details).

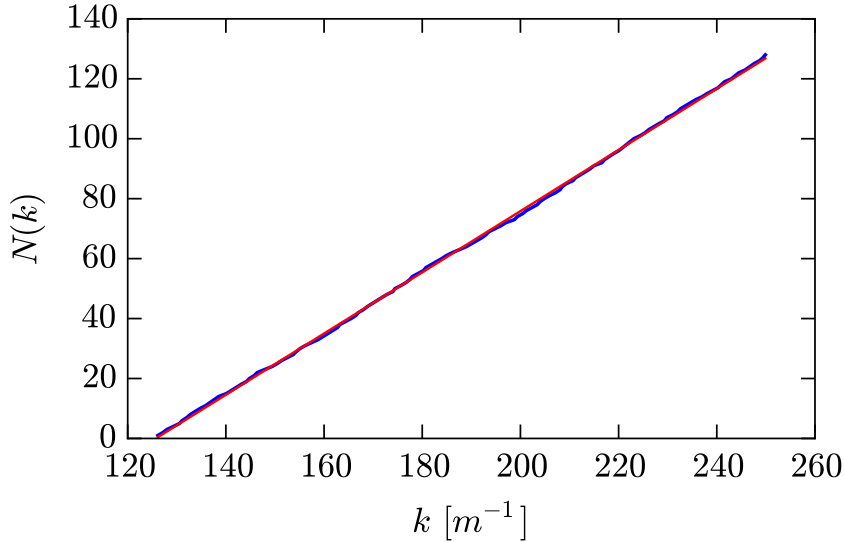


**Fig. 3.16.** The blue solid line is the staircase function  $N(k)$  for set of eigenvalues corresponding to Kramers doublets of one symplectic graph. The total length of the graph is 334.05 cm and total of 128 eigenvalues are identified. The red straight line is for the linear fitting to extract the smoothed part of  $N(k)$ .

Fig. 3.16 shows the staircase function  $N(k)$  of one of our graphs. The mean of this staircase function  $N^{Weyl}(k)$  can be obtained by simply fitting a line  $N^{Weyl}(k) = a_{exp} k + b$  to the experimentally measured staircase function  $N(k)$ . The slope of the best fit line is  $a_{exp} = 1.0210$ . For a quantum graph, the Weyl formula  $N^{Weyl}(k)$  is given as

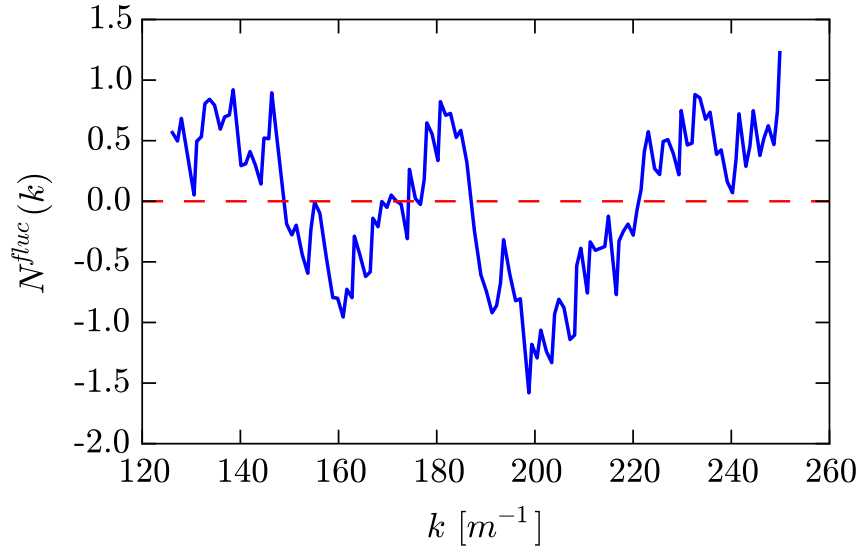
$$N^{Weyl}(k) = \bar{N}(0) + \frac{L}{\pi} k, \quad (3.48)$$

where  $\bar{N}(0) = 1/2$  and  $L$  is the total length of the graph being considered. Note that Kottos and Smilansky [24] have used a somewhat different definition, as they have defined directed graphs thus doubling the length of their graphs. For the case of quantum billiards the Weyl law depends on area and perimeter of the billiard. However, a quantum graph is one dimensional system, thus the Weyl law only

depends on the length of the whole graph. The measured total optical length of the graph is 334.05 cm resulting in a theoretical value for the slope from the Weyl law of  $a_{th} = 1.0633$ , which is close to the slope of experimental staircase function. The experimental data agreed well with the Weyl law given in Eq. (3.48), and the fluctuation of the staircase function around the mean is hardly noticeable.

The fluctuating part  $N^{fluc}(k)$  can be obtained by subtracting the smoothed part  $N^{Weyl}(k)$  from the experimental staircase function  $N(k)$  as

$$N^{fluc}(k) = N(k) - N^{Weyl}(k) \quad , \quad (3.49)$$



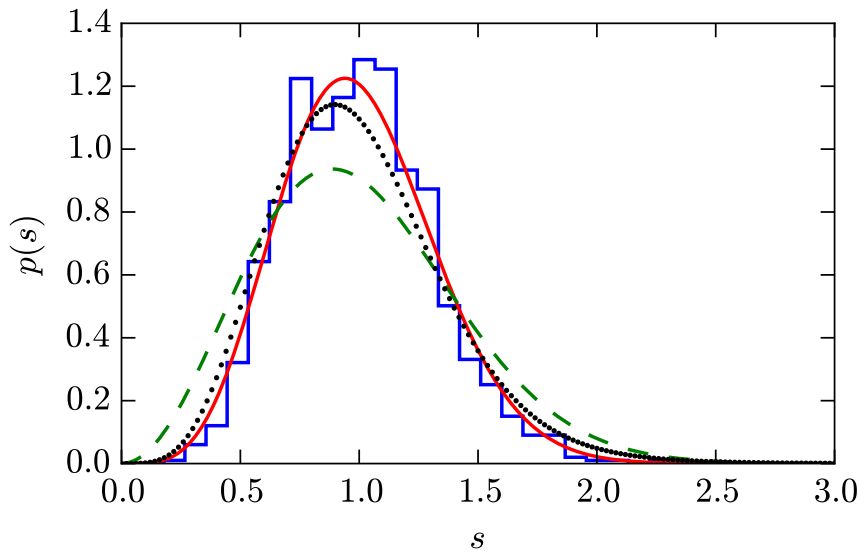
**Fig. 3.17.** The blue solid line is showing the fluctuating part given in Eq. (3.49) of the staircase function  $N(k)$  plotted in Fig. 3.16. The red dashed line

Fig. 3.17 shows the fluctuation of the levels versus the wave number  $k$ . From the overall structure, it is exhibiting an oscillation around zero. This fluctuating part contains information on the underlying classical dynamics of the system [37]. In principle, with this information one can identify associated periodic orbits. However, due to the small number of accessible eigenvalues for one symplectic graph, we shall not proceed in that direction.

### 3.6 Level spacing distribution

In previous section we have demonstrated that our microwave graph shown in Fig. 3.3 has symplectic symmetry which is usually associated with spin-1/2 systems. In this section we will focus on nearest neighbor spacing distribution (NNSD) of those Kramers doublets observed at  $\Delta\varphi = \pi$ .

Fig. 3.18 shows the level spacing distribution  $p(s)$  of symplectic graphs with one pair of connecting bonds, where  $s = s' / \langle s' \rangle$  is the normalized level spacing,  $\langle s' \rangle$  is the mean level spacing which is normalized to one for each single graph and  $s' = \nu_{n+1} - \nu_n$  is the spacing between two nearest resonances, for symplectic case the doublets. This result is obtained by collecting eigenfrequencies associated to Kramers doublets from 9 different graphs and altogether 1130 eigenvalues are used. These different graphs are achieved by: (i) replacing pair(s) of bonds with other bonds of different lengths; (ii) changing the coupling points of the graph to the probing leads. For each of these graphs with a typical optical length of 3.3 m, there are about 130 doublets observed. The green dashed line corresponds to the Wigner GUE distribution as given in Eq. (2.78b) and the red solid line is corresponding to the Wigner GSE distribution which is given in Eq. (2.78c). The experimental result, the histogram, fits well to the Wigner GSE distribution and is clearly at odds with a GUE distribution. The dotted black line is for level spacing distribution obtained from the one pair of connecting bonds approximation given in Eq. (3.41). During the preparation of thesis we have noticed that already Kuemmeth *et al.* [11] observed GSE statistics in the spectra of Au nanoparticles.



**Fig. 3.18.** Spectral nearest neighbor spacing distribution for symplectic graphs with a single pair of connecting bonds obtained by superimposing the results from 9 different spectra (blue). The solid red and dashed green line correspond to GSE and GUE Wigner distributions, respectively, see Eqs. (3.42) and (2.78b). The dotted black line corresponds to the single pair of bonds approximation given in Eq. (3.41).

This result makes the whole spin-1/2 physics [38] accessible to microwave analogue studies.

In Sec. 3.2.4 we have seen that one pair of connecting bonds is not sufficient to couple two subgraphs with identical GUE spectra such that the spectrum of resulting

coupled graph agrees completely with Wigner GSE statistics. Nevertheless, the level spacing distribution shows the quartic level repulsion at small spacings as shown in Fig. 3.4, which is one of the main characteristics of GSE statistics. In order to increase the coupling between the two GUE subspectra we have modified the graph by simply adding another one pair of connecting bonds as shown in the sketch (3.19). One phase shifter sketched as a dashed blue line (and noted by PS1 on the sketch) is placed on the one bond,  $b = (\bar{6}, 4)$ , the second phase shifter PS2 is placed on the bond  $b = (\bar{1}, 3)$ , sketched as a dashed red line. Therefore, one pair includes  $b_{\bar{4}6}, b_{\bar{6}4}$ , while the another pair includes  $b_{\bar{1}3}, b_{3\bar{1}}$ . When the phase shifters at one step, say at the origin, the lengths of cables are chosen such that  $L_{\bar{4}6} = L_{\bar{6}4}$  and  $L_{\bar{1}3} = L_{3\bar{1}}$ . When performing the measurement for the graph with this configurations care must be taken, because the phase difference  $\Delta\varphi$  between the two bonds of each pairs must be exactly the same. After many times of testing, we were successful to achieve this requirements and the resulting phase difference  $\Delta\varphi$  is taken care via the calibration of the length difference  $\Delta l$  on both pairs again by checking the transmission minima as did for the graph with one pair of connecting bonds, Sec. 3.4.1. We used the same approach in the extraction of resonances at  $\Delta\varphi = \pi$ .

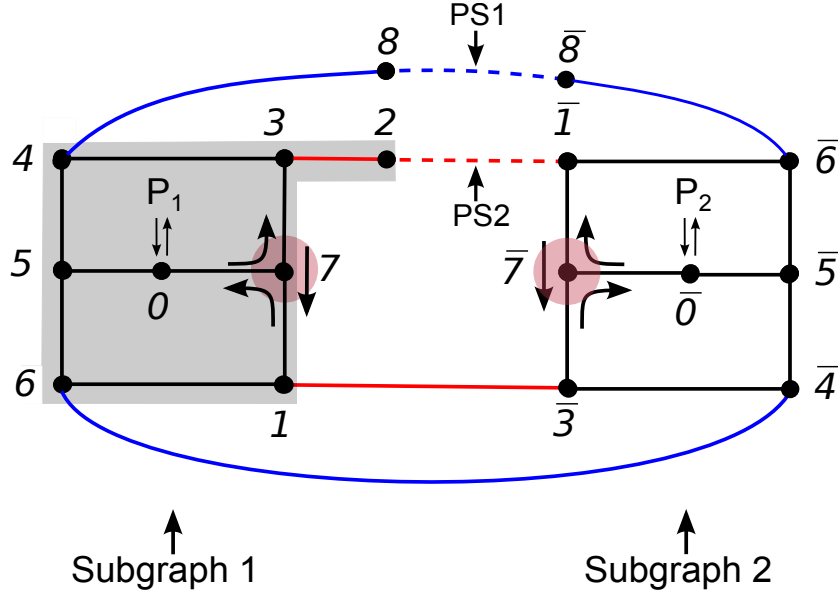


**Fig. 3.19.** The sketch of the GSE graph with two pairs of connecting bonds. Where the dashed red line corresponds to one phase shifter and dashed blue line correspond to another phase shifter. The lengths of bonds are not to scale. The red shaded points at vertex 7 and  $\bar{7}$  correspond to the position of circulators.

Fig. 3.20 shows the level spacing distribution of this graph with two pairs of connecting bonds. We used altogether 777 eigenvalues collected from 5 different graphs which are obtained by changing the lengths of their bonds. The spacings  $s$  between nearest neighboring levels are normalized by the mean level spacing  $\langle s \rangle = 1$  for each graph. The experimental result agrees well with the Wigner GSE distribution given by Eq. (3.42), the green dashed line corresponds to the Wigner GUE distribution given by Eq. (2.78b) and the black dotted line is for the distribution from the one pair of connecting bonds approximation given in Eq. (3.41).

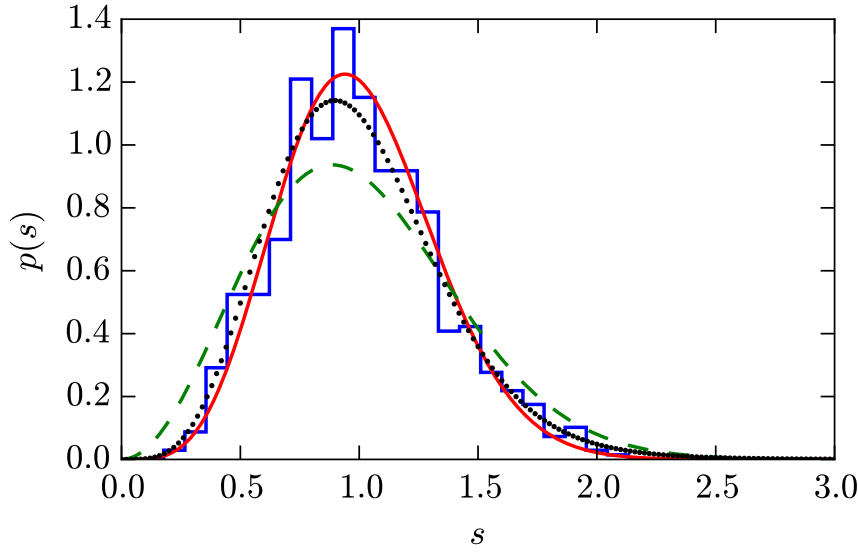


**Fig. 3.20.** Spectral nearest neighbor spacing distribution for symplectic graphs with a two pairs of connecting bonds obtained by superimposing the results from 5 different spectra (blue). The solid red and dashed green line correspond to GSE and GUE Wigner distributions, respectively, see Eqs. (3.42) and (2.78b). The dotted black line corresponds to the single pair of bonds approximation given in Eq. (3.41).

In principle one should expect to see the effect of one extra pair of connecting bonds from the resulting level spacing distribution in comparison with the distribution from one pair of connecting bonds approximation given by in Eq. (3.41). To see the difference one would have to use at least 10 times more eigenvalues. Comparing Figs. 3.18 and 3.20 one notices that the statistical evidence is not sufficient to see the influence of the additional pairs of bonds. from the symplectic graph with one pair of connecting bonds, due to the statistically insufficient experimental data we did not observe significant improvements in our experimental result, the histogram in Fig. 3.20, from the symplectic graph with two pairs of connecting bonds. Therefore, from the practical point of view the Wigner GSE distribution is completely sufficient to describe the experimental data, although in random matrix simulations, the histogram in Fig. 3.4, the difference to the single pair of bonds approximation is clearly distinguishable, where  $10^5$  Kramers doublets from random matrix simulation have been used and the same number of energy levels are used in Ref. [23] to obtain the result shown in Fig. 3.1 for the GSE graph with two pair of connecting bonds as well.

A further increase of number of pairs of connecting bonds would boost the complexity of the experiment and would require considerable extra efforts, but the numerically it is easy to address this problem. Fig. 3.21 shows the random matrix result for the level spacing distribution of gradually increased number of pairs of connecting bonds. The random matrix spectra were generated based on the Hamiltonian given by Eq. (3.31), where the off-diagonal elements are given by Eq. (3.32) for GSE graph with only one pair of connecting bonds. In the random matrix simulation a more general form was used as given in Eq. (3.50),

$$\left[ V\bar{V}^\dagger \right]_{nm} = \sum_{i=1}^b \left[ \psi_{n,2i-1} \psi_{m,2i} + e^{i\Delta\varphi} \psi_{n,2i} \psi_{m,2i-1} \right] \quad (3.50)$$

was used to generate the off-diagonal elements for graphs with more number of connecting bonds, where  $b$  is the number of pairs of bonds in Eq. (3.50) and  $\Delta\varphi = \pi$  for the symplectic case. Sure enough for ten pairs of connecting bonds the level spacing distribution completely converges to Wigner GSE distribution. A more detailed description of this result can be found on the Appendix B of Ref. [13].

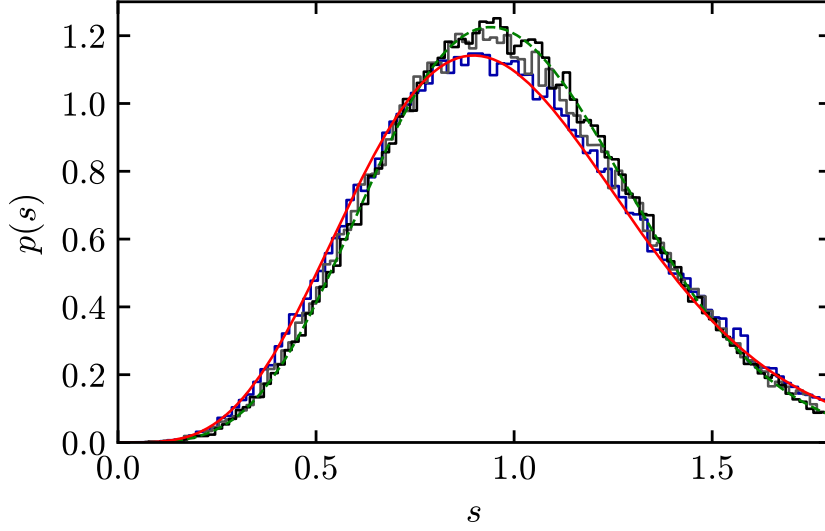


**Fig. 3.21.** The level spacing distribution  $p(s)$  for random matrix simulation for the GSE graph, using the Hamiltonian given in Eq. (3.31) and with off-diagonal blocks given by Eq. (3.50) for  $\Delta\varphi = \pi$  with several different number of pairs of connecting bonds  $b = 1$  (blue),  $b = 2$  (gray) and  $b = 10$  (black). The green dashed line is for Wigner GSE distribution and the red solid line is for the distribution from one pair of bonds approximation given in Eq. (3.41). The size of the GSE subblocks  $H_0$  and  $\tilde{H}_0$  is 500. Each histogram is a result of 2000 realizations.

### 3.7 Spectral correlations

One way to quantitatively distinguish random matrix Gaussian ensembles is the nearest neighbor spacing distribution (NNSD)  $p(s)$  which measures the short range correlation between neighboring energy levels. Random matrix theory has provided several other quantities to discriminate Gaussian ensemble in terms of long range spectral correlations. In this section we will present our experimental results from the symplectic spectra in this regards.

#### 3.7.1 Spectral two-point correlation function $R_2(L)$

The spectral two-point correlation function is the probability density to find two different eigenenergies with distance  $L = E_n - E_m$ ,

$$R_2(L) = \frac{1}{N} \sum'_{n,m} \delta(L - E_n + E_m) \quad (3.51)$$

where  $L$  is given in unit of the mean level spacings. The two-point correlation function  $R_2(L)$  shows oscillation for  $L > 1$  for all three random matrix Gaussian ensembles. This oscillation is actually originated from the level repulsion. For the Gaussian symplectic ensemble (GSE), this oscillation is much stronger than for the other two ensembles thanks to the strong quartic level repulsion.

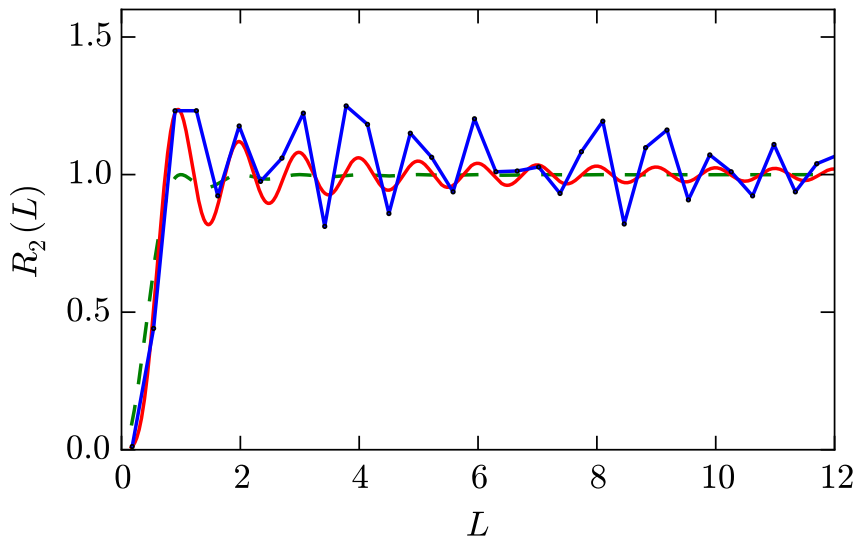


**Fig. 3.22.** Experimental two-point correlation function  $R_2(L)$ , together with the random matrix prediction for the GSE (solid red) and the GUE (dashed green), respectively.

The experimental result for  $R_2(L)$  from the GSE graph is presented in Fig. 3.22 together with the theoretical  $R_2(L)$  for GSE and GUE systems. The same data set used for Fig. 3.18 is used. The random matrix ensemble-averaged theoretical  $R_2(L)$  for all three Gaussian ensembles are given in Ref. [2], and is given for GUE system by

$$R_2(L) = 1 - \left( \frac{\sin(\pi L)}{\pi L} \right)^2, \quad (3.52)$$

and for the GSE system by

$$R_2(L) = 1 - \left( \frac{\sin(2\pi L)}{2\pi L} \right)^2 + \frac{d}{dL} \left( \frac{\sin(2\pi L)}{2\pi L} \right) \int_0^L \left( \frac{\sin(2\pi t)}{2\pi t} \right) dt. \quad (3.53)$$

The behavior for small  $L \rightarrow 0$  is

$$R_2(L) \sim \begin{cases} L^2 & , \quad (GUE) \\ L^4 & , \quad (GSE) \end{cases} \quad (3.54)$$

The experiment agrees very well with theoretical  $R_2(L)$  for GSE system such that the expected strong oscillation with peaks at integer  $L$  for GSE from the theory is reproduced by the experiment. The experimental  $R_2(L)$  for overall  $L$  follows rather GSE than GUE. Moreover, the oscillation with increasing  $L$  is stronger than the theoretical expectation by Eq. (3.53). This is suggesting that the level correlation is stronger than the random matrix theoretical prediction. Indeed the behavior of the experimental spectral rigidity  $\Delta_3(L)$  for  $L \leq 12$  is in favor of this suggestion, see Sec. 3.7.3.

### 3.7.2 Spectral form factor $K(\tau)$

The most conspicuous quantity to distinguish Gaussian ensembles is the spectral form factor  $K(\tau)$ , which is defined as the Fourier transform of the spectral two-point correlation function,

$$K(\tau) = \frac{1}{N} \sum'_{n,m} e^{2\pi i \tau (E_n - E_m)}. \quad (3.55)$$

where  $\tau = t/T_H$  is the normalized time with  $T_H = 2\pi \hbar \bar{\rho}$  being the Heisenberg-time and  $\bar{\rho}$  the mean level density. For the GUE the ensemble averaged form factor is given by

$$K(\tau) = \begin{cases} \tau & , \quad \tau \leq 1 \\ 1 & , \quad \tau > 1 \end{cases} \quad (3.56)$$

For the GSE the ensemble averaged form factor is given by

$$K(\tau) = \begin{cases} \frac{1}{2}|\tau| - \frac{1}{4}|\tau| \ln |1 - |\tau|| & , \quad \tau \leq 2 \\ 1 & , \quad \tau > 2 \end{cases} \quad (3.57)$$

The logarithmic singularity at  $\tau = 1$  described by Eq. (3.57) is an unmistakable signature of the GSE system, while for other Gaussian ensembles the form factor  $K(\tau)$  is continuous for all values of  $\tau$ . Fig. 3.23 is showing the experimental result for  $K(\tau)$  together with theoretical predictions for GSE and GUE systems. The experimental result agrees well with theoretical prediction given by Eq. (3.57) including the singularity at  $\tau = 1$  expected by theory for GSE system, which is nicely reproduced in the experiment. In the experimental result we did not remove the diagonal term of the double sum in Eq. (3.55), which in turn results in a delta peak at  $\tau = 0$ .



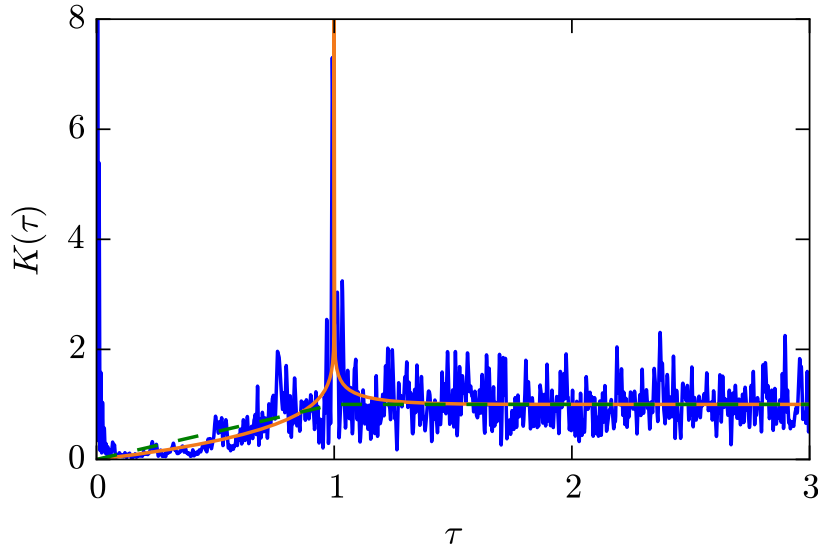


**Fig. 3.23.** The spectral form factor  $K(\tau)$ . The blue solid line is for the experimental result and the random matrix theoretical spectral form factor (or Dyson-Mehta statistics)  $K(\tau)$  for GSE (orange solid), GUE (green dashed). The peak at  $\tau = 0$  from the double sum in Eq. (3.55) was not removed from the experimental result.

### 3.7.3 Number variance $\Sigma^2(L)$ and spectral rigidity $\Delta_3(L)$

In many experiments the available data are not sufficient to exhibit expected features of the system via the spectral two-point correlation function  $R_2(L)$  and spectral form factor  $K(\tau)$ . But smoothed quantities such as the number variance  $\Sigma^2(L)$  and spectral rigidity  $\Delta_3(L)$  may still reveal the statistical properties of the system. Following Ref. [8] the number variance  $\Sigma^2(L)$  is defined as the variance of the number  $n(E, L)$  of eigenvalues in an interval of length  $L$ , centered at the energy  $E$ ,

$$\Sigma^2(L) = \langle (n(E, L) - \langle n(E, L) \rangle)^2 \rangle \quad (3.58)$$

where  $n(E, L) = \int_{E-L/2}^{E+L/2} \rho(E) dE$  and its ensemble average  $\langle n(E, L) \rangle = L$  is independent of  $E$ . By assuming the mean level density normalized to one, Eq. (3.58) may be written as

$$\Sigma^2(L) = L - 2 \int_0^L (L - E)(1 - R_2(E)) dE \quad (3.59)$$

We can see that  $\Sigma^2(L)$  is somehow a smoothed version of the two-point correlation function  $R_2(E)$ . The experimental result for  $\Sigma^2(L)$  is plotted in Fig. 3.24. An overall good agreement between the experimental result and random matrix prediction for GSE is found for  $L \leq 2$ , for larger values of  $L$  there are clear deviations which can be understood as the effect of missing levels.

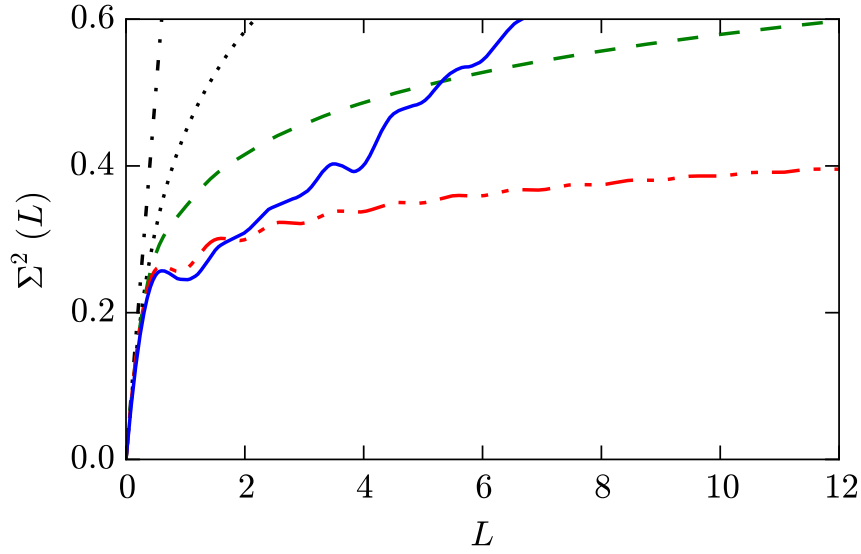


**Fig. 3.24.** The spectral number variance  $\Sigma^2(L)$ . The blue solid line is for the experimental result and the theoretical number variance  $\Delta_3$  for GSE (red dashed), GUE (green dashed), GOE (black dotted) and Poisson (dashed-dotted).

The next quantity to check is the spectral rigidity  $\Delta_3(L)$  introduced by Dyson and Mehta [2, 39], which is also based on the two-level correlation function and more frequently used than the number variance  $\Sigma^2(L)$ . The spectral rigidity is defined as the ensemble average of the minimum of the  $\chi^2$  function obtained in the fit,

$$\Delta_3(L) = \left\langle \min_{a,b} \int_{E-L/2}^{E+L/2} [n(E) - (bE + a)]^2 dE \right\rangle, \quad (3.60)$$

where  $n(E)$  is the integrated density of states. It is actually the staircase function in Eq. (3.47) with mean slope of one, indeed the slope found from fitting in Fig. 3.16 is 1.0210 very close to one.  $a$  and  $b$  are the intercept and slope of the fitted line, respectively. We can see that the spectral rigidity does not depend on the energy level itself, but does on the all possible distances  $L$  of these levels. Alternatively,  $\Delta_3(L)$  can be expressed in terms of the number variance  $\Sigma^2(L)$  as

$$\Delta_3(L) = \frac{2}{L^4} \int_0^L (L^3 - 2L^2E + E^3) \Sigma^2(E) dE. \quad (3.61)$$

Fig. 3.25 shows the experimental result and random matrix theoretical prediction for spectral rigidity  $\Delta_3(L)$ . The experimental result, the blue solid line, agrees with the random matrix prediction, the red dashed line, for  $L \leq 2$  and for larger values of  $L$  up to  $L = 12$  the experimental spectral rigidity is below the random matrix prediction, this is again due to the missing levels. The effect of missing level on the statistical properties of a spectrum can be found in more details in Ref. [40, 41].

$\Delta_3(L)$  measures the degree of rigidity of the spectrum in such a way that for a given range  $L$ , the smaller  $\Delta_3(L)$  is, the stronger is the rigidity, signifying the long range correlations between levels [39]. Therefore, the spectrum of our GSE graph at  $\Delta\varphi = \pi$  is even more rigid and the levels are much stronger correlated than predicted degree expected by random matrix theory, at least for  $L \leq 12$ .

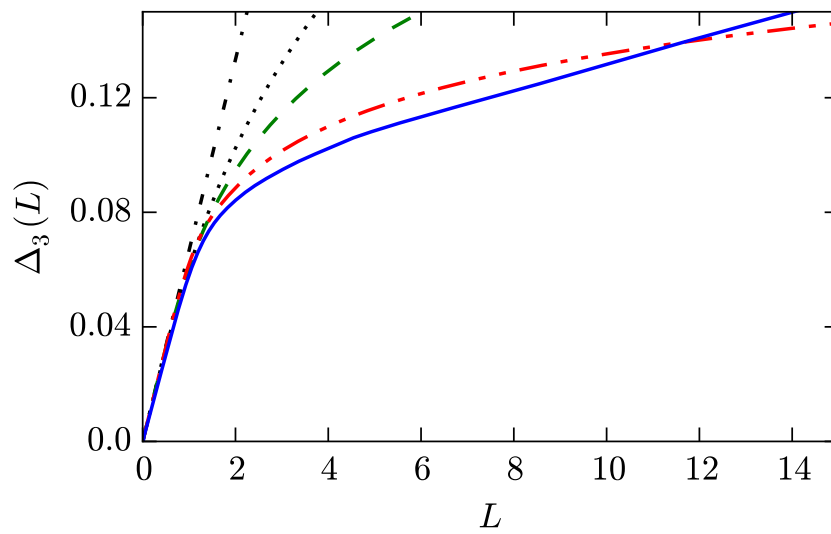


**Fig. 3.25.** The spectral rigidity  $\Delta_3(L)$ . The blue solid line is for the experimental result and the theoretical spectral rigidity (or Dyson-Mehta statistics)  $\Delta_3$  for GSE (red dashed), GUE (green dashed), GOE (black dotted) and Poisson (dashed-dotted).

### 3.8 Dynamical transition from GSE via GUE to GOE

Although our experiment was designed with the motivation to realize GSE statistics, the measured spectra shown in Fig. 3.12 do not only allow to analyze the spectrum at  $\Delta\varphi = \pi$  where the GSE statistics is observed as expected, but also provide a broad range of spectra for all values of  $\Delta\varphi$  from 0 to  $2\pi$  and even up to  $3\pi$  at higher frequencies. We take advantage of this particular feature of the experimental spectra of our GSE microwave graph to study the spectral level dynamics depending on  $\Delta\varphi$ . In all previous sections we have mainly studied the spectrum at  $\Delta\varphi = \pi$  in details.  $\Delta\varphi = \pi$  corresponds to the minus sign in Eq. (3.16) (middle) and the corresponding spectrum of the graph has antiunitary symmetry of  $\mathcal{T}$ , squaring to minus one,  $\mathcal{T}^2 = -1$  and the statistics of the observed Kramers doublets showed Wigner GSE type. For the case of  $\Delta\varphi = 0$  or  $\Delta\varphi = 2\pi$  that minus sign in Eq. (3.16) (middle) is missing and the resulted spectrum has still the antiunitary symmetry  $\mathcal{T}$ , but now obeying  $\mathcal{T}^2 = +1$ , the corresponding statistics of the eigenvalues is expected to follow Wigner GOE statistics. At all other values of  $\Delta\varphi$  in between 0 and  $\pi$ , set  $\Delta\varphi = 3\pi/2$  or  $\pi$  and  $2\pi$  the corresponding spectra do not have an antiunitary symmetry, in other words, the antiunitary symmetry is broken, thus Wigner GUE statistics is expected (regarding in this respect see Sec. 2.5 of Ref. [4]).

Apart from changing symmetry for different values of  $\Delta\varphi$ , the whole spectra have another interesting feature to be discussed. As the unique property of our setup the phase difference  $\Delta\varphi$  can be changed by changing the length difference  $\Delta l$  introduced by two phase shifters, this results in a change of the mean level density  $\Delta\rho_{\text{Weyl}} = \Delta l / \pi = \Delta\varphi / (\pi k)$ , where  $k$  is the microwave wave number. Varying  $\Delta\varphi$  from 0 to  $2\pi$  results in a change of  $2/k$  of the mean level density  $\rho_{\text{Weyl}}$ . If  $\Delta\varphi$  changes by  $2\pi$ , the mean integrated density of states  $N_{\text{Weyl}}(k) = k \rho_{\text{Weyl}}$  by a factor of 2. From the Figs. 3.13 and 3.16 we see that this is also true for the exact integrated density of states, the staircase function  $N(k)$ , thanks to the periodicity of the spectra. Following any resonance from  $\Delta\varphi = 0$  to  $\Delta\varphi = 2\pi$  it arrives two resonances to the right at the crossing of the  $2\pi$  line. Wrapping the spectra onto a cylinder by identifying the line  $\Delta\varphi = 0$  with the line  $\Delta\varphi = 2\pi$  the spectra may hence be interpreted in terms of just one pair of resonances twisted spiral-like along the cylinder surface. The two members of the pair merge whenever they cross the  $\pi$  line and typically have a maximal spacing when crossing the  $2\pi$  line.

In order to check the symmetries expected for spectra associated with different values of the phase difference  $\Delta\varphi$ , we shall focus our analysis on the spectra at  $\Delta\varphi = \pi$ ,  $\Delta\varphi = 3\pi/2$  and  $\Delta\varphi = 2\pi$  where GSE, GUE, GOE statistics are expected, respectively. The spectrum at  $\Delta\varphi = \pi$  has already been considered in details. However, the approach explained in Sec. 3.4.2 is used to extract the resonances of the spectrum at  $\Delta\varphi = \pi$  no longer works efficiently for the spectra at  $\Delta\varphi = 3\pi/2$  and  $\Delta\varphi = 2\pi$ . In principle, fitting the spectrum to complex Lorentzian should work but it would be quite exhausting for altogether 14 graphs with around 250 and around 220 eigenvalues at  $\Delta\varphi = 3\pi/2$  and  $\Delta\varphi = 2\pi$ , respectively. Therefore, to identify resonances we looked at the minima of each corresponding spectrum. The well known drawback of this method is that it is quite difficult even confusing to decide the correct resonance frequency when it comes to the overlapping resonances. For one or the other reason few percent of our doublets were not split well at  $\Delta\varphi = 2\pi$  particularly at  $\Delta\varphi = 3\pi/2$  where the reminiscences of symplectic symmetry are still considerable, this can also be seen from Fig. 3.13. We admit that the quality of the extracted data could be further improved.

Fig. 3.26 is showing the results. The plots at left column, from top to bottom,

are the nearest neighbor spacing distributions  $p(s)$  of the spectra for  $\Delta\varphi = \pi$ ,  $\Delta\varphi = 3\pi/2$  and  $\Delta\varphi = 2\pi$ , respectively. In order to make the discussion coherent, we have used individual 2 levels of each Kramers doublet instead of using corresponding Kramers doublet as one single level, this gives an additional peak to the level spacing distribution at  $s = 0$  corresponding to the zero distance between the two member levels of each doublet. When we do so we have to ensure that the mean level spacing is  $\langle s \rangle = 1$ , this moves the distribution of Kramers doublets to the right by factor of two. So the experimental data is collected from all 14 different graphs with one pair of connecting bonds and two pairs of connecting bonds.

The experimental level spacing distributions of the spectra at  $\Delta\varphi = \pi$  and  $\Delta\varphi = 2\pi$  agreed well with Wigner GSE and Wigner GOE distributions, respectively. For the level spacing distribution of the spectrum at  $\Delta\varphi = 3\pi/2$  a deviation from the Wigner GUE distribution is found. Since all the three classical Gaussian random matrix ensembles, namely GOE, GUE and GSE, with corresponding indices  $\beta = 1$ ,  $\beta = 2$  and  $\beta = 4$ , can be discriminated by means of the order of level repulsion at small distances of neighboring levels by comparing their level spacing distributions  $p_\beta(s)$ . One expects for  $s \rightarrow 0$  linear level repulsion  $p_1(s) \sim s$  for GOE system, quadratic level repulsion  $p_2(s) \sim s^2$  for GUE system and quartic level repulsion  $p_4(s) \sim s^4$  for GSE system. To see the small distance behavior of level spacing distribution  $p(s)$  we have used integrated level spacing distribution

$$I(s) = \int_0^s p(\bar{s}) d\bar{s}, \quad (3.62)$$

The analytic expression for  $\beta = 1$  is

$$I_1(s) = 1 - e^{-\frac{\pi}{4}s^2} \quad (3.63)$$

for  $\beta = 2$  The analytic expression for  $\beta = 1$  is

$$I_2(s) = \text{erf}(\sqrt{a}s) - a s e^{-a s^2} \quad (3.64)$$

where  $a = \frac{4}{\pi}$ . For  $\beta = 4$

$$I_4(s) = \frac{3\sqrt{\pi}c}{8a^{3/2}} \text{erf}(\sqrt{a}s) - \frac{cs^3}{2} e^{-a s^2} - \frac{3cs}{4a} e^{-a s^2} \quad (3.65)$$

where  $a = \frac{64}{9\pi}$  and  $c = \frac{2^{12}}{3^4\pi^2}$  and  $\text{erf}(x)$  in Eqs. (3.64), (3.65) is the error function. Due to the integration given by Eq. (3.62), the expected level repulsion exponent will be increased by one as  $I_\beta(s) \sim s^{\beta+1}$  for small distances  $s \sim 0$ .

Both the experimental and theoretical results are presented on the right column of Fig. 3.26. To make the repulsion exponents clearly visible, we plotted  $I_\beta(s)$  versus  $s$  in double logarithmic scale. The plots d) and f) correspond to  $\Delta\varphi = \pi$  and  $\Delta\varphi = 2\pi$  showing a good agreement over nearly two orders of magnitudes of the integrated level spacing distribution  $I_\beta(s)$  for the cases of  $\beta = 4$  and  $\beta = 1$ , respectively. The antiunitary symmetry  $\mathcal{T}$  with  $\mathcal{T}^2 = -1$  or  $\mathcal{T}^2 = +1$  thus really maps onto a spectral repulsion  $p(s) \sim s^\beta$  with  $\beta = 4$  and 1, respectively. For the case of  $\Delta\varphi = 3\pi/2$ , the experimental result is clearly at odds with the integrated Wigner GUE level spacing distribution, but still it shows the expected repulsion exponent for  $\beta = 2$  (the dotted black line in plot e)).

At the beginning of this section we have argued that the antiunitary symmetry  $\mathcal{T}$  with  $\mathcal{T}^2 = -1$  at  $\Delta\varphi = \pi$  will be broken for all values of  $\Delta\varphi$  departing from  $\pi$  to  $2\pi$ ,

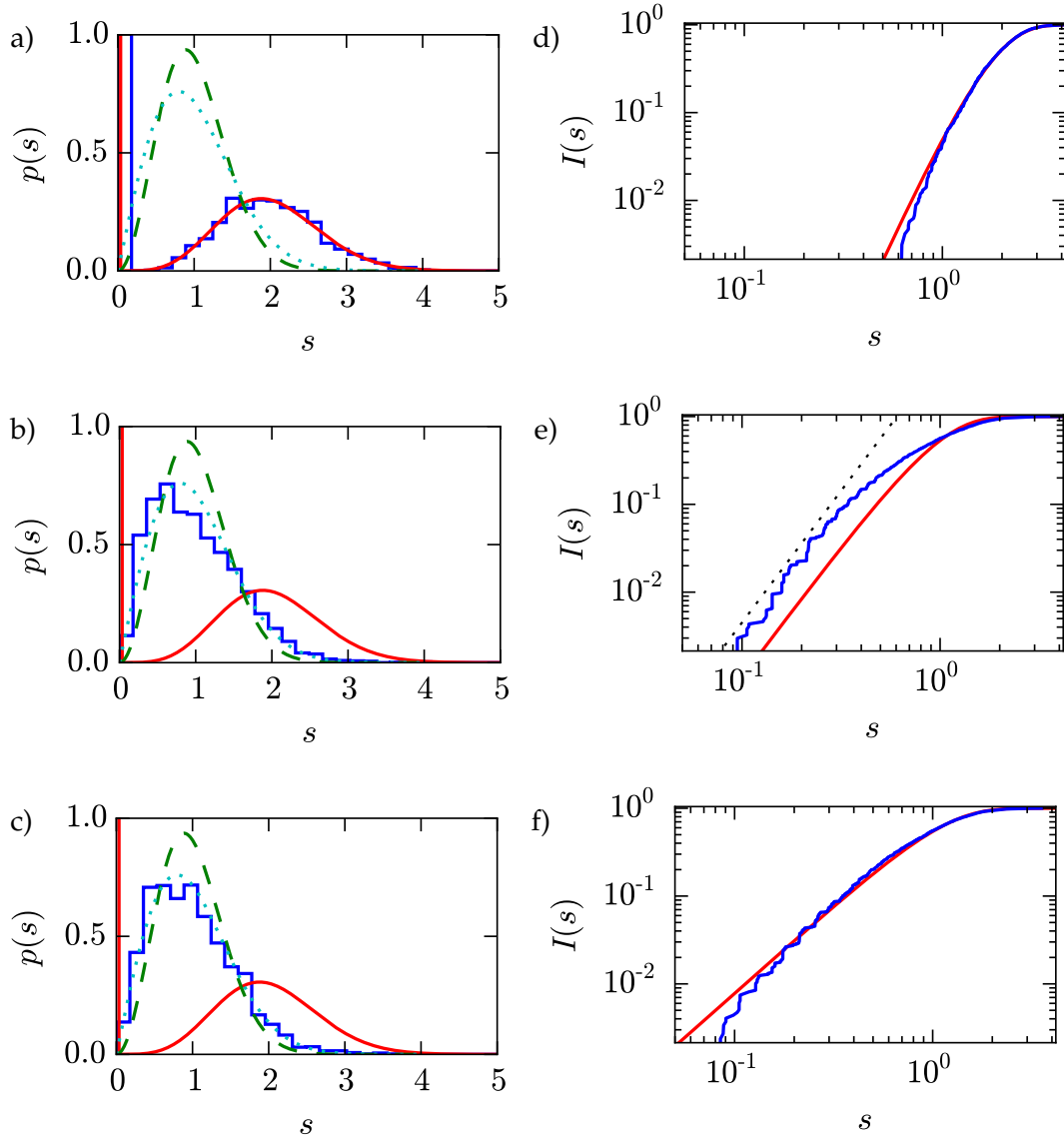


**Fig. 3.26.** Level-spacing distributions [left, a) - c)] and corresponding integrated level-spacing distributions [right, d) - f)] for  $\Delta\varphi=\pi$ ,  $\Delta\varphi=1.5\pi$  and  $\Delta\varphi=2\pi$  (from left to right). The green dashed, cyan dotted, and red solid lines correspond to the Wigner GOE, GUE, and GSE distributions, respectively. For the integrated spacings only the respective distribution is plotted as solid line. The dotted line in e) indicates a slope of 3.

but the experimental result showed in plot b) is indicating that this is not perfectly true for spectra we analyzed. The level dynamics depending on  $\Delta\varphi$  is not sufficient to completely destroy the correlation between the two member of the Kramers doublets. As it seems, when  $\Delta\varphi$  departs from  $\Delta\varphi = \pi$  line, the degeneracy is lifted and Kramers doublets start to split, but the correlation between the previous two members of each doublet maintains up to considerable value of  $\Delta\varphi$ . The level spacing distribution  $p(s)$  for the small spacing like  $s < 0.5$  is exceeding to the left from the expected GUE curve in plot b) of Fig. 3.26. This feature can be understand as an indication of the remaining correlation of members of each doublet. Similar behavior is also observed in random matrix simulation from the level spacing distribution of a spectrum for a GSE graph with one pair of connecting bonds and two pairs of connecting bonds, shown in Fig. 3.27. For ten pairs of connecting bonds, the level spacing distribution agrees completely to Wigner GUE distribution (See Appendix B of Ref. [13] to more details of the simulation).

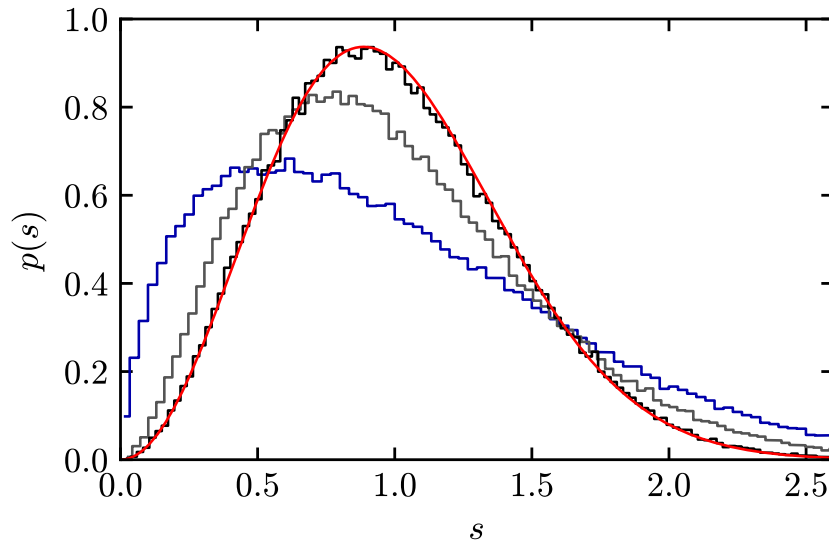


**Fig. 3.27.** The level spacing distribution  $p(s)$  for random matrix simulation for the GUE graph, using the Hamiltonian in Eq. (3.31) and with off-diagonal blocks in Eq. (3.50) for  $\Delta\varphi = 3\pi/2$  with several different number of pairs of connecting bonds  $b = 1$  (blue),  $b = 2$  (gray) and  $b = 10$  (black). The solid red curve is for Wigner GUE distribution. The size of the GUE subblocks  $H_0$  and  $\tilde{H}_0$  is 500. Each histogram is a result of 2000 realizations.





# Scattering experiments on graphs with orthogonal, unitary and symplectic symmetry

## 4.1 Motivation

During the last decade transport properties and scattering of waves within different systems have been studied both theoretically and experimentally. The area of mesoscopic quantum systems has been one of the popular playground in this regard. The Landauer-Büttiker formalism provides a unique way which allows one to study the electrical conductance of a medium by looking at relevant scattering properties of the system of interest. Based on this approach the classical analogies of quantum systems have been used as auxiliary tools for a better understanding of the conductance properties of an electrical devices in two-terminal configurations. There are an abundant number of scattering experiments for systems with time reversal symmetry (TRS) and there are few number of scattering experiments on systems without time reversal symmetry. To our knowledge, including our result discussed in previous Chap. 3 there are only two experimental studies are available for systems with time reversal symmetry and spin-1/2 interaction [11, 13, 33].

When it comes to the measurement of the conducting features of devices, multi-terminal probing technique are quite popular [42, 43]. Alternatively to the mostly used two-terminal configuration, three terminal systems provide information of non-local effects associated with transport observables. There is a comprehensive theoretical understanding of quantum graph [24, 27], and there are also a number of microwave experiments on the subject [12, 13, 32, 33].

In this chapter I will present our results of a currently undergoing joint project with Dr. A. M. Martínez-Argüello from Mexico. I will start with the presentation of a scheme for a three terminal quantum device to study coherent transport and a theoretical prediction for the distribution of a three-terminal-transport related quantity. The distribution function of this quantity is universal and depends only on the time reversal invariant properties of the system. On the basis of the equivalence relation between electrical conductance and transmission coefficients we employed three different three-terminal quantum graphs with time reversal symmetry without spin-1/2, without time reversal symmetry and with time reversal symmetry including spin-1/2 interaction to check the theoretically predicted behavior. At the end we will discuss corresponding experimental results including the effect of imperfect coupling and absorption.

## 4.2 Theory

For a multi-terminal electrical device, the electrical current  $I_i$  on terminal  $i$  can be written as

$$I_i = \sum_j G_{ij}(V_i - V_j), \quad \text{with} \quad G_{ij} = G_0 T_{ij}, \quad (4.1)$$

where  $V_i$  is the voltage at terminal  $i$ ,  $G_{ij}$  is the conductance from terminal  $j$  to terminal  $i$ ,  $T_{ij}$  is the corresponding transmission coefficient from terminal  $j$  to terminal  $i$ ,  $G_0 = \frac{e^2}{h}$  is the elementary conductance quantum, if the spin degeneracy is included, the quantum of conductance is  $G_0 = \frac{2e^2}{h}$ . Let restrict ourselves to a device with only three terminals  $T_1, T_2, T_3$  as shown in Fig. 4.1 and set one of these terminals, lets say terminal  $T_3$ , as a probe such that there is no current flowing through this terminal, i.e.  $I_3 = 0$ .

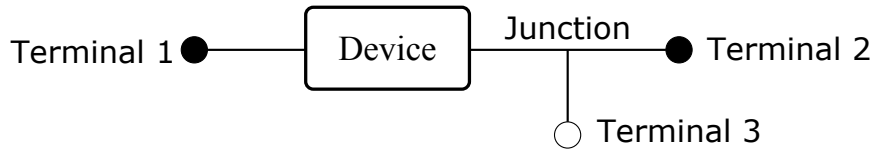


**Fig. 4.1.** Sketch of a three-terminal setting that allows the measurement of the voltage along a device. The device carries a current while the vertical wire measures the voltage drop. Thin lines represent perfect conductors connected to sources of voltages  $V_1, V_2$ , and  $V_3$ .

The voltage at terminal 3, is a weighted average of the voltages in the other terminals, the weight may be determined by the conductance coefficients from the other terminals to the probe, means the  $T_3$ . Thus, one can write  $V_3$  as

$$V_3 = \frac{1}{2} (V_1 + V_2) + \frac{1}{2} (V_1 - V_2) f, \quad (4.2)$$

where

$$f = \frac{T_{31} - T_{32}}{T_{31} + T_{32}}, \quad (4.3)$$

Equation. (4.2) shows that the voltage at terminal  $T_3$  is fluctuating about the average of  $V_1$  and  $V_2$ . The value  $f$  can be varied from  $-1$  to  $+1$  and only depends on the transmissions from  $T_1$  to  $T_3$  and  $T_2$  to  $T_3$ . Godoy *et al.* [44, 45] have studied the voltage drop along a disordered quantum wire by utilizing this three-terminal method.

As shown in Fig. 4.1 our proposed setup to experimentally study this quantity  $f$  consists of two main building blocks: one is a quantum graph with orthogonal, unitary and symplectic symmetry; the other one is a microwave T-junction. This three terminal device is realized by connecting one of the tree arms of the T-junction to one vertex of a quantum graph. The graphs we are going to use have chaotic dynamics characterized by the orthogonal, unitary and symplectic symmetry with corresponding labels  $\beta = 1, \beta = 2$  and  $\beta = 4$ , respectively. In order to study the fluctuation of  $f$  we shall use the scattering approach of random matrix theory. The graphs used in the experiments have two channels, thus its corresponding scattering matrix may be written as

$$S_g = \begin{pmatrix} r_g & t'_g \\ t_g & r'_g \end{pmatrix}, \quad (4.4)$$

where  $r_g$  ( $r'_g$ ) and  $t_g$  ( $t'_g$ ) are the reflection and transmission amplitudes, for incidence from the left (right). Since the second building block of our three-terminal device, T-Junction, has three electrically equivalent arms, one can describe it with the following  $3 \times 3$  scattering matrix

$$S_0 = \frac{1}{3} \begin{pmatrix} -1 & 2 & 2 \\ 2 & -1 & 2 \\ 2 & 2 & -1 \end{pmatrix}. \quad (4.5)$$

The intrinsic nature of our experimental three-terminal setup yields  $3 \times 3$  scattering matrix  $S$  for our whole setup showed in Fig. 4.1. Standard scattering theory relates the  $S$  of whole device and  $S_g$ ,  $S_0$  of its building blocks in following way

$$S = S_{PP} + S_{PQ}S_0 \frac{1}{\mathbb{1}_3 - S_{QQ}S_0} S_{QP}, \quad (4.6)$$

where  $\mathbb{1}_3$  is the  $3 \times 3$  unit matrix,  $S_0$  is the scattering matrix of the T-Junction and

$$S_{PP} = \begin{pmatrix} r_g & 0 & 0 \\ 0 & 0 & 0 \\ 0 & 0 & 0 \end{pmatrix}, \quad S_{PQ} = \begin{pmatrix} t'_g & 0 & 0 \\ 0 & 1 & 0 \\ 0 & 0 & 1 \end{pmatrix}, \quad (4.7)$$

$$S_{QP} = \begin{pmatrix} t_g & 0 & 0 \\ 0 & 1 & 0 \\ 0 & 0 & 1 \end{pmatrix}, \quad S_{QQ} = \begin{pmatrix} r'_g & 0 & 0 \\ 0 & 0 & 0 \\ 0 & 0 & 0 \end{pmatrix}. \quad (4.8)$$

where  $r_g$ ,  $t'_g$ ,  $t_g$ ,  $r'_g$  are the elements of the graph scattering matrix  $S_g$  (see Eq. (4.4)). The expression of  $S$  given in Eq. (4.6) has very intuitive meaning: the first term  $S_{PP}$  on the right hand side corresponds to the reflections at the terminals; the second term takes care of all complex multiple scattering processes within the three-terminal device, where  $S_{QP}$  represents the transmission from outside of the device to its whole inside region,  $(\mathbb{1}_3 - S_{QQ}S_0)^{-1}$  contains the multiple reflections between the junction and the graph and  $S_{PQ}$  is representing the transmitted portion from the inside of the device to outside, means through the terminals.

The transmission coefficient is given as  $T_{ij} = |S_{ij}|^2$ , where  $S_{ij}$  are the scattering elements of  $S$  of the whole three-terminal system and takes values according to the system symmetry

$$S_{ij} = \begin{cases} \text{Real,} & \text{TRS, no spin-1/2} & \beta = 1 \\ \text{Complex,} & \text{no TRS} & \beta = 2 \\ \text{Real quaternion,} & \text{TRS + spin-1/2} & \beta = 4 \end{cases} \quad (4.9)$$

where TRS stands for time reversal symmetry. Now our main quantity  $f$  can be rewritten in terms of the elements of  $S$  as

$$f = \frac{|S_{31}|^2 - |S_{32}|^2}{|S_{31}|^2 + |S_{32}|^2} \quad (4.10)$$

Let's assume there is no energy loss within the graph such that the corresponding scattering matrix  $S_g$  is unitary

$$S_g S_g^\dagger = 1. \quad (4.11)$$

Depending on the symmetry of the graph,  $S_g$  belongs to one of the Circular Ensembles: Orthogonal (COE) for  $\beta = 1$ , Unitary (CUE) for  $\beta = 2$ , and Symplectic (CSE)

for  $\beta = 4$ . Thus, one can parametrize the scattering matrix  $S_g$  as

$$S_g = \begin{bmatrix} -\sqrt{1-\tau} e^{2i\phi'} & a^{-1} \sqrt{\tau} e^{i(\phi+\phi')} \\ a \sqrt{\tau} e^{i(\phi+\phi')} & \sqrt{1-\tau} e^{2i\phi} \end{bmatrix}, \quad (4.12)$$

where  $0 \leq \tau \leq 1$ ,  $0 \leq \phi, \phi' \leq \pi$ , and  $a$  is a real, complex, or real quaternion number of modulus 1 for  $\beta = 1, 2$  or 4, respectively. Now the scattering matrix  $S$  given in Eq. (4.6) can be parametrized and the expression for  $f$  in Eq. (4.10) can also be written in terms of parameters as

$$f = \frac{\tau - |1 + \sqrt{1-\tau} e^{2i\phi}|^2}{\tau + |1 + \sqrt{1-\tau} e^{2i\phi}|^2}, \quad (4.13)$$

where the parameter  $a$  disappears. Following Ref. [46] the probability density of  $S_g$  can be written as

$$dP_\beta(S_g) = \frac{\beta}{2} \tau^{-1+\beta/2} d\tau \frac{d\phi}{\pi} \frac{d\phi'}{\pi} da. \quad (4.14)$$

By using this Eq. (4.14) and integrating over all parameters, one gets the probability distribution of  $f$  as

$$p_\beta(f) = \frac{(\beta-1)!!}{\beta [\Gamma(\beta/2)]^2} \frac{(1-f)^{\beta/2}}{(1+f)^{1-\beta/2}}. \quad (4.15)$$

This distribution of  $f$  dominates for negative values of  $f$  and can be understood intuitively from the unique configuration of the device such that the terminal  $T_2$  is much closer to the terminal  $T_3$  than to the terminal  $T_1$ , resulting in a higher probability of transmission from terminal  $T_2$  to terminal  $T_3$  rather than terminal  $T_1$  to terminal  $T_3$ . The width of the distribution is a signature of the nonlocal effects in measurement of the probe port.

Equation. (4.15) is our main theoretical result which is valid in an ideal situation: It applies to quantum systems in the absence of any inelastic process and to classical wave systems in the absence of dissipation and imperfect coupling to the device.

### 4.3 Experimental setup

Fig. 4.2 shows the experimental setups and corresponding sketches of the three-terminal device. The main components of the setup were explained in the previous Chap. 3. Figure a) is the sketch of GOE graph and b) is the corresponding microwave graph. Figure c) and d) are for the case of GUE graph which is realized simply by replacing one of the T-junctions on the graph shown in figure b) by a microwave circulator which breaks the time reversal symmetry. Figure e) is the sketch of the three-terminal setup for the case of symplectic symmetry.

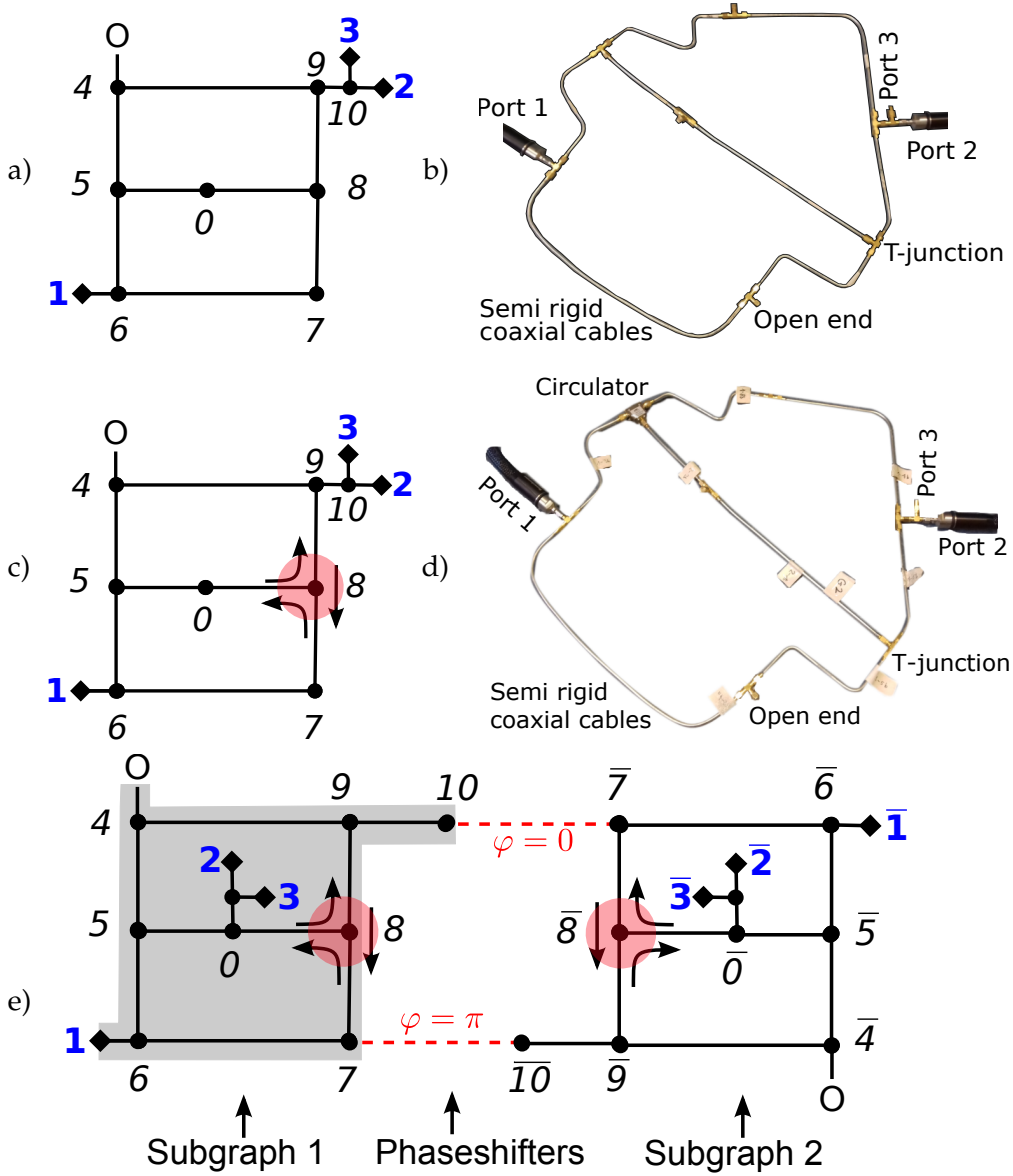


**Fig. 4.2.** Experimental setup and corresponding sketch of three-terminal device shown in Fig. 4.1. a) and b) are for the graph with time reversal symmetry (GOE); c), d) are for the graph without time reversal symmetry (GUE), the circulator breaks the time reversal symmetry; e) is the sketch for the graph with time reversal symmetry and spin-1/2 interaction and its corresponding graph without the third terminal is given in Fig. 3.3 (c). The red shaded region correspond to the circulator in figure c) and figure e).

In order to understand how the symplectic symmetry is realized with this setup, one can see the details in previous Chap. 3 and Ref. [13, 33]. One can see that the third terminal  $T_3$  is, as explained in the previous section, realized by connecting one T-junction to one of the vertex of microwave graph with orthogonal, unitary and symplectic symmetries. The complex scattering matrix elements were measured via an Agilent 8720ES vector network analyzer (VNA). Since our analyzer has only two ports, when we performed the measurement a standard  $50\ \Omega$  terminator is connected to one of the three terminals while the other two being used to take measurements.

Before we start to take series of measurements we have checked if the graph represented by sketch e) in Fig. 4.2 still maintains the required symplectic symmetry after adding the third terminal. To do that we have checked the unitary property by looking at one arbitrary element, lets say  $S_{12}$  of the scattering matrix  $S$  and

$$S_{12}S_{12}^\dagger = \begin{pmatrix} 1611.0622 + 0 & -22.5551 + i49.4429 \\ -22.5551 - 49.4429 & 1811.7863 \end{pmatrix}. \quad (4.16)$$

Since  $S_{ij}$  for  $\beta = 4$  is real quaternion,  $S_{ij}S_{ij}^\dagger$  must be proportional to the  $2 \times 2$  unit matrix. However, in the experiment this can not be achieved with arbitrary accuracy due to power losses. Nevertheless, Eq. (4.16) shows the fact that the system still remains the symmetry within the limit of tolerance in the experiment. We have measured all necessary elements of S-matrix given by Eq. (4.6) for all three symmetry classes.

## 4.4 Results

The experimental results are given in Fig. 4.3. The left column, from top to bottom shows the experimentally measured value of the quantity  $f$  for  $\beta = 1$  (GOE),  $\beta = 2$  (GUE) and  $\beta = 4$  (GSE), respectively. For the case of  $\beta = 1$ , the measurement was performed from 1 GHz to 17 GHz frequency regime, while due to the working frequency of the circulator for the case of  $\beta = 2$  and  $\beta = 4$  the frequency range is limited to 6 to 12 GHz. The right column, from the top to bottom shows both experimental and theoretical distribution of  $f$  for the cases of  $\beta = 1$ ,  $\beta = 2$  and  $\beta = 4$ , respectively. For the cases  $\beta = 1$  and  $\beta = 2$  data from two realizations were used and for  $\beta = 4$  data from only one realization is used. The histogram represents the experimental result and the black solid line is for the theoretical predictions given by Eq. (4.15).

The clear visible deviations between experiment and theory for case  $\beta = 1$  and  $\beta = 2$  can be explained by the power losses within the whole setup. The effect of the absorption can be quantified by assuming that the scattering matrix of the graph does not conserve flux; while the effect of the coupling can be modeled by adding identical barriers, with transmission intensity  $T_a$ , between the graph and port 1, between the graph and the T-junction, and between the T-junction and port 2, respectively. Following Ref. [47], such scattering matrix, that we denote by  $\tilde{S}_g$ , can be written as

$$\tilde{S}_g(E) = 1 - 2\pi i \tilde{W}^\dagger \frac{1}{E - \tilde{\mathcal{H}} + i\pi \tilde{W} \tilde{W}^\dagger} \tilde{W}, \quad (4.17)$$

where  $E$  is the energy and  $\tilde{W}$  accounts for the coupling between the resonant modes of the graph and the scattering channels. Here,  $\tilde{\mathcal{H}}_{mn} = H_{mn} + i(\gamma\Delta/4\pi)\delta_{mn}$ , with  $H$  being the Hamiltonian that describes the closed microwave graph with mean level spacing  $\Delta$  and it is taken from the Gaussian ensembles corresponding to the symmetry present in the graph. The imaginary part of  $\tilde{\mathcal{H}}$  mimics the absorption quantified by the parameter  $\gamma$ . It can be extracted from the experimental data through the autocorrelation function between elements of the scattering matrix.

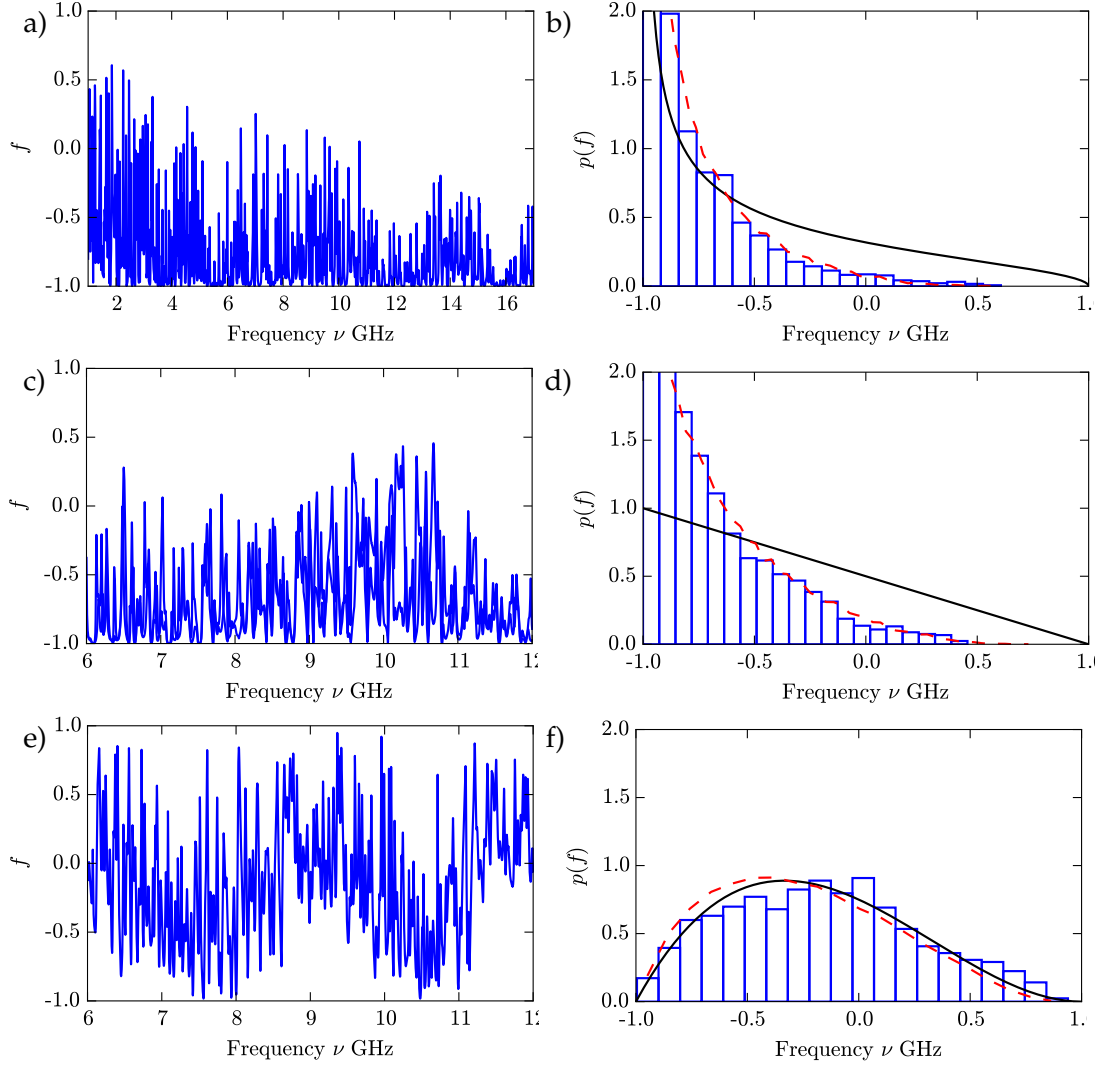


**Fig. 4.3.**  $f$  as a function of the frequency is shown in the left column, and its corresponding distribution in the right column, for  $\beta = 1$  (top), 2 (middle), and 4 (bottom). In the right column the black solid lines represent the analytical result for the ideal case, Eq. (4.15), while the dashed lines correspond to RMT simulations with power losses and imperfect coupling of the T-junctions to the graph, where all parameters were fixed before hand using the autocorrelation functions (see Fig. (4.4)). For the statistical analysis we used an ensemble of  $5 \times 10^4$  realizations.

After some mathematics, they can be written as

$$\frac{C_{aa}^{(\beta)}(t)}{T_a^2} = \begin{cases} \left[ \frac{3}{(1+2T_a t)^3} - \frac{b_{1,2}(t)}{(1+T_a t)^4} \right] e^{-\gamma t} & \text{for } \beta = 1, \\ \left[ \frac{2}{(1+T_a t)^4} - \frac{2^6 b_{2,2}(t)}{(2+T_a t)^6} \right] e^{-\gamma t} & \text{for } \beta = 2, \\ \left[ \frac{6}{(1+T_a t)^6} - \frac{2^{12} b_{4,2}(t)}{(2+T_a t)^{10}} \right] e^{-2\gamma t} & \text{for } \beta = 4, \end{cases} \quad (4.18)$$

where  $b_{\beta,2}(t)$  is the two-level form factor [50] and  $T_a$  is the coupling strength, which is also extracted from the experiment via  $T_a = 1 - |\langle S_{aa} \rangle|^2$  with the average  $\langle S_{aa} \rangle$



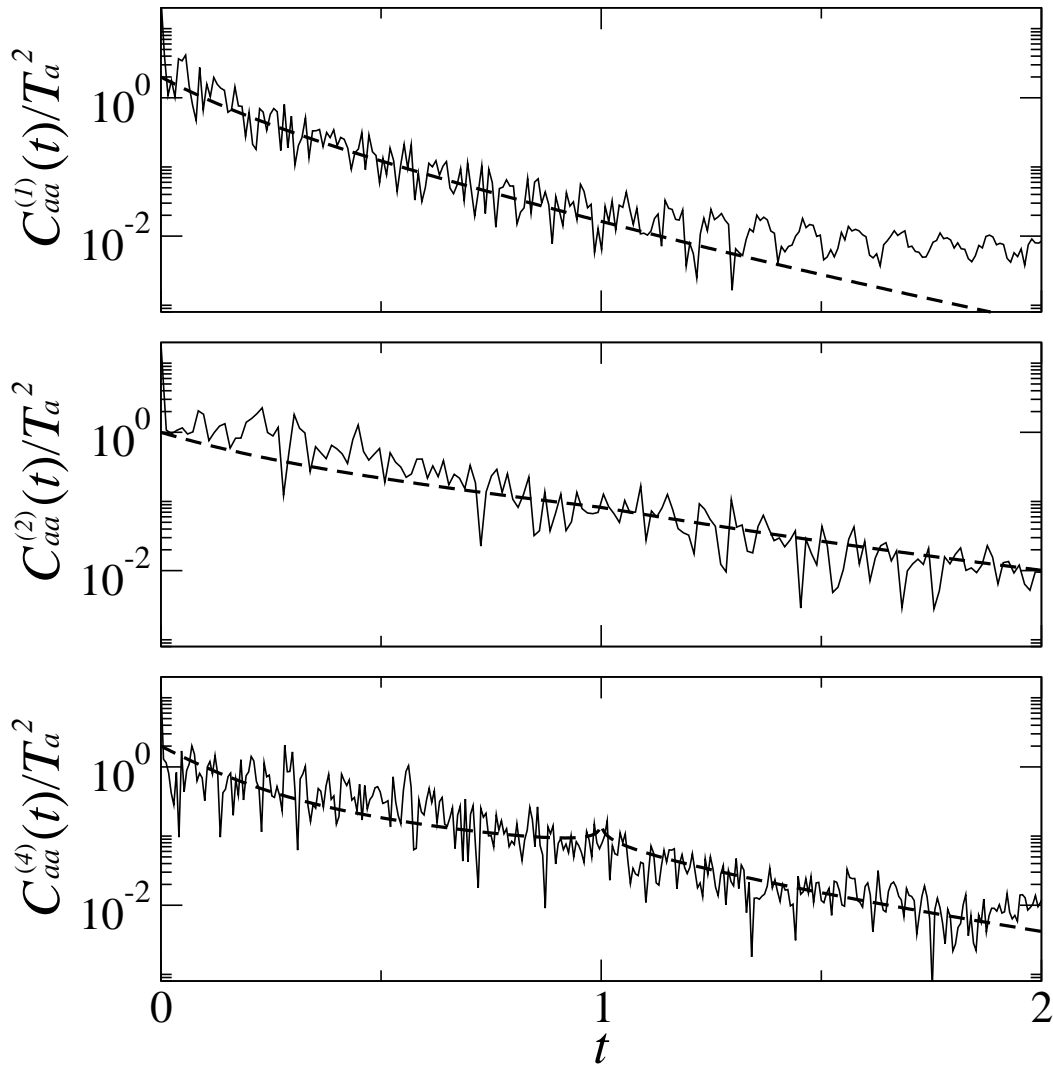


**Fig. 4.4.** Fitting of the autocorrelation function, Eq. (4.18), to the experimental data. The parameters are  $T_a = 0.98$  and  $\gamma = 1.9$  for  $\beta = 1$ ,  $T_a = 0.96$  and  $\gamma = 0.5$  for  $\beta = 2$ , and  $T_a = 0.97$  and  $\gamma = 0.2$  for  $\beta = 4$ .

taken over the frequency. The corresponding expression for the GOE is given in Ref. [48], while for all  $\beta$  in Ref. [49].

Fig. (4.4) shows the autocorrelation function  $C_{aa}^{(\beta)}(t)$  of the experimental data. The best fit yields  $T_a = 0.98$  and  $\gamma = 1.9$ , for  $\beta = 1$ ,  $T_a = 0.96$  and  $\gamma = 0.5$ , for  $\beta = 2$ , and  $T_a = 0.97$  and  $\gamma = 0.2$ , for  $\beta = 4$ , and they are plotted as dashed lines. The coupling values for all three setups are obtained from the experimental data. One notices that the coupling is almost perfect due to the standard 50 $\Omega$  technology. As expected the coupling parameters are almost the same for the three symmetries but the absorption parameter is significantly different from one symmetry to another. In particular, we notice that the value of  $\gamma$  for  $\beta = 2$  is almost twice the value for  $\beta = 4$ . This may be due to the interplay of reflection and absorption [51], i.e., the higher the reflection the smaller the absorption. This is the situation of the  $\beta = 4$  case which presents twice the reflection than that of the  $\beta = 2$  case (two subgraphs). Also, the circulators introduce more reflections for  $\beta = 2$  and 4 in comparison with

the  $\beta = 1$  case with no circulators. The parameters  $T_a$  and  $\gamma$  are used in Eq. (4.17), from which we obtain  $T_{31}$  and  $T_{32}$ , and finally compute  $f$ . The results are shown in Fig. (4.3) (lower panels) as dashed lines. A good agreement with the experimental distribution is observed. For the symplectic case the agreement between experiment and theory is good even without the correction due to absorption and imperfect coupling; since  $\gamma$  is relatively small,  $p_4(f)$  depends only weakly on the port couplings which are almost perfect.

# Summary

In this work, I have presented a number of experimental results which can be described by random matrix theory (RMT) and scattering theory.

The main results are presented in Chapter 3. Here, following an idea by Joyner *et al.* [23], we have constructed microwave quantum graphs simulating spin-1/2 systems with an antiunitary symmetry of  $\mathcal{T}$  obeying  $\mathcal{T}^2 = -1$ . From the reflection spectrum we observed a set of Kramers doublets. The nearest neighbor spacing distribution of these doublets agrees to the random matrix Wigner GSE prediction. Moreover, to study the long range correlation, we examined the spectral two point correlation function  $R_2(L)$  and its Fourier transform, the spectral form factor  $K(\tau)$ , as well as smoothed quantities such as the number variance  $\Sigma^2(L)$  and the spectral rigidity  $\Delta_3(L)$ . Despite the existence of a few percent of missing levels, the experimental results of these quantities exhibited overall good agreement with the GSE statistics expected from random matrix theory. As the experiment is only connecting two subgraphs by one pair of bonds we introduced a one pair of connecting bonds approximation and extended it to the case of a GSE graph with more pairs of connecting bonds. The numerical random matrix simulation confirmed that one needs ten pairs of connecting bonds to arrive at the Wigner GSE distribution. Finally, we have studied a parameter dependent dynamical transition from GSE via GUE to GOE statistics. For particular values of the varying parameter, the experimental results showed the level repulsion expected for all three cases, namely GOE, GUE and GSE.

In chapter 4, we have presented the work which has been done in close collaboration with Dr. A. M. Martínez-Argüello from Mexico. The measurements analyzed in this part have been performed when he has visited our laboratory. We have studied the transport properties of three terminal microwave graphs with orthogonal, unitary and symplectic symmetry. Here, a theoretical prediction for  $f$  was given, a universal symmetry dependent probability distribution related to the transport within the three terminal system. We examined this prediction experimentally by means of microwave scattering experiments on quantum graphs with orthogonal, unitary and symplectic symmetry. After considering the effect of absorption good agreement was found between the experimental results and the theoretical prediction. Surprisingly, for the symplectic case, the result shows that the absorption could hardly disturb the symmetry, in contrast to the orthogonal and unitary case.



## Appendix A

Here I shall present the full reflection spectra  $|S_{00}|^2$  for constant  $\Delta\varphi$  for one of the studied graphs. The green and red solid lines correspond to constant  $\Delta\varphi = \pi$  and  $\Delta\varphi = 3\pi$ , respectively, determined by Eq. (3.44). They are zoomed of Fig. 3.12. The only difference between these two ones is that in Fig. 3.12 the unaccessible region limited by the Eq. (3.45) is white (upper part) while it is black here in this zoomed version. Each individual plot spans a 1 GHz frequency window. The features as shown in Fig. 3.13 are visible with clear Kramers doublets in the entire frequency window from 6 to 12 GHz. The green and red horizontal lines are for the constant values of  $\Delta\varphi = \pi$  and  $\Delta\varphi = 3\pi$ , respectively.

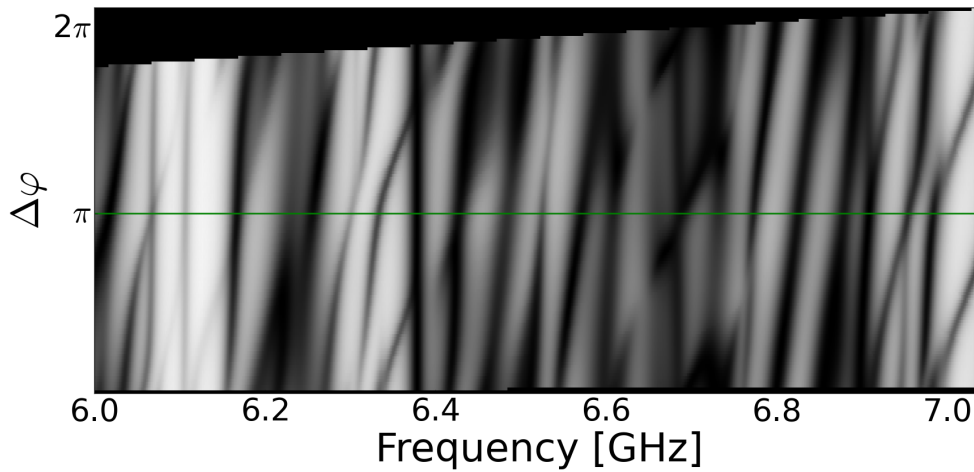


Fig. A.1

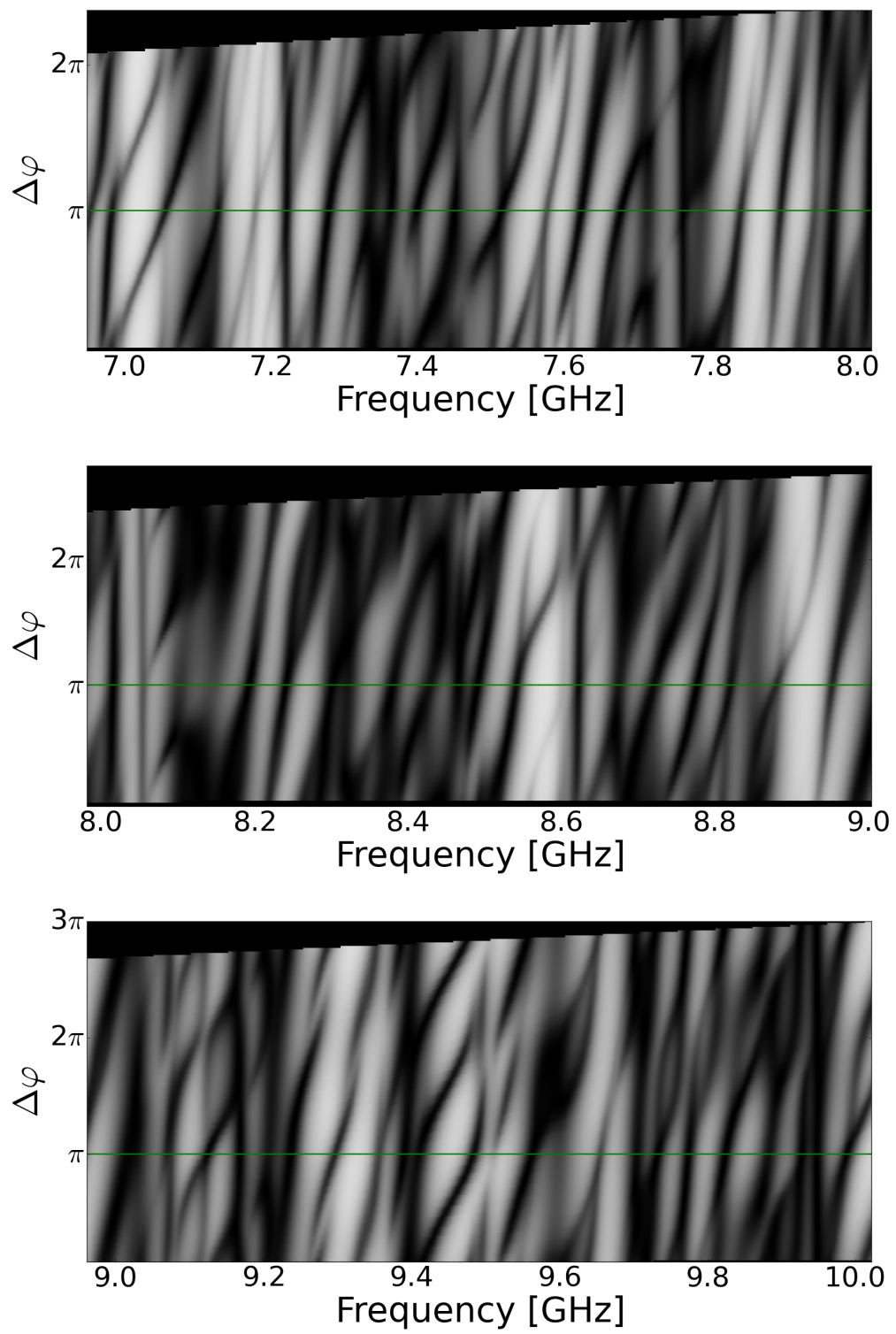


Fig. A.2

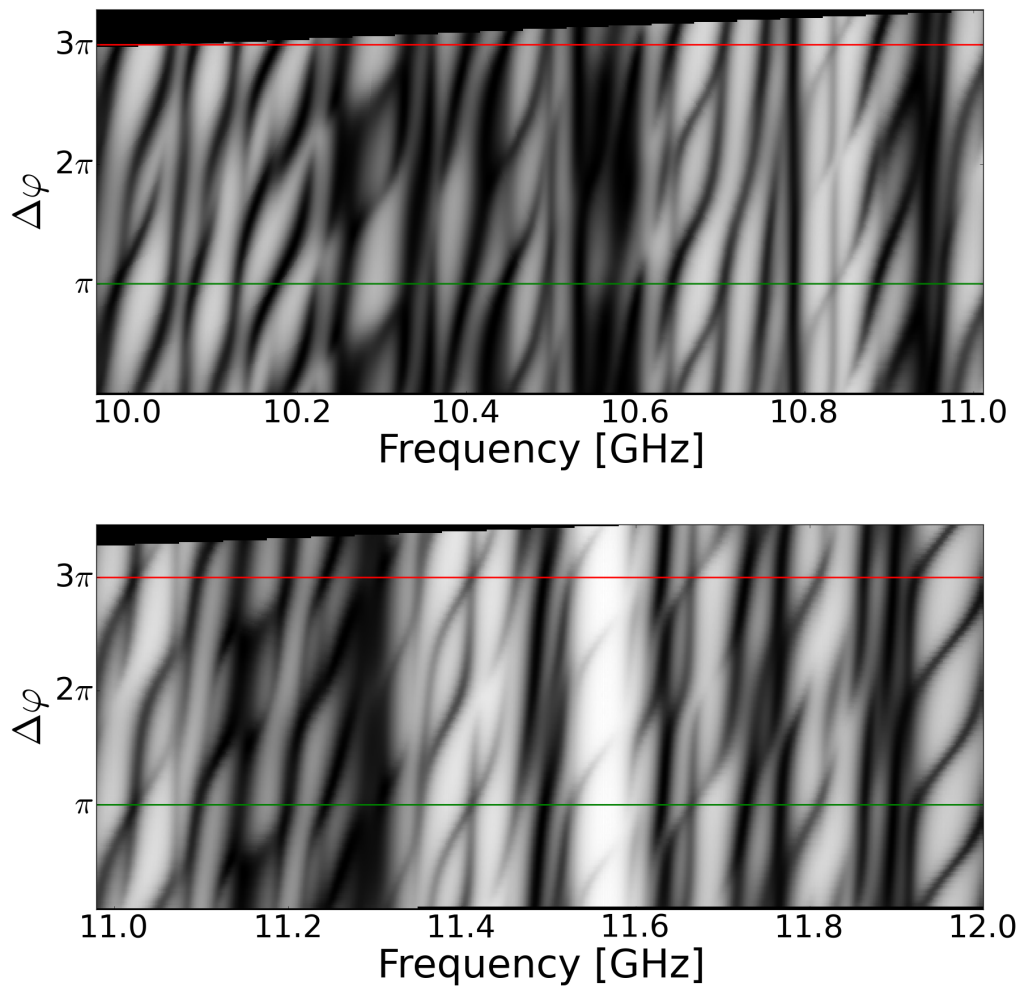


Fig. A.3





# Bibliography

- [1] O. Bohigas, M. J. Giannoni, and C. Schmit. Characterization of chaotic spectra and universality of level fluctuation laws. *Phys. Rev. Lett.*, 52:1, 1984. doi: 10.1103/PhysRevLett.52.1.
- [2] M. L. Mehta. *Random Matrices*. Academic Press, New York, 2nd edition, 1991.
- [3] Giulio Casati, Italo Guarneri, and Fausto Valz Gris. On the connection between quantization of non integrable systems and the statistical theory of spectra. 28: 279, 06 1980.
- [4] F. Haake. *Quantum Signatures of Chaos*. Springer, Berlin, 1991.
- [5] Eugene P. Wigner. On the distribution of the roots of certain symmetric matrices. *Annals of Mathematics*, 67(2):325–327, 1958. ISSN 0003486X.
- [6] C. E. Porter. *Statistical Theory of Spectra: Fluctuations*. Academic Press, New York, 1965.
- [7] T. A. Brody, J. Flores, J. B. French, P. A. Mello, A. Pandey, and S. S. M. Wong. Random-matrix physics: spectrum and strength fluctuations. 53:385, 1981. doi: 10.1103/RevModPhys.53.385.
- [8] H.-J. Stöckmann. *Quantum Chaos - An Introduction*. University Press, Cambridge, 1999. ISBN 9780521592840. doi: 10.2277/0521592844.
- [9] P. So, S. M. Anlage, E. Ott, and R. N. Oerter. Wave chaos experiments with and without time reversal symmetry: GUE and GOE statistics. *Phys. Rev. Lett.*, 74: 2662, 1995. doi: 10.1103/PhysRevLett.74.2662.
- [10] U. Stoffregen, J. Stein, H.-J. Stöckmann, M. Kuś, and F. Haake. Microwave billiards with broken time reversal symmetry. *Phys. Rev. Lett.*, 74:2666, 1995. doi: 10.1103/PhysRevLett.74.2666. URL <http://link.aps.org/doi/10.1103/PhysRevLett.74.2666>.
- [11] Ferdinand Kuemmeth, Kirill I. Bolotin, Su-Fei Shi, and Daniel C. Ralph. Measurement of discrete energy-level spectra in individual chemically synthesized gold nanoparticles. *Nano Letters*, 8(12):4506–4512, 2008. doi: 10.1021/nl802473n. PMID: 18983200.
- [12] O. Hul, S. Bauch, P. Pakoński, N. Savitsky, K. Życzkowski, and L. Sirko. Experimental simulation of quantum graphs by microwave networks. *Phys. Rev. E*, 69:056205, 2004. doi: 10.1103/PhysRevE.69.056205.
- [13] A. Rehemanjiang, M. Richter, U. Kuhl, and H.-J. Stöckmann. Spectra and spectral correlations of microwave graphs with symplectic symmetry. *Phys. Rev. E*, 97:022204, 2018. doi: 10.1103/PhysRevE.97.022204.

- [14] H. Alt, H.-D. Gräf, T. Guhr, H. L. Harney, R. Hofferbert, H. Rehfeld, A. Richter, and P. Schardt. Correlation-hole method for the spectra of superconducting microwave billiards. *Phys. Rev. E*, 55:6674, 1997. doi: 10.1103/PhysRevE.55.6674.
- [15] F. Leyvraz, C. Schmit, and T. H. Seligman. Anomalous spectral statistics in a symmetrical billiard. *J. Phys. A*, 29:L575, 1996. doi: 10.1088/0305-4470/29/22/004.
- [16] B. Gutkin. Dynamical ‘breaking’ of time reversal symmetry. *J. Phys. A*, 40:F761, 2007. doi: 10.1088/1751-8113/40/31/F02.
- [17] C. Dembowski, H.-D. Gräf, A. Heine, H. Rehfeld, A. Richter, and C. Schmit. Gaussian unitary ensemble statistics in a time-reversal invariant microwave triangular billiard. *Phys. Rev. E*, 62:4516(R), 2000. doi: 10.1103/PhysRevE.62.R4516.
- [18] R. Schäfer, M. Barth, F. Leyvraz, M. Müller, T. H. Seligman, and H.-J. Stöckmann. Transition from gaussian-orthogonal to gaussian-unitary ensemble in a microwave billiard with threefold symmetry. *Phys. Rev. E*, 66:016202, 2002. doi: 10.1103/PhysRevE.66.016202.
- [19] B. Dietz, T. Guhr, B. Gutkin, M. Miski-Oglu, and A. Richter. Spectral properties and dynamical tunneling in constant-width billiards. *Phys. Rev. E*, 90:022903, 2014. doi: 10.1103/PhysRevE.90.022903.
- [20] M. V. Berry and M. Robnik. Statistics of energy levels without time-reversal symmetry: Aharonov-Bohm chaotic billiards. *J. Phys. A*, 19:649, 1986. doi: 10.1088/0305-4470/19/5/019.
- [21] F. J. Dyson. A Brownian-motion model for the eigenvalues of a random matrix. 3:1191, 1962. doi: 10.1063/1.1703862.
- [22] R. Scharf, B. Dietz, M. Kuś, F. Haake, and M. V. Berry. Kramers’ degeneracy and quartic level repulsion. *Europhys. Lett.*, 5:383, 1988. doi: 10.1209/0295-5075/5/5/001.
- [23] C. H. Joyner, S. Müller, and M. Sieber. GSE statistics without spin. *Europhys. Lett.*, 107:50004, 2014. doi: 10.1209/0295-5075/107/50004.
- [24] T. Kottos and U. Smilansky. Quantum chaos on graphs. *Phys. Rev. Lett.*, 79:4794, 1997. doi: 10.1103/PhysRevLett.79.4794.
- [25] F. Haake. *Quantum Signatures of Chaos. 2nd edition*. Springer, Berlin, 2001. doi: 10.1007/978-3-642-05428-0.
- [26] Gernot Akemann, Jinho Baik, and Philippe Di Francesco, editors. *The Oxford Handbook of Random Matrix Theory*. Oxford University Press, 2011.
- [27] T. Kottos and U. Smilansky. Periodic orbit theory and spectral statistics for quantum graphs. 274:76, 1999. doi: 10.1006/aphy.1999.5904.
- [28] URL [https://en.wikipedia.org/wiki/Quaternion\\_group](https://en.wikipedia.org/wiki/Quaternion_group).
- [29] P. A. Mello and N. Kumar. *Quantum Transport in Mesoscopic Systems: Complexity and Statistical Fluctuations*. Oxford University Press, Oxford, 2004. doi: 10.1093/acprof:oso/9780198525820.001.0001.

- [30] Ram Band, Ori Parzanchevski, and Gilad Ben-Shach. The isospectral fruits of representation theory: quantum graphs and drums. *Journal of Physics A: Mathematical and Theoretical*, 42(17):175202, 2009.
- [31] Ori Parzanchevski and Ram Band. Linear representations and isospectrality with boundary conditions. *Journal of Geometric Analysis*, 20(2):439–471, 2010.
- [32] M. Allgaier, S. Gehler, S. Barkhofen, H.-J. Stöckmann, and U. Kuhl. Spectral properties of microwave graphs with local absorption. *Phys. Rev. E*, 89:022925, 2014. doi: 10.1103/PhysRevE.89.022925.
- [33] A. Rehemanyang, M. Allgaier, C. H. Joyner, S. Müller, M. Sieber, U. Kuhl, and H.-J. Stöckmann. Microwave realization of the gaussian symplectic ensemble. *Phys. Rev. Lett.*, 117:064101, 2016. doi: 10.1103/PhysRevLett.117.064101.
- [34] D. V. Savin, O. Legrand, and F. Mortessagne. Inhomogeneous losses and complexness of wave functions in chaotic cavities. *Europhys. Lett.*, 76:774, 2006. doi: 10.1209/epl/i2006-10358-3.
- [35] J. D. Jackson. *Classical Electrodynamics*, 3rd ed. John Wiley & Sons, New York, 1998.
- [36] M. C. Gutzwiller. Periodic orbits and classical quantization conditions. 12:343, 1971.
- [37] A. Richter. *Playing Billiards with Microwaves — Quantum Manifestations of Classical Chaos*, pages 479–523. Springer New York, New York, NY, 1999. doi: 10.1007/978-1-4612-1544-8\_20.
- [38] D. Dubbers and H.-J. Stöckmann. *Quantum Physics: The Bottom-Up Approach*. Springer, Berlin Heidelberg, 2013. ISBN 978-3-642-31059-1. doi: 10.1007/978-3-642-31060-7.
- [39] Madan Lal Mehta and Freeman J. Dyson. Statistical theory of the energy levels of complex systems. v. *Journal of Mathematical Physics*, 4(5):713–719, 1963. doi: 10.1063/1.1704009.
- [40] M. Białous, V. Yunko, S. Bauch, M. Ławniczak, B. Dietz, and L. Sirko. Power spectrum analysis and missing level statistics of microwave graphs with violated time reversal invariance. *Phys. Rev. Lett.*, 117:144101, 2016. doi: 10.1103/PhysRevLett.117.144101.
- [41] Peter D. Georgopoulos and Harry S. Camarda. Use of the dyson-mehta  $\Delta_3$  statistic as a test of missing levels. *Phys. Rev. C*, 24:420–425, Aug 1981. doi: 10.1103/PhysRevC.24.420.
- [42] R. de Picciotto, H. L. Stormer, L. N. Pfeiffer, K. W. Baldwin, and K. W. West. Four-terminal resistance of a ballistic quantum wire. *Nature*, 411(6833):51–54, 2001. doi: 10.1038/35075009.
- [43] Shinya Yoshimoto, Yuya Murata, Keisuke Kubo, Kazuhiro Tomita, Kenji Motoyoshi, Takehiko Kimura, Hiroyuki Okino, Rei Hobara, Iwao Matsuda, Shin-ichi Honda, Mitsuhiro Katayama, and Shuji Hasegawa. Four-point probe resistance measurements using ptir-coated carbon nanotube tips. *Nano Letters*, 7(4): 956–959, 2007. doi: 10.1021/nl0630182.

- [44] S. Godoy and P. A. Mello. The voltage drop along a mesoscopic conductor. Is it a well-defined macroscopic variable? Are there limitations in its determination? *Europhys. Lett.*, 17:243, 1992. doi: 10.1209/0295-5075/17/3/010.
- [45] S. Godoy and P. A. Mello. Random-matrix study of multiprobe mesoscopic devices: A three-probe one-dimensional system. 46:2346, 1992. doi: 10.1103/PhysRevB.46.2346.
- [46] P. W. Brouwer and C. W. J. Beenakker. Conductance distribution of a quantum dot with nonideal single-channel leads. 50:11263, 1994. doi: 10.1103/PhysRevB.50.11263.
- [47] P. W. Brouwer and C. W. J. Beenakker. Voltage-probe and imaginary-potential models for dephasing in a chaotic quantum dot. 55:4695, 1997. doi: 10.1103/PhysRevB.55.4695.
- [48] R. Schäfer, T. Gorin, T. H. Seligman, and H.-J. Stöckmann. Correlation functions of scattering matrix elements in microwave cavities with strong absorption. *J. Phys. A*, 36:3289, 2003. doi: 10.1088/0305-4470/36/12/325.
- [49] Y V Fyodorov, D V Savin, and H-J Sommers. Scattering, reflection and impedance of waves in chaotic and disordered systems with absorption. *Journal of Physics A: Mathematical and General*, 38(49):10731, 2005.
- [50] T. Guhr, A. Müller-Groeling, and H. A. Weidenmüller. Random matrix theories in quantum physics: common concepts. 299:189, 1998. doi: 10.1016/S0370-1573(97)00088-4.
- [51] G. Báez, M. Martínez-Mares, and R. A. Méndez-Sánchez. Absorption strength in absorbing chaotic cavities. *Phys. Rev. E*, 78:036208, 2008.

# Acknowledgments

I thank everybody who contributed to the success of this thesis. My special thanks goes to the following persons:

Prof. Dr. Hans-Jürgen Stöckmann for giving me the precious opportunity to do my PhD work in his group, for many fruitful discussions, for all his priceless help, for his kindness, for very patient guidance and the last but not least for giving great ideas for the projects.

Prof. Dr. Ulrich Kuhl for his kind guidance concerning measurements and data analysis, for giving me the opportunity to stay one month in his research laboratory in Nice, France and for the friendly supervision during my PhD project.

Prof. Dr. B. Eckhardt as a second referee for help and discussions about my PhD work.

Prof. Dr. Martin Sieber, Dr. Sebastian Müller from Bristol and Dr. Chris H. Joyner from London for cooperation in our joint project of the realization of the GSE system.

Dr. A. M. Martínez-Argüello, M. Martínez-Mares and J. A. Méndez-Bermúdez from Mexico for the undergoing collaborative work on the three terminal transport device.

The member of the electronic workshop for their reliable support.

The member of the fine mechanic workshop for the help to build the phase shifter frame and other technical supports.

My colleague Tobias Hofmann for the friendly working atmosphere in the quantum chaos group.

Other colleagues Mrs. Annegret Webel, Mrs. Beatrix Payer from the physics department and Mrs. Heidi Wiegand from the international office of the university for their kind support during my stay as a PhD student in Marburg.

My lovely parents for their unconditional support not only during my study, but also my everyday life by an invisible love.

My lovely wife Gulistan for her tremendous support, encouragement, what she has been paying for our family and most importantly her unconditional love. My cute son Zulkar for his sweet smile, the hope and, of course, the love that he has brought to our family.



# Wissenschaftlicher Werdegang

- 05.09.1984    geboren in Kashgar, Xinjiang, Volksrepublik China
- 2004-2009    B. Sc. Physik, an der Xinjiang Universität, Ürümqi, China  
 (Prof. Dr. Baishan Shadike)  
*Comparing magnetic characteristics of magnetic thin films  
 SiO<sub>2</sub>/NiFe/Ta and SiO<sub>2</sub>/NiFe/Ru (in Chinesisch)*
- 2009-2010    Studium zum M. Sc. Materialphysik (*nicht abgeschlossen*), an der  
 Xinjiang Universität, Ürümqi, China
- 2011-2014    M. Sc. Physik, an der Universität Camerino,  
 Camerino, Italien  
 (Prof. Dr. David Vitali und Dr. Riccardo Natali)  
*Finite element analysis of mechanical and thermal properties of a  
 nanomembrane within an optomechanical setup*
- 2015-2018    Promotion in der Arbeitsgruppe Quantenchaos an der  
 Philipps-Universität Marburg, Marburg (Lahn), Deutschland  
 (PD. Dr. Ulrich Kuhl und Prof. Dr. Hans-Jürgen Stöckmann)  
*Microwave Experiments on Graphs Simulating Spin-1/2 System*